理學博士 學位論文

Dye-Sensitized Solar Cells based on Titanium Oxide(Ⅳ) Nanotube Arrays

티타니아 나노튜브 층이 도입된 염료감응형 태양전지

2017年 8月

서울大學校 大學院

化學部

千命煥

Dye-Sensitized Solar Cells based on Titanium Oxide(Ⅳ) Nanotube Arrays

티타니아 나노튜브 층이 도입된 염료감응형 태양전지

指導敎授 徐 正 雙 博士

이 論文을 理學博士 學位論文으로 提出함.

2017년 8월

서울大學校 大學院

化學部

千 命 煥

천명환의 이학박사 학위논문을 인준함

2017년 8월

위 원 장 정 연 준 (인)

부위원장 서 정 쌍 (인)

위 원 홍 종 인 (인)

위 원 정 대 홍 (인)

위 원 윤 천 호 (인)

Abstract

We prepared dye-sensitized solar cells (DSSCs) with enhanced energy conversion efficiency using open-ended TiO_2 nanotube arrays with a TiO_2 scattering layer. As compared to closed-ended TiO_2 nanotube arrays, the energy conversion efficiency of the open-ended TiO_2 nanotube arrays was increased from 5.63% to 5.92%, which is an enhancement of 5.15%. With the TiO_2 scattering layer, the energy conversion efficiency was increased from 5.92% to 6.53%, which is an enhancement of 10.30%. After treating the open-ended TiO_2 nanotube arrays with $TiCl_4$, the energy conversion efficiency was increased from 5.92% to 6.89%, a 16.38% enhancement, which is attributed to improved light harvesting and increased dye adsorption.

Dye-sensitized solar cells (DSSCs) were fabricated using open-ended freestanding TiO_2 nanotube arrays functionalized with Ag nanoparticles (NPs) in the channel to create a plasmonic effect, and then coated with large TiO_2 NPs to create a scattering effect in order to improve energy conversion efficiency. Compared to closed-ended freestandung TiO_2 nanotube array-based DSSCs without Ag or large TiO_2 NPs, the energy conversion efficiency of closed-ended DSSCs improved by 9.21%(actual efficiency, from 5.86% to 6.40%) with Ag NPs, 6.48%(actual efficiency, from 5.86% to 6.24%) with TiO_2 NPs, and

14.50%(actual efficiency, from 5.86% to 6.71%) with both Ag NPs and TiO_2 NPs. By introducing Ag NPs and/or large TiO_2 NPs to open-ended freestanding TiO_2 nanotube array-based DSSCs, the energy conversion efficiency was improved by 9.15%(actual efficiency, from 6.12% to 6.68%) with Ag NPs and 8.17%(actual efficiency, from 6.12% to 6.62%) with TiO_2 NPs, and by 15.20%(actual efficiency, from 6.12% to 7.05%) with both Ag NPs and TiO_2 NPs. Moreover, compared to closed-ended freestanding TiO_2 nanotube arrays, the energy conversion efficiency of open-ended freestanding TiO_2 nanotube arrays increased from 6.71% to 7.05%. We demonstrate that each component －Ag NPs, TiO_2 NPs and open-ended freestanding TiO_2 nanotube arrays－enhanced the energy conversion efficiency, and the use of a combination of all components in DSSCs resulted in the highest energy conversion efficiency.

Keywords: open-ended freestanding TiO_2 nanotube arrays; dye-sensitized solar cells; plasmonic; scattering; anodization

Student Number : 2002-30153

Contents

List of Table

List of Figures

Chapter 1 Introduction

1. 1. Anodization

Anodization of metal oxide has applications to prevent corrosion, to form capacitor dielectrics [1], to template nanomaterials [2-7], and to apply to catalysis, optics, and electronics [8-10]. Anodic aluminum oxide (AAO), known as porous anodic oxide, was first reported [11-14] and is now commercially available because its pores can be used as template for preparing nanostructures. Additionally, anodic metal oxide has been achieved on surface of many other metals such as tungsten [15], zirconium [16], titanium [17-19], tantalum [20], hafnium [21], niobium [22], and vanadium [23].

The formation of anodic metal oxides is based on two continuous processes, one is oxide dissolution at the electrolyte/oxide interface and the other is oxidation of metal at the oxide/metal interface. To optimize the anodization condition for pore ordering and pore size, the electrochemical process and chemical reagents are more investigated [24, 25].

1. 1. 1. Titanium (Ti) anodization - Anodic titanium oxide (ATO)

Anodic titanium oxide, TiO_2 nanotubes, has better properties compared to many other forms of TiO_2 for application in photocatalysis [26, 27],

gas sensors [28-31], photoelectrolysis [10, 32, 33], and photovoltaics [34, 36]. Since Zwilling reported the TiO_2 nanotubes in chromic acid and hydrofluoric acid in 1999 [37], TiO_2 nanotubes have been made in the fabrication, characterization, application, and formation mechanism [38].

Gong reported TiO_2 nanotubes in a 0.5 wt% HF aqueous solution at room temperature using different anodizing voltages as shown in Figure 1. 1. [17].

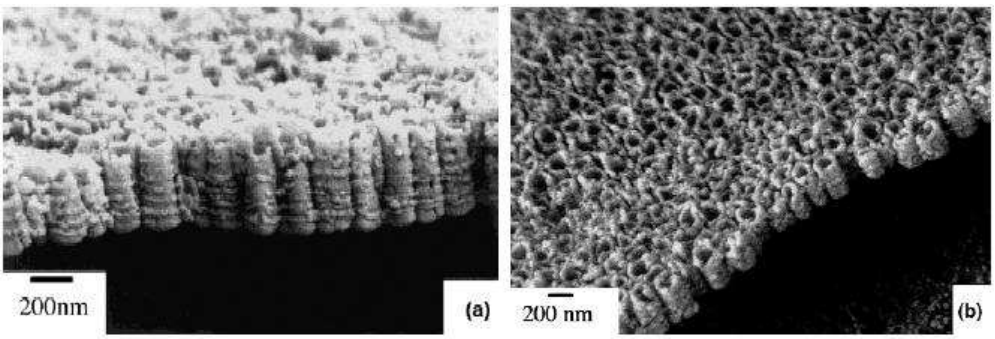

Figure 1. 1. FE-SEM cross-sectional images of titanium oxide nanotubes. The sample was anodized in 0.5 wt% HF solution at 20 V for 20 min [17].

The film thickness could not be increased further from 400-500 nm using HF-based electrolyte. Fluoride solution dissolves the TiO_2 by forming TiF_6^{2-} anions. Too strong acidity of HF electrolyte results in a too fast dissolution of the TiO_2. To overcome this problem, Mor

reported that addition of acetic acid to a 0.5 wt% HF electrolyte in a 1:7 ratio was resulted in more mechanically robust TiO_2 nanotubes without changing their shape and size [29, 39]. The surface morphology of TiO_2 nanotubes are anodized in an electrolyte containing 2.5 % HNO_3 and 1 % HF at 20 V for 4 h showed a uniform, clean, regular TiO_2 nanotube structure with a length about 400 nm that was reported by Ruan. An electrolyte of 0.5 M H_3BO_3, 2.5 % HNO_3, and 1 % HF in anodization at 20 V for 4 h led to irregular pore of TiO_2 nanotubes but long length of TiO_2 nanotubes about 560 nm [40]. To increase the length of TiO_2 nanotubes, Ti was anodized with KF or NaF in electrolyte [41]. The acidity of electrolyte might be controlled by adding HF, H_2SO_4 or Na_2SO_4 to adjust the balance of dissociation of TiO_2 at the electrolyte/oxide interface and oxidation of TiO_2 at the oxide/metal interface [42, 43].

Grimes and co-workers obtained TiO_2 nanotubes up to approximately 1000 mm using a variety of organic electrolytes such as dimethyl sulfoxide, formamide, ethylene glycol, and N-methylformamide as shown in Figure 1. 2. [19, 44, 45].

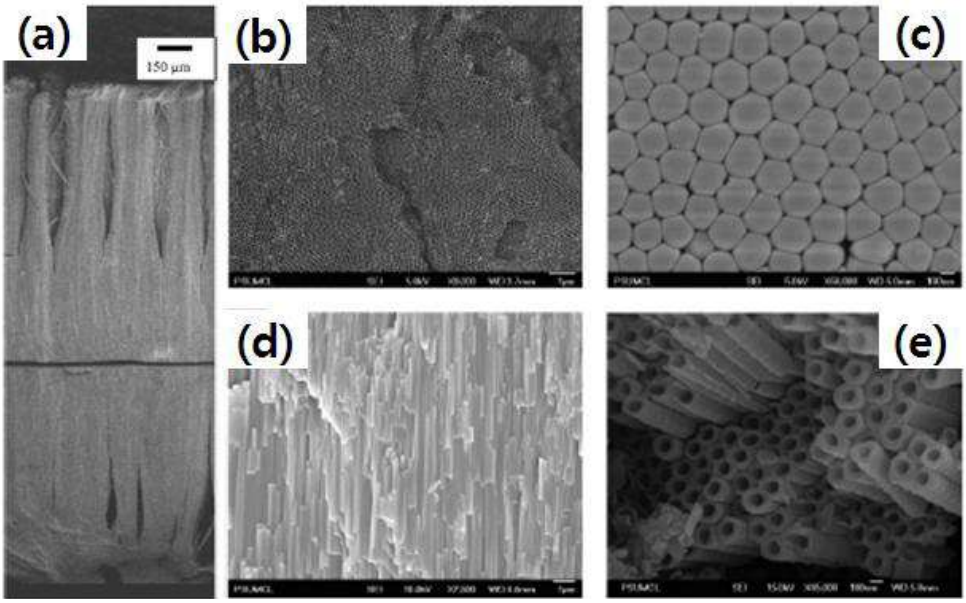

Figure 1. 2. TiO_2 nanotubes over 2 mm in thickness. (a) Cross-sectional view of self-standing TiO_2 nanotubes, (b) top side of nanotube array film, (c) back side or barrier layer side of nanotube array film, and (d, e) cross sectional image of mechanically fractured nanotube array film showing its tubular nature [45].

The key of long length of TiO_2 nanotubes is to minimize water content in the anodization bath to less than 5 %. In organic electrolytes, a little water content reduces the dissociation of the oxide in the fluorine containing electrolytes.

Tahya reported that water content affect the morphology of titanium

oxide array films. [46]

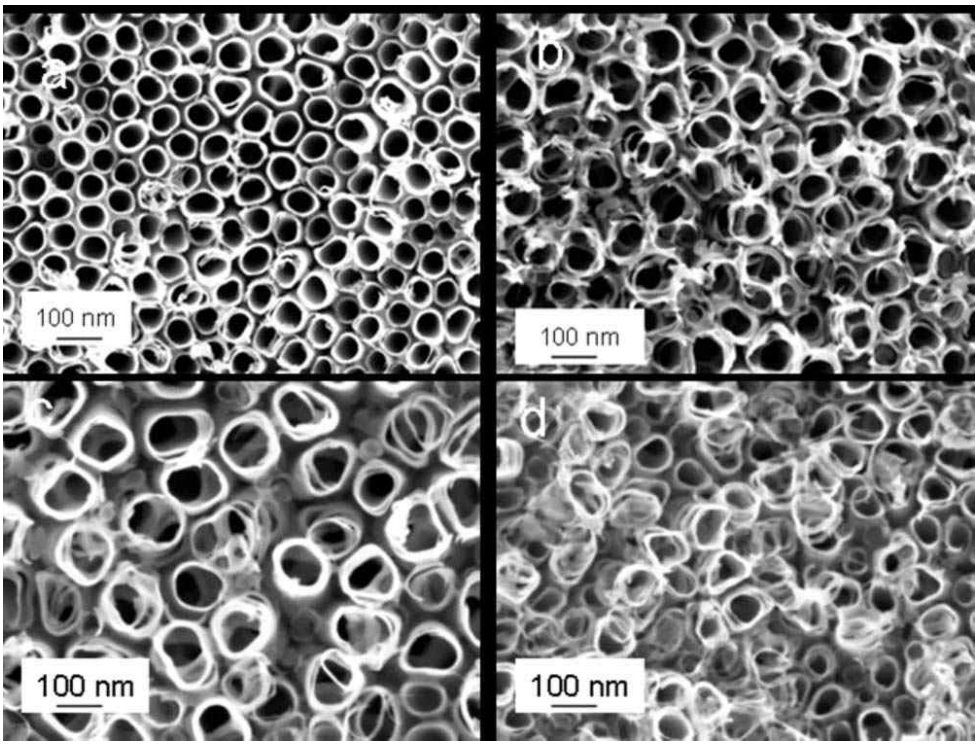

Figure 1. 3. SEM images of TiO_2 NTs grown by electrochemical anodization in NH_4F + H_2O + glycerol electrolyte at different H_2O concentrations: (a) 0% H2O, (b) 20%, (c) 50%, and (d) 70%. The same NH_4F concentration 0.5% was used in these experiments. [46]

1. 1. 2. Chemical reaction of Titanium anodization

The chemical reaction of titanium anodization should be the same as that of aluminum anodization [19, 38, 47, 48].

The anodization process begins with an initial oxide layer formed by interaction of the surface Ti^{4+} ions with oxygen ions in the electrolyte. In the initial stages of the anodization process, field-assisted dissolution dominates the chemical dissolution due to the relatively large electric field across the thin oxide layer. Further oxide growth is controlled by field-assisted ion transport (O^{2-} and Ti^{4+} ions) through the growing oxide. The anode oxidation of titanium is shown in Figure 1. 4.

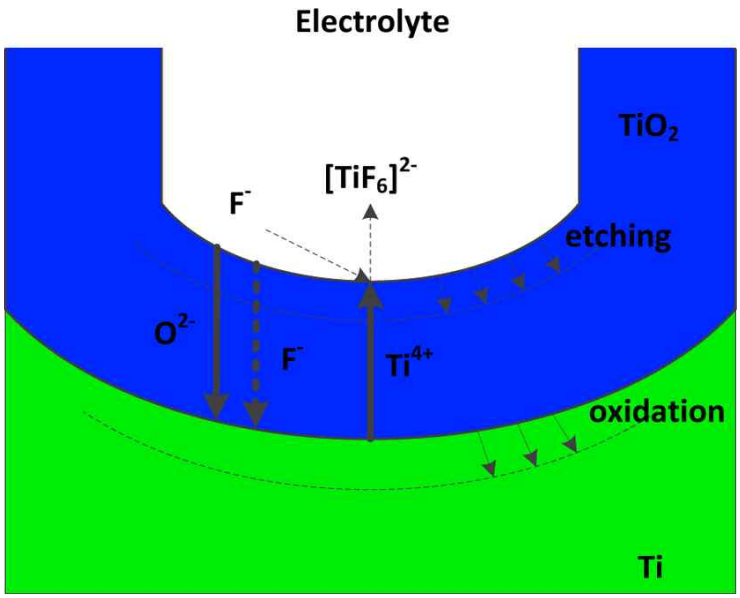

Figure 1. 4. Schematic drawing of adonization process. [49]

Anode:

$$2H_2O \rightarrow O_2 + 4e^- + 4H^+ \qquad \Delta G_0^f = 6577.22 \text{ kJ}$$

$$Ti(s) + O_2 \rightarrow TiO_2 \qquad \Delta G_0^f = -901.61 \text{ kj}$$

The overall anode reaction for anodic oxidation of titanium is represented as

$$Ti(s) + 2H_2O(l) \rightarrow TiO_2(s) + 4H^+ + 4e^- \quad \Delta G_0^f = 348 \text{ kJ}$$

Meanwhile, hydrogen gas is released at the cathode that causes the flotation. The electrode reaction is described as follows:

Cathode:

$$4H^+ + 4e^- \rightarrow 2H_2(g)$$

So the overall electrode reaction at this stage can be described as

$$Ti(s) + 2H_2O(l) \rightarrow 2H_2(g) + TiO_2(s) \quad \Delta G_0^f = 439.98 \text{ kJ}$$

After the formation of the oxide layer, the TiO_2-Ti interface is locally activated, and the chemical and physical diffusions occur in the meantime. Small pores are formed first due to the localized dissolution of the oxide. Then, these pits are converted into bigger pores, and the pore density increases as governed by both electrochemical etching and chemical dissolution. Fluoride ions in the electrolyte have the ability to form water-soluble TiF_6^{2-}, and their small ionic radius makes them

suitable to enter the growing TiO_2 lattice and to be transported through the oxide by the applied electric field. After a while, the individual pores will interfere with each other, balance the available current, and finally reach a steady state condition, which results in a growth of the self-ordered nanotube structure. The nanotubes will grow steadily when the rate of TiO_2 formation equals the rate of TiF_6^{2-} formation and dissolution. The chemical dissolution process of the oxide is described as a chemical reaction

$$TiO_2(s) + 6F^- + 4H^+ \rightarrow TiF_6^{2-} + 2H_2O \qquad \Delta G_0^f = 348 \text{ kJ}$$

The basic premise of electrochemical anodization is the competition between the formation of the compact TiO_2 layer and the formation/dissolution of Ti^{4+} in the nanotube TiO_2 layer. After the formation of the compact TiO_2 oxide layer, Ti^{4+} ions at the metal－oxide interface will move toward the oxide－electrolyte interface under the applied electric field, as illustrated in Figure 1. 5. [50]

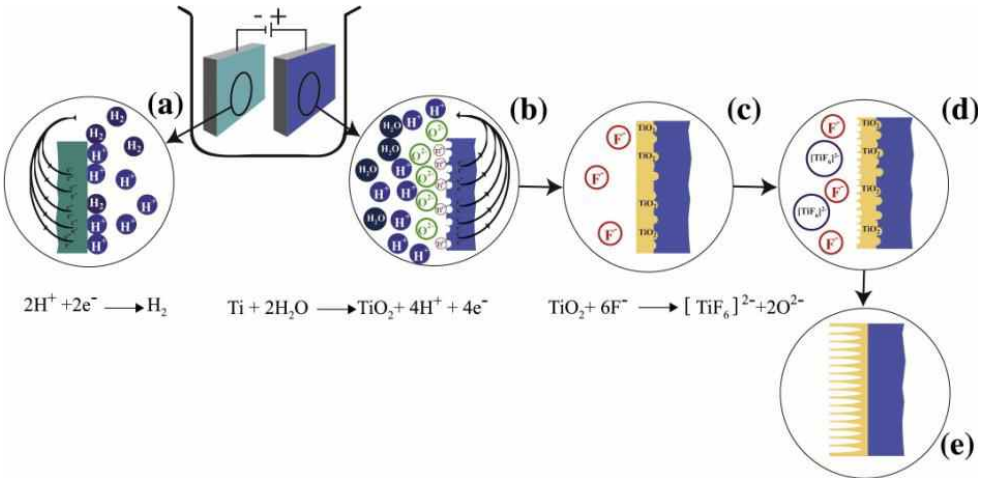

Figure 1. 5. Growth of regular TiO_2 nanotubes: (a) cathodic reaction, (b) anodic reaction,(c) transition state of TiO_2 layer, (d) starting of nanotube formation and (e) TiO_2 nanotubes [51].

1. 1. 3. Formation of TiO_2 nanotubes

The pores are developed from pits on the Ti plate surface and a schematic diagram for the equifield strength model as shown in Figure 1. 6.

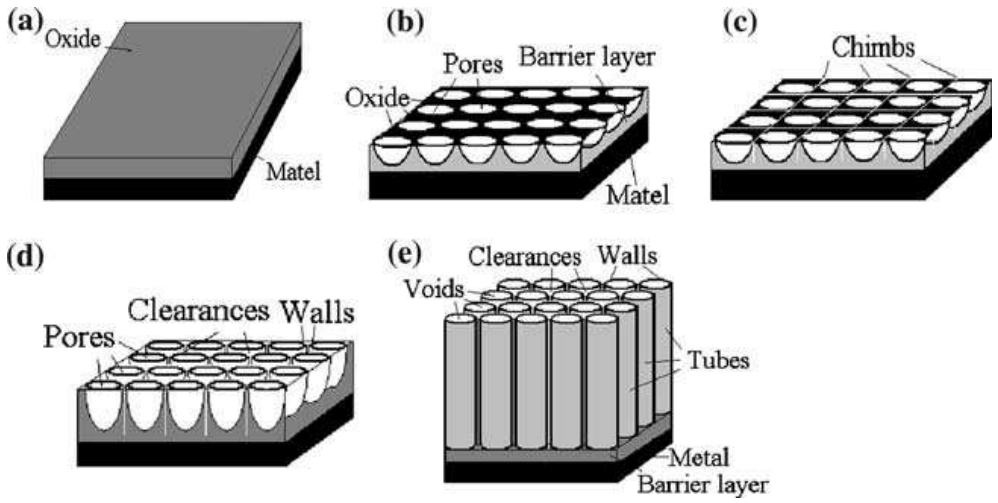

Figure 1. 6. Schematic diagram of the evolution of titania nanotubes in anodization as follows: (a) oxide layer formation; (b) pore formation on the oxide layer; (c) chimbs formation between pores; (d) growth of the pores and the chimbs; (e) fully developed of the titania nanotube arrays. [52]

The initiation and growth of pores are associated with accelerated dissolution of TiO_2 with an influence of electric field. Many defects like impurities, dislocation, grain boundaries, or nonmetallic inclusions could cause a faster dissolution rate and lead to a pit growth [53, 54]. When Ti^{4+} cations are gotten out from the oxide surface that are caused by an applied field, Ti^{4+} cation vacancies can arise and accumulate to form high density voids in the oxide layer, which can help the propagation of pits [55, 56]. The pores are developed from

pits after dissolution, oxide at the electrolyte/oxide interface, and oxidation, titanium metal at the oxide/metal interface, are stable.

1. 1. 4 Anodization condition and annealing

For good appearance of titanium oxide array, anodization voltage is somewhat important. In Yahya's report, titanium oxide suitably evolute to anatase at 500℃ in regular Voltage of 60s.

After anodization period, array was dealt in high temperature annealing. Through annealing process, titanium oxide expand its crystallography and strength. In Figure 1. 7, recommended anodization condition is 60V anodization and about 500℃ annealing temperature.

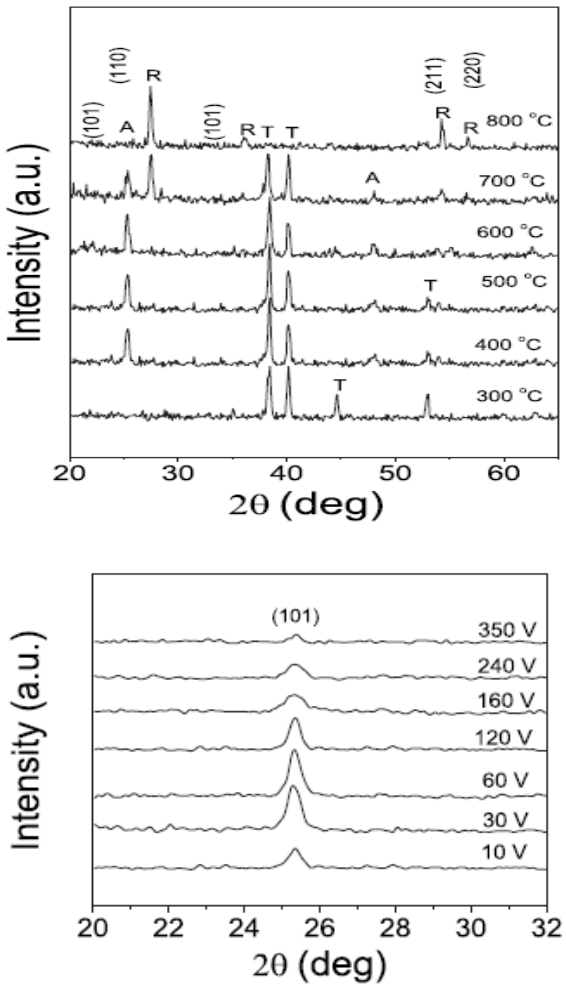

(a) (b)

Figure 1. 7. (a) GAXRD spectra of TiO_2 NTs grown at 0.7% acid concentration as a function of annealing temperature. Samples were annealed in temperature range of 300–800℃ with 100℃ step. A, R, and T refer to anatase, rutile, and titanium, respectively. (b) (101) anatase XRD diffraction peak of TiO_2 NTs as a function of anodization voltage. [46]

1. 2. Dye Sensitized Solar Cell

1.2.1. Overview

The first embodiment of modern day Dye-sensitized Solar Cell (DSC) dates back to late 1980s. [57] However, not until the fundamental work of Grätzel and O'Regan in 1991, [58] it was proven that DSCs can be a feasible alternative energy source. They built the first DSSCs which showed 7.1% energy conversion efficiency. [58] After that work, numerous studies had been reported. [60-68]

Although the power conversion efficiency of DSSCs is not as good as compared to other inorganic 1st and 2nd generation solar cells, it has an edge over them at some points.

In the normal operating temperature range of 25−65^{0}C, DSSCs efficiency is nearly temperature-independent. In diffuse sunlight or cloudy conditions, DSSCs shows even better efficiency than polycrystalline Si solar cell. Performance is less sensitive to the incident angle of the light radiation. Although a mass commercial production of DSSCs is still not available, it can be expected that it has a cost advantage over all thin film devices. Only low cost and abundantly available materials are needed. DSSCs materials are biocompatible and abundantly available.

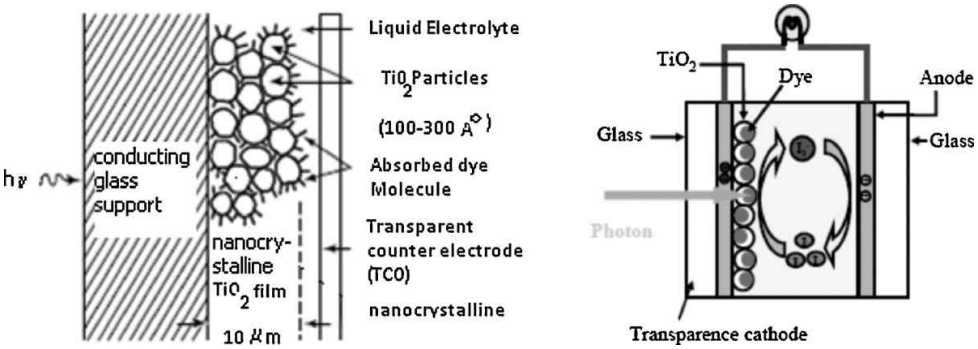

Figure 1. 8. Cross section of dye-sensitized solar cell [62, 67]

1. 2. 2. Components of DSSCs

DSSCs has four components, semiconductor, sensitizer(dye), electrolyte, counter electrode.

1. 2. 2. 1 Semiconductor

The semiconductor as a photoanode in DSSCs provides multi-function as supporter of sensitizer(dye) to load, and transporter of excited electrons from sensitizer to external circuit.

Among potential electron acceptors for DSSCs, TiO_2 is the most versatile. It delivers the highest efficiencies, is chemically stable, non-toxic, and available in large quantities. Generally, TiO_2 nanoparticles (NPs) have several crystal phase, such as rutile, anatase, and brookite. Its anatase nanocrystalline form gives the most efficiency

with optimization of surface area, porosity, pore diameter, transparency and film thickness. TiO_2 is the semiconductor of choice due to its wide bandgap, nanoporous structure with large surface area and, suitable HOMO and LUMO alignment with the electrolyte and dye respectively. The rutile phase has a bandgap of 3 eV, while 3.2 eV for anatase; corresponding to photon absorption edge of 413 and 388 nm. [60, 69, 70]

1. 2. 2. 2 Dye

The photo sensitizer dye is the heart of operation of DSSCs. The dye molecule commonly used in DSSCs are polypyridyl-type ruthenium (Ru) complexes such as namely N719 and N3 dye. [59, 60, 71, 72, 73] Upon sensitization of the semiconductor film, the dyes form a monomolecular coating, with the stoichiometry of the anchored photosensitizer as high as ~1:100 (Ru per Ti). [74] Stringent engineering of the dye is necessary for efficient light absorption, charge injection and collection of the cell. It is well-known that the Ru complexes absorb the visible light due to a metal to ligand charge transfer (MLCT) process. Furthermore, it has a proper excited and ground state energy levels, relatively long excited-state lifetime, and high chemical stability. [71]

1. 2. 2. 3 Electrolyte

In DSSCs, electrolyte act as reductor to regenerate of the oxidized dye. [75] The iodide/triiodide electrolyte system is commonly used. It's advantage is easy preparation, high conductivity, good permeability, and fast oxidation of I^- at the photoanode/electrolyte interface. [76, 78]

Incorporation of 4-tertbutylpyridine in the electrolyte increases the open-circuit voltage and fill factor by decreasing the dark current at the semiconductor-electrolyte junction.

The following relation holds for regenerative photo-electrochemical systems,

$$V_{OC} = \left(\frac{kT}{e}\right) \ln\left(\frac{I_{inj}}{n_{cb} K_{et} [I_3^-]}\right)$$

Where I_{inj} is the charge flux from sensitizer injection, K_{et} is the rate constant for triiodide reduction and n_{cb} is the electron concentration on the semiconductor surface. [60] Although the TiO_2 surface is covered by a dye monolayer, the reduction of triiodide by conduction band electrons causes the dark current. Due to its relatively small size the triiodide ions either cross the monolayer or have entrance to nanometer-sized pores into which the dye molecules cannot enter. In

the latter case, the surface of TiO_2 is exposed to redox mediator. 4-tert-butylpyridine effectively decreases the rate of the reduction of triiodide, increasing the open-circuit voltage of the cell. [75-83]

1. 2. 2. 4 Counter Electrode

Platinum coated FTO glass substrate is used to as the counter electrode for DSSCs. The counter electrode has a multiple role as a catalyst to regenerate the eletrolyte and electron collector from external circuit. [84] Thus, the counter electrode should have advantages of high catalytic activity and electrical conductivity. [85] Pt counter electrode fulfilled this purpose.

RF sputtered Pt layer showed a good performance, however, for a nanoporous titania film fully optimized for efficient light absorption, chemically deposited platinum from a solution of 0.05 M hexachloroplatinic acid can perform alike.

The electrode substrate TCO affects the cell performance in 2 ways. The sheet resistance of the FTO influences the series resistance of the cell and the transmittance control the light absorption. Considering sheet resistance, the lower the better, but lower FTO sheet resistance require thicker FTO layer causing reduced light transmittance and efficiency. [95, 98-100]

1. 2. 3 Basic Operating Principle

The DSSCs is the useful photovoltaic device that utilizes separate mediums for light absorption/carrier generation (dye) and carrier transport (TiO_2 nano-particles).

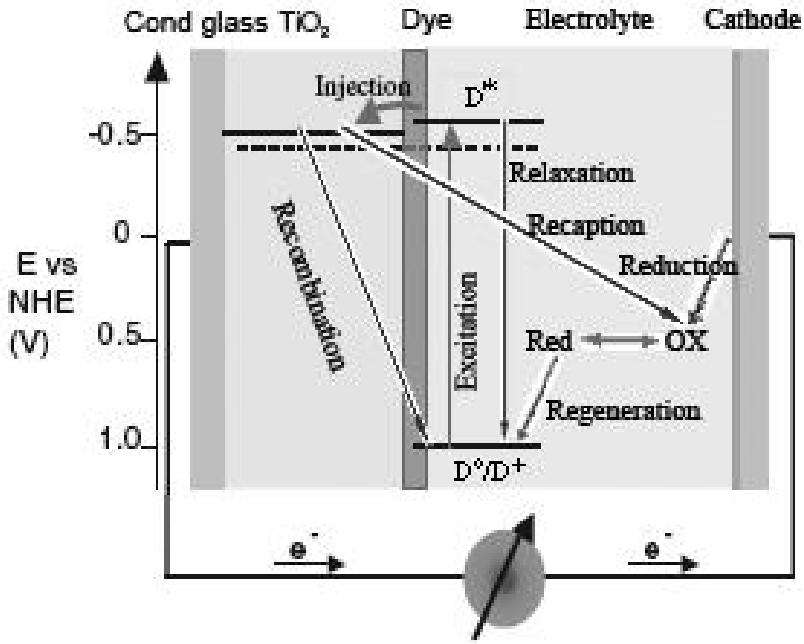

Fig. 1. 9. Principle of operation of DSSCs. [86]

DSSCs include a substrate of fluorine-doped SnO_2 conducting glass (FTO), a porous nanocrystalline semiconductor oxide (the most employed is TiO_2) film sensitized by a dye (typically bipyridine ruthenium complexes) for absorbing visible light, a redox electrolyte (usually an organic solvent containing a redox system, such as iodide/triiodide couple) layer for deoxidizing oxidized dye, and a

platinized cathode to collect electrons and catalyze the redox couple regeneration reaction [58, 62, 65].

The light-to-electricity conversion in a DSSC is based on the injection of electron from the photoexcited state of the sensitized dye into the conduction band of TiO_2. The dye is regenerated by electron donation from iodide in the electrolyte. The iodide is restored, in turn, by the reduction of triiodide at the cathode, with the circuit being completed via electron migration through the external load.

The voltage generated under illumination corresponds to the difference between the Fermi level of the electron in the TiO_2 and the redox potential of the electrolyte. Overall, the device generates electric power from light without suffering any permanent chemical transformation [58, 62, 87, 88].

The photoelectric chemical process in DSSC can be expressed as equations. (1)-(6).

$$TiO_2|S + hv \rightarrow TiO_2|S^* \quad \text{excitation} \quad (1)$$

$$TiO_2|S^* \rightarrow TiO_2|S^+ + e^- \ (CB) \quad \text{injection} \quad (2)$$

$$TiO_2|2S^+ + 3I^- \rightarrow TiO_2|2S + I_3^- \quad \text{regeneration} \quad (3)$$

$$I_3^- + 2e^-(Pt) \rightarrow 3I^- \quad \text{reduction} \quad (4)$$

$I_3^- + 2e^-(CB) \rightarrow 3I^-$ recaption(dark reaction) (5)

$TiO_2|S^+ + e^-(CB) \rightarrow TiO_2|S$ recombination(dark reaction) (6)

The photoexcited electron injects into the conduction band of TiO_2. [71, 89-91] The dark reaction equation (5) and (6) also occur during the light-to-electricity conversion, but do not play a remarkable negative effect on photovoltaic performance of DSSCs owing to their slow reaction speed compared with that of equation (2) [92-94].

The operation steps are the following.

1. 2. 3. 1 Excitation

The light is absorbed by a sensitizer dye molecule, it goes over an electronic state change from the ground (S) to the excited state (S*). The lifetime of the excited state is in the order of nanoseconds.

1. 2. 3. 2 Injection

The sensitizing dye molecules are adsorbed on the surface of a wide band gap semiconductor (typically TiO_2). Upon absorption of a photon (excitation), the dye gains the ability to transfer an electron to the conduction band of the semiconductor. The internal electric field of the nanoparticles causes the electron extraction and the dye becomes

oxidized (S^+). The injection rate constant is in the femtosecond range for singlet state.

1. 2. 3. 3 Diffusion in TiO_2

The nonporous TiO_2 film consists of spherical anatase particles of diameter ~20 nm. The presence of oxygen vacancies in the lattice makes it a weakly n-doped material. [71, 72] As the TiO_2 particle diameter is too small for electric field to build up, the dominant electron transport mechanism is diffusion via trapping and de-trapping.

1. 2. 3. 4 Iodine Reduction

The electron travels through the outer circuit performing work, reaches the back FTO electrode, and reduces the iodine in the electrolyte. The platinum layer on the FTO acts as a catalyst for the reduction. The dark cathode reaction:

$$I_3^- + 2e^- \rightarrow 3I^-$$

The iodine reduction can also occur at the excited dye molecules causing recombination of the photo-generated electrons. For efficient charge transfer, the rate of iodine reduction at the counter electrode has to be orders of magnitude faster than the recombination at the TiO_2/electrolyte interface.

1. 2. 3. 5 Dye Regeneration

The reduced iodide ion replenishes the highest occupied molecular orbital (HOMO) of the dye - regenerating its original form, and makes it ready for electron generation again.

The photoanode reaction:

$$2I^- \rightarrow I_2 + 2e^-$$

This prevents buildup of S^+, which could lead to the conduction band electrons going back to the dye molecules. The maximum output voltage equals to the difference between the Fermi level of the semiconductor and the redox potential of the mediator. [72]

Thus, the device is can produce electricity from light without undergoing any permanent physical and chemical change.

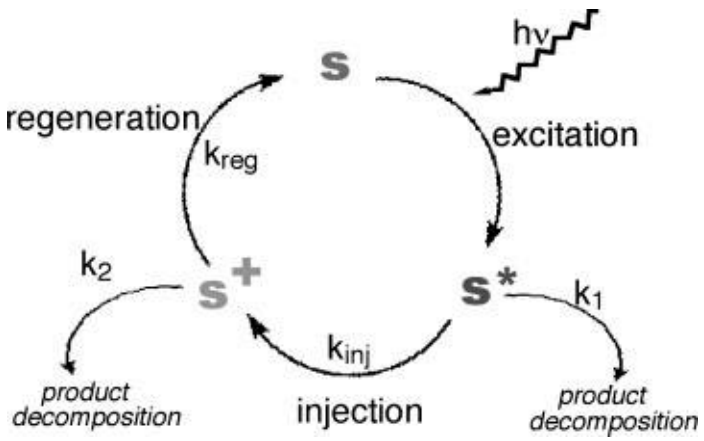

Figure 1. 10. The overall catalytic cycle of the sensitizer during DSSCs operation [68]

1. 2. 4 Solar Cell Terminologies

1. 2. 4. 1 Equivalent circuit of solar cells

A current source in parallel with a forward biased diode expresses the equivalent circuit of an ideal solar cell. Series and parallel resistances are added to account for various loss mechanisms.

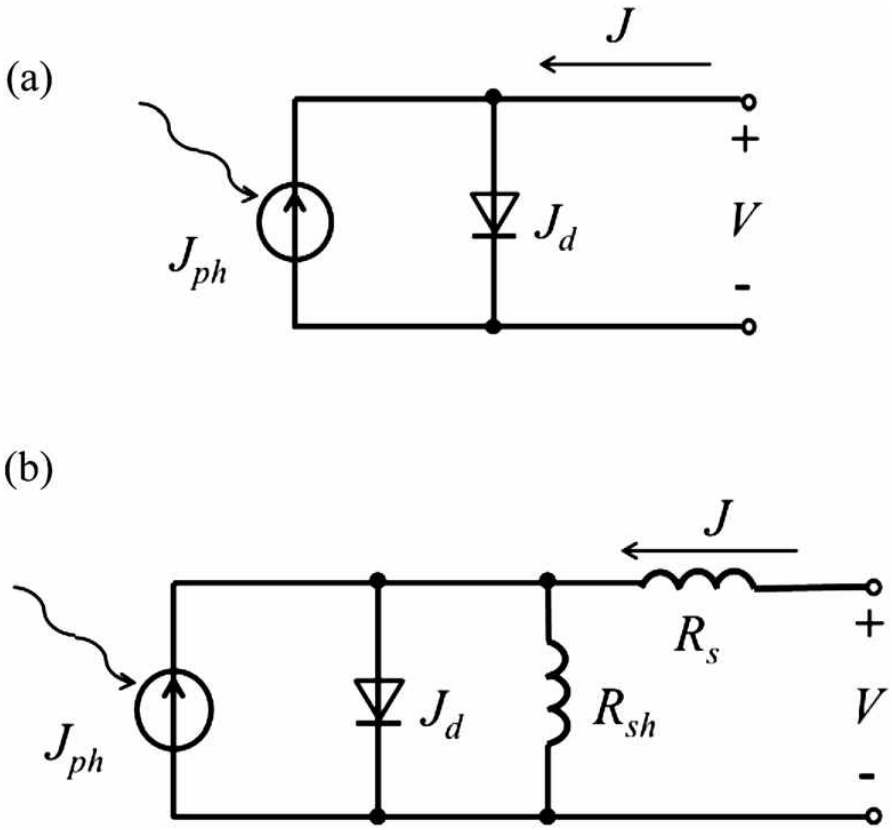

Figure 1. 11. Equivalent circuit of (a) an ideal solar cell and (b) a practical solar cell. [95]

Under illumination a solar cell works like a current source, providing a current density of J_{ph}. A proportion of this current counteracts the junction current of the diode, and the residual current flows to the load. According to Shockley's theory, the junction current density of the diode is presented by:

$$J_d = J_0[\exp(qV/k_BT) - 1]$$

(T : temperature, k_B : Boltzmann constant, J_0 : the reverse saturation current density (in a p–n junction solar cell, J_0 represents the current density of minority carriers, which is a summation of the hole current in the n region and the electron current in the p region), V : the output voltage)

Series resistance R_s and shunt resistance R_{sh} have to be taken into account in a practical solar cell, whose equivalent circuit is shown in Figure 1. 11(b). R_s is composed of the resistance of the bulk active layer, the resistance of electrodes and the contact resistance between the active layer and the electrodes, etc.

R_{sh} originates from various kinds of current leakage, such as current leakage in the p–n junction, current leakage from the edge of the cell, current leakage induced by impurities in the cell, etc.

1. 2. 4. 2 Short-circuit Current

In closed circuit, short-circuit Current is the current obtained from the cell when short-circuited or in other words when the load resistance is zero. Solar cell current is normally represented as current density, Jsc:

$$J_{SC} = \frac{I_{SC}}{A} \qquad (mA/cm^2)$$

where A is the effective area of the solar cell. [69]

1. 2. 4. 3 Open-circuit Voltage

Open-circuit voltage is the maximum voltage available from a solar cell and is obtained when a load with infinite resistance is attached to its terminals. It is a function of the semiconductor bandgap and charge recombination in the cell. For DSC the Voc is given by:

$$V_{OC} = \frac{E_{CB}}{q} + \frac{kT}{q}\ln\left(\frac{n}{N_{CB}}\right) - \frac{E_{redox}}{q} \qquad (volts)$$

where, n is the number of electron in TiO_2 conduction band and NCB is the effective density of states. [96] The first two terms defines the quasi-fermi level of TiO_2 and Eredox is the Nernst potential of the redox mediator.

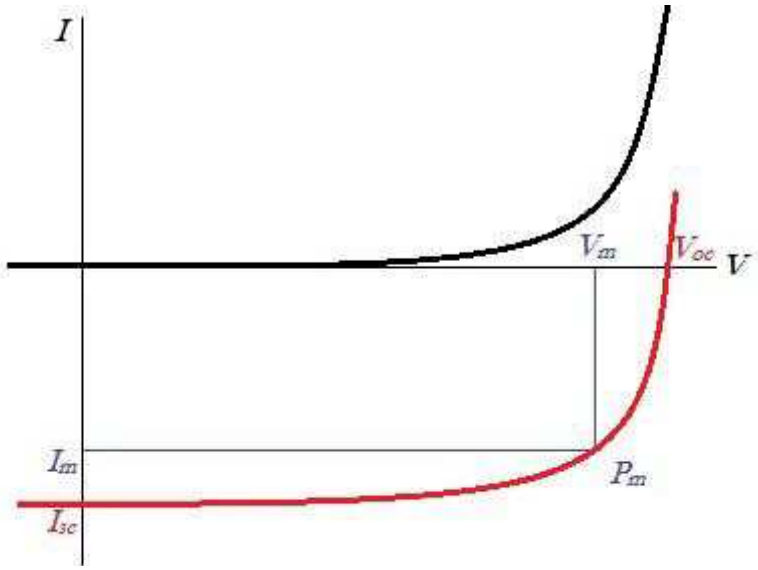

Light I-V response(below line) and dark I-V response(upper line).

Figure 1. 12. Typical current-voltage relationship of a solar cell. [95, 97]

1. 2. 4. 4 Series Resistance

Series resistance, R_S in a solar cell is the result of contact resistance and charge transfer resistance in the semiconductor material. Series resistance reduces the fill factor affecting the maximum power output, while excessively high value of R_S can also reduce the short-circuit current. The open-circuit voltage is not affected since, at V_{OC} the total

current flow through cell itself and hence through the series resistance is zero. An approximation of the series resistance can be determined from the slope of the IV curve at the open-circuit voltage point. [98, 99, 100]

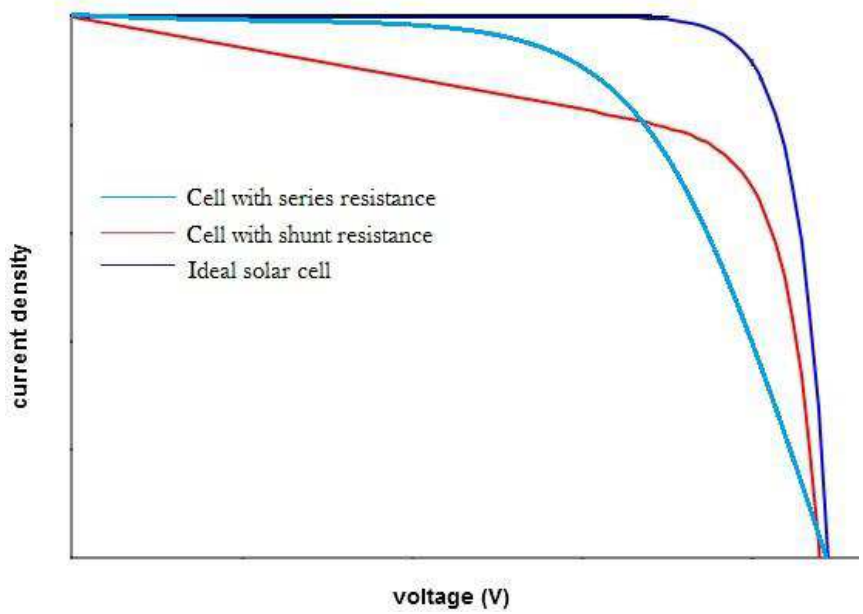

Figure 1. 13. Current-voltage response of a solar cell with series and shunt resistance.

1. 2. 4. 5 Shunt Resistance

Low shunt resistance, R_{sh} provides an alternate current path for the photo-generated current causing significant power loss. The effect of low shunt resistance is reduced fill factor and lower open-circuit voltage affecting the maximum power output. The short-circuit voltage is not affected unless for a very low value, since at J_{SC} the total current flows

through the outer path and hence through the shunt resistance is low. An approximation of the shunt resistance can be calculated from the slope of the I-V curve at the short circuit current point. [95]

1. 2. 4. 6 Fill Factor

The fill factor (FF) is a measure of the maximum power output from a solar cell. It represents the squareness of the I-V curve and is defined as the ratio of the maximum power to the product of V_{OC} and I_{SC} for the solar cell:

$$FF = \frac{V_m \times I_m}{V_{OC} \times I_{SC}}$$

Where, V_m and I_m are the voltage and current at maximum power point. Fill factor, being a ratio of the same physical parameters, has no unit. Fill factor is a function of the series and shunt resistance of the solar cell. For D_{SC}, it reflects the extent of electrical and

electrochemical losses during cell operation. To obtain higher fill factor improvement of the shunt resistance and decrement of the series resistance, with reduction of the overvoltage for diffusion and charge transfer is required. [101]

1. 2. 4. 7. Efficiency

The efficiency of a solar cell is defined as the ratio of maximum electrical energy output to the energy input from the sun. Thus the mathematical definition of Efficiency:

$$\eta = \left(\frac{V_{oc} \times I_{sc} \times FF}{P_{in}}\right)$$

where, Pin is the power input from the sunlight. Efficiency is generally expressed in percentage. [89]

1. 2. 4. 8. Quantum Efficiency

Quantum efficiency (QE) or 'External Quantum Efficiency (EQE)', sometimes also referred to as Incident Photon to Charge Carrier Efficiency (IPCE) is a measure of how efficient a solar cell is in producing photo-generated charge at a given frequency. It is defined as

the photocurrent density produced in the external circuit under illumination condition, divided by the photon flux of excitation wavelength. [71]

For DSSCs, the term is defined as:

$$IPCE = \frac{\text{photocurrent density}}{\text{wavelengh} \times \text{photon flux}}$$

$$IPCE\ (\lambda) = LHE(\lambda) \times \phi(inj) \times \eta(coll)$$

Where, LHE(λ) is the light-harvesting efficiency at excitation wavelength λ, Φ(inj) is the electron injection quantum yield for the excited sensitizer to the semiconductor oxide conduction band and η (coll) is the efficiency for the collection of electrons. [71, 102]

1. 3 Additional strategies to enhance the efficiency of DSSCs

1. 3. 1 Blocking Layer

Charge recombination is one of the main reasons of lower current for D_{SC}. Recombination occurs at both Electrode/Electrolyte and TiO_2/Electrolyte interface. A compact blocking layer of TiO_2 by RF sputtering [103] or spray pyrolysis [104] between the conducting electrode and the nanocrystalline TiO_2 layer can effectively prevent the recombination at electrode/electrolyte interface. Introduction of this layer prevents electrolyte from reaching the electrode (increases J_{SC}) and also enhance electron transport from nanocrystalline titania to the electrode (increases V_{OC}). This blocking layer is absolutely necessary for planar organic dyes, while ruthenium based sensitizers can perform this anode insulation themselves against recombination losses. [105, 106]

A rather cost effective and easier way of incorporating this blocking layer is through hydrolysis of $TiCl_4$. $TiCl_4$ treatment on FTO substrate is found to suppress the dark current, shifting its commencement by some hundred millivolts. This is due to a positive shift in the conduction band edge of highly doped SnO_2 by about 0.5 V which results in a higher electron density in the FTO substrate. [107]

1. 3. 2 $TiCl_4$ Treatment

To reduce charge recombination at TiO_2/electrolyte interface, another blocking layer of TiO_2 is implemented via $TiCl_4$ treatment with subsequent annealing. The average pore diameter and specific surface area decreases with the $TiCl_4$ treatment, because of the surface epitaxial growth of TiO_2, resulting in particle-necking and a new TiO_2 layer. The increase of the inter-particle necking will reduce the resistance in electron transport through the nanoparticles reducing the recombination probability. At the same time, it improves the surface roughness factor and light absorbance. [107] These lead to a decrease in the dark current and an increase of the photocurrent. [108]

Hydrolysis from the acidic $TiCl_4$ solution prevents deposition of impurities in the $TiCl_4$, such as Fe^{3+}, because of the higher solubility of iron oxide compared to TiO_2. The P25 powder, which is the most common source of producing nanocrystalline Titania, contains as far as 100 ppm of Fe_2O_3, which is known for causing interference with electron injection from the excited state of the dye. The $TiCl_4$ treatment covers this relatively impure semiconductor core with a TiO_2 thin layer of ultra-high purity. This improves the injection efficiency and the blocking character of the semiconductor-electrolyte junction. [60, 83]

Theoretically, this overlayer can be formed of other metal-oxide films (examples include MgO, ZnO, Al_2O_3, and Nb_2O_5) which have conduction band edges higher than TiO_2. [109]

The performance of these oxides depends on their protonation / deprotonation capability of the TiO_2 surface, which enhances dye adsorption and a positive shift of the TiO_2 flat band. [110] For example, Al_2O_3 being basic, will tend to deprotonate the TiO_2 film, resulting in the improvement in cell performance.

1. 3. 3 Light Scattering Layer

One limitation of the sensitizing dyes is their poor performance in the near infra-red spectrum of light. A way of improving this is - by introducing an additional light scattering layer of larger titania particles. These can be mixed with or screen-printed on top of the film of 15-30nm sized TiO_2 particles. This allows the scattered photons to be contained in the film by means of multiple reflections, increasing their optical path length substantially beyond the film thickness. Consequently, the solar light absorption is enhanced, especially in the red to near-IR regions. With the use of 200-400nm sized anatase particles as light-scattering centers, an increment of the J_{SC} by 3-4

mA/cm^2 was observed for N719-based DSCs because of the enhanced light absorption.

Moreover, approximately 4% loss occurs because of the reflection of incident light on the glass substrate. This can be partially overcome by introducing an anti-reflecting film, which can also act as a UV cut-off filter. [107, 111-131]

1. 4 Plasmonic DSSCs

1. 4. 1. Surface plasmon resonance for solar cells

Plasmonic solar cells are photovoltaic devices that are used the noble metal surface plasmons. Surface plasmons are the collective oscillation of excited free electrons.

Most of solar cells have a weak absorber. To trap the more absorption and long wavelength of light, the morphology of substrate is etched like pyramids with a size of 2-10 mm that is about wavelength-scale texture. This structure not only increases the light trapping to solar cell, but also increases the surface recombination and low material quality. [132, 133]

Another is to use the noble metal nanoparticles in the solar cells. The

light is absorbed and scattered from noble metal nanoparticles that is excited at the surface plasmon resonance. It has been based on Raman scattering that can be increased by order of magnitude when the metal nanoparticles are used [134, 135].

Surface plasmon resonance (SPRs) are coherent oscillations of free electrons at the boundaries between metal and dielectric which are often categorized into two classes: (1) propagating surface plasmons (PSPs), which generate at the metal film and (2) localized surface plasmons (LSPs), which generate at the metal NPs. [136-139]

In the case the case of PSPs, surface electromagnetic field propagates along the dielectric interface of metal in the x-/y-directions, but decays exponentially in the z-direction [137, 140, 141]

Whereas in LSPs, metallic NPs interact with light when they are much smaller than the incident wavelength, leading to a polarization at the surface of metal NPs. Consequently, induce a strong enhancement of electromagnetic filed in the near-field region (resonance amplification), polarization make oscillate electrons locally at the surface of metal NPs. Therefore, light absorption can be enhanced strongly, as depicted in figure [137, 140, 141]

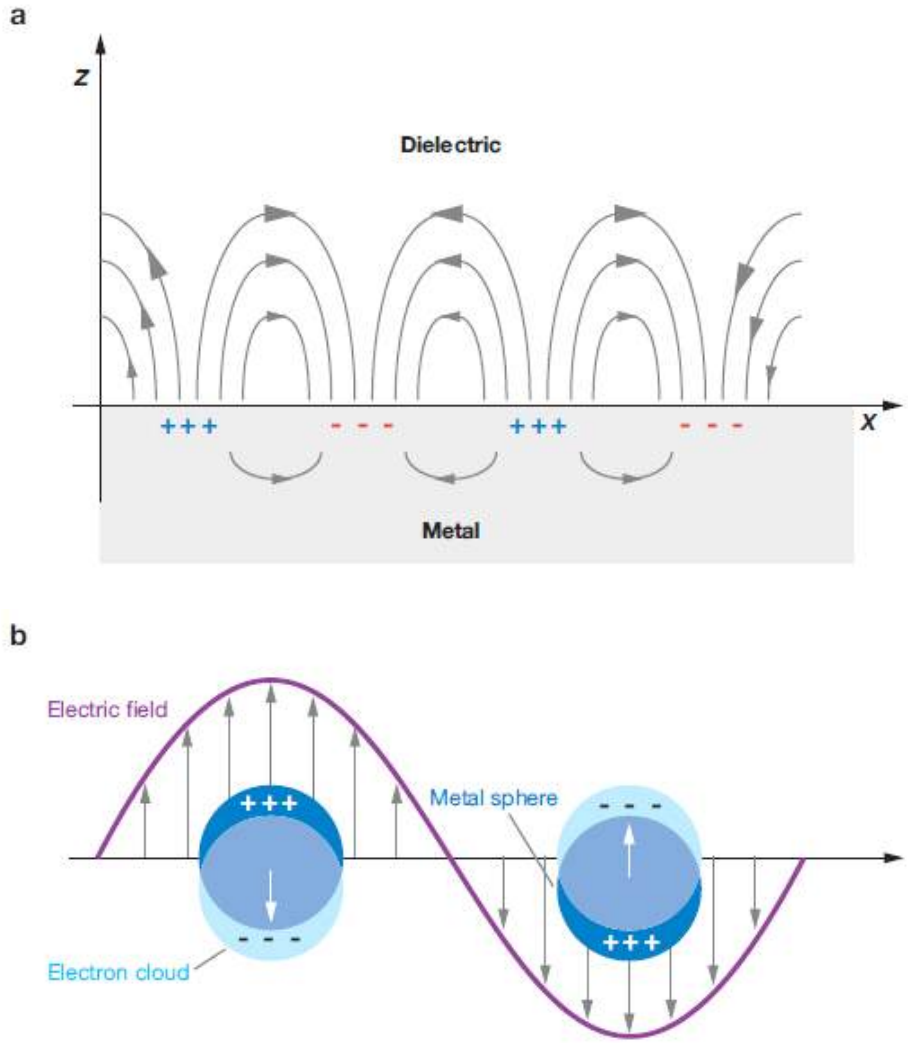

Figura 1. 14. Schematic diagrams illustrating (a) a surface plasmon polariton (or propagating plasmon) and (b) a localized surface plasmon. [140]

1. 4. 2 Localized surface plasmon resonance

Localized surface plasmons (LSPs) are associated with the collective oscillations of electrons confined locally by metal nanostructures. The most representative examples of LSPs are metal NPs. The particle plasmons are excited when the frequency of the incident photons matches the resonance frequency of the NPs. Their resonance wavelength depends on the particle shape, size, and the dielectric parameters of the surrounding environment. From the quasistatic approximation, the polarizability (P) of a spherical NP can be expressed as:

$$\mathrm{P} = 4\pi a^3 \frac{\varepsilon - \varepsilon_m}{\varepsilon + 2\varepsilon_m} \quad [142]$$

Where a is the diameter of the NP and ε and ε_m are the dielectric constants of the surrounding dielectric medium and of the metal NP itself, respectively. [142] From equation, we conclude that the value of P reaches its maximum when ε_m is equal to $-2\varepsilon_m$, resulting in a resonance condition. Because the excited plasmons are localized and cannot propagate within the nanostructure, this process is known as localized surface plasmon resonance (LSPR).

1. 4. 3. Plasmonic effects in solar cells

Proposal mechanism of plasmonic solar cells is to explain photocurrent improvement by metal nanoparticles that are incorporated into or on solar cells as shown in Figure 1. 15. One is scattering from the metal nanoparticles. The role of metal nanoparticles is used as subwavelength scattering elements to couple and trap propagating plane waves from the Sun into semiconductor thin film, by folding the light into a thin absorber layer as shown in Figure 1. 15. (a). In inorganic plasmonic solar cells, the photocurrent improvement is increased by scattering from metal nanoparticles. Another is near-field enhancement from metal nanoparticles. Metal nanoparticles are used as subwavelength antennas in which the plasmonic near field is coupled to the semiconductor, increasing its effective absorption cross-section as shown in Figure 1. 15. (b). In organic plasmonic solar cells, the photocurrent improvement is increased by near-field enhancement. The other is direct generation of charge carriers in the semiconductor substrate. A corrugated metallic film on the back surface of a thin photovoltaic absorber layer can couple sunlight into surface plasmon polaritons (SPP) modes. Surface plasmon polaritons are supported at the metal/semiconductor interface as well as guided modes in the semiconductor slab. Accordingly, the light is converted to photocarriers in the semiconductor as shown in Figure 1. 15. (c). [143].

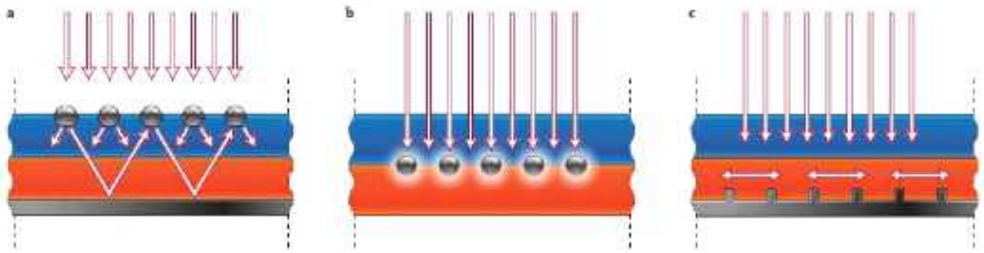

Figure 1. 15. Plasmonic light-trapping geometries for thin-film solar cells. (a) Light trapping by scattering from metal nanoparticles at the surface of the solar cell. Light is preferentially scattered and trapped into the semiconductor thin film by multiple and high-angle scattering, causing an increase in the effective optical path length in the cell. (b) Light trapping by the excitation of localized surface plasmons in metal nanoparticles is embedded in the semiconductor. The excited particles' near-field causes the creation of electron−hole pairs in the semiconductor. (c) Light trapping by the excitation of surface plasmon polaritons at the metal/semiconductor interface. A corrugated metal back surface couples light to surface plasmon polariton or photonic modes that propagate in the plane of the semiconductor layer [143].

Chapter 2 Experimental Section

2. 1. Preparation of TiO_2 nanotubes arrays

2. 1. 1. Materials

Titanium plate (Alfa aesar, 99.7% purity, 0.25 mm thickness), ammonium fluoride (NH_4F, Showa Chemical Co., 97.0%), ethylene glycol (Daejung chemical, 99%), hydrogen peroxide (H_2O_2, Daejung chemical, 30%), fluorine-doped tin oxide(FTO) glass (Pilkington, TEC-A7), Titanium diisopropoxide bis(acetylacetonate) solution (Aldrich, 75 wt% in isopropanol), n-butanol (Daejung chemical, 99%), TiO_2 paste (Ti-Nanoxide T/SP, solaronix), scattering TiO_2 paste (18NR-AO, Dyesol), silver nitrate ($AgNO_3$, Aldrich, 99%) titanium chloride ($TiCl_4$, Aldrich, 0.09 M in 20% HCl), Dye (cis-diisothiocyanato-bis (2,2'-bipyridyl-4,4'-dicarboxylato) ruthenium(II) bis(tetrabutylammonium), N719, Solaronix), chloroplatinic acid hexahydrate($H_2PtCl_6 \cdot 6H_2O$, Aldrich), 1-butyl-3-methyl-imidazolium iodide (BMII, Aldrich, 99%), iodine (I_2, Aldrich, 99%), guanidium thiocyanate (GSCN, Aldrich, 99%), 4-tertbutylpyridine (TBP, Aldrich, 96%), acetonitrile (CH_3CN, Aldrich, 99.8%), valeronitrile ($CH_3(CH_2)_3CN$, Aldrich, 99.5%)

2. 1. 2. Titanium (Ti) Anodization

TiO_2 nanotubes were fabricated by anodizing thin Ti plates (99.7 % purity, Alpha, 2.5 cm x 4.0 cm x 200 μm) in an electrolyte composed of 0.8 wt% of NH_4F and 2 vol% of H_2O in ethylene glycol at 25℃ and at a constant applied voltage of 60 V DC for 2 h as shown in Figure 2. 1. [45, 144, 145].

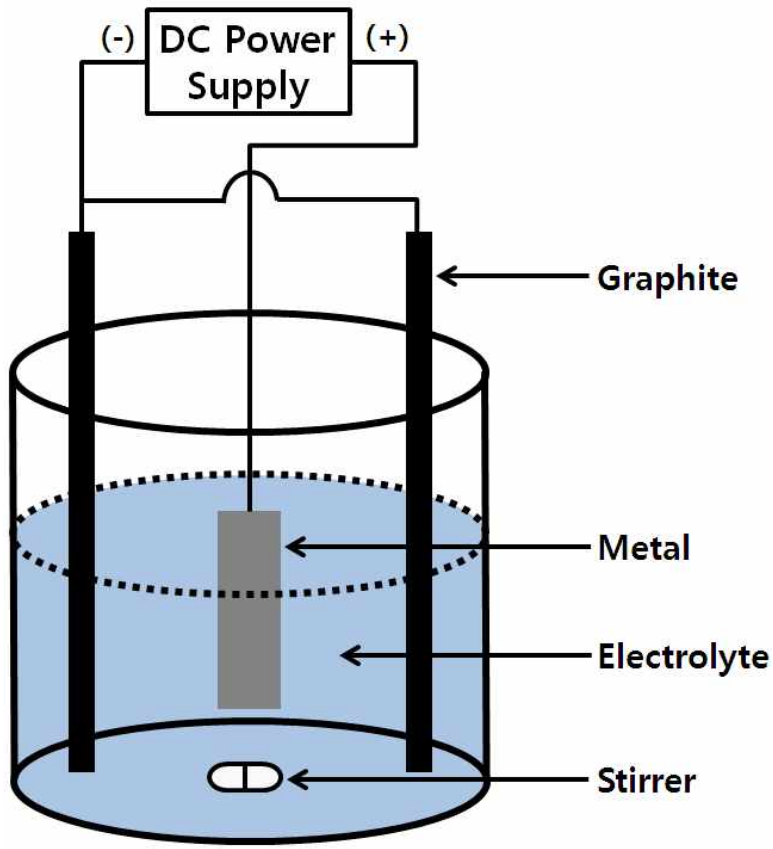

Figure 2. 1. Schematic diagram of titanium (Ti) anodization.

2. 1. 3. Preparation of free-standing crystallized TiO_2 nanotubes

The Ti plate-formed TiO_2 nanotubes arrays were annealed at 450℃ for 1 h under an ambient atmosphere to improve their crystallinity. To detach the free-standing TiO_2 nanotube arrays from the Ti plate, a second anodization was done at a constant applied voltage of 30 V DC for 10 min, and then the plate was immersed in the 10 % of H_2O_2 for 24 h [146].

2. 1. 4. Preparation of free-standing crystallized TiO_2 nanotube arrays

To prepare TiO_2 nanotube arrays, the barrier layer of TiO_2 nanotubes was etched. However, free-standing crystallized TiO_2 nanotubes was very stable in chemicals. So the barrier layer was not etched by acidic or basic condition.

The barrier layer of TiO_2 nanotubes was removed by ion milling with Ar^+ bombardment for several minutes to prepare open-ended freestanding TiO_2 nanotube arrays. [146, 147].

2. 2. Fabrication of dye-sensitized solar cells based on TiO_2 nanotubes array with scattering layer

2. 2. 1. Overview of DSSCs manufacturing

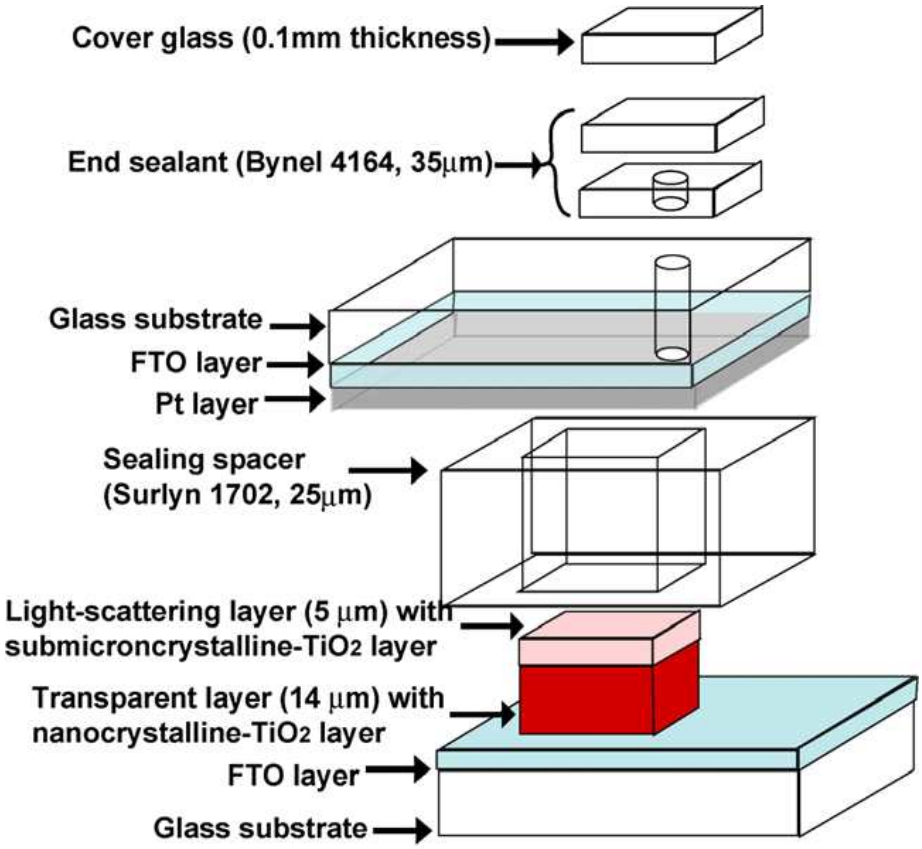

Figure 2. 2. Configuration of the dye sensitized solar cells. [107]

2. 2. 2. Preparation of blocking layer

A TiO_2 blocking layer was formed on fluorine-doped tin oxide (FTO) glass by spin-coating with 5 wt% of titanium di-isopropoxide bis(acetylacetonate) in butanol and then by heating at 450℃ for 30 min under ambient conditions. [106].

2. 2. 3. Introduction to TiO_2 nanotubes arrays on FTO glass

TiO_2 nanotubes or nanomembranes were attached on the fluorine-doped thin oxide (FTO) glass formed a TiO_2 blocking layer on its surface by using TiO_2 nanoparticles viscous paste. The viscous TiO_2 paste (from Solaronix) was printed onto FTO glass by the doctor blade technique and the closed- and open-ended TiO_2 nanotube arrays were introduced on the paste. The substrate was then sintered at 450℃ for 1 h under ambient conditions.

2. 2. 4 Adapting scattering layer

The TiO_2 scattering layer (~400nm-diameter particles) was coated onto the closed- and open-ended TiO_2 nanotube arrays using a doctor blade and sintered at 450℃ for 30 min under ambient conditions.

2. 2. 5. $TiCl_4$ treatment

TiO_2 nanotubes arrays on FTO glass were treated with $TiCl_4$ by dipping the plate in a 0.1 M $TiCl_4$ aqueous solution for 30 min and then sintered at 450℃ for 30 min. By the sintering process, the crystal structure of TiO_2 nanoparticles was changed to anatase.

2. 2. 6. Dye absorption

Dye molecules were absorbed by immersing the nanotube film-attached FTO glass plate in an ethanol solution of 0.5 mM cis-diisothiocyanato-bis(2,2'-bipyridyl-4,4'dicarboxylato) ruthenium(II) bis (tetrabutylammonium), (N719, Solaronix), at 50℃ over 8 h.

2. 2. 7. Electrolyte

The composition of the electrolyte was as follows: 0.7 M 1-butyl-3-methyl-imidazolium iodide (BMII), 0.03 M I_2, 0.1 M guanidium thiocyanate (GSCN), and 0.5 M 4-tertbutylpyridine (TBP) in a mixture of acetonitrile and valeronitrile (85:15 v/v).

2. 2. 8. Counter electrode

The counter-electrode was prepared by sputtering Pt on FTO glass or prepared by spin-coating the H_2PtCl_6 in isopropanol on FTO glass and then sintering at 400℃ for 20 min [106].

2. 2. 9. Fabrication of DSSCs

The working electrode was further sandwiched with the Pt-coated FTO glass, separated by a 60-μm-thick hot-melt spacer.

2. 3. Fabrication of DSSCs with freestanding TiO_2 nanotube arrays with channels containing Ag NPs

2. 3. 1. Same the former process of free standing TiO_2 nanotube arrays with scattering layer

Former process of free standing TiO_2 nanotube arrays with scattering layer, preparation of blocking layer and introduction to TiO_2 nanotube arrays on FTO glass, are same.

2. 3. 2. Ag nanoparticle formation

The substrate was dipped in 0.3 mM $AgNO_3$ aqueous solution and exposed to 254 nm UV irradiation for reduction of Ag cations.

2. 3. 3. Same the latter process of free standing TiO_2 nanotube arrays with scattering layer

Latter process of free standing TiO_2 nanotube arrays with scattering layer, adapting scattering layer, $TiCl_4$ treatment, dye absorption,

electrolyte filling, preparation of counter electrode and fabrication of DSSCs, are same.

2. 4. Characterization

2. 4. 1. FE-SEM

The morphology and thickness of the free-standing TiO_2 nanotube arrays, which were TiO_2 nanotube arrays after detachment from the Ti plate, were analyzed using a field emission scanning electron microscope (FE-SEM, JSM-6330F, JEOL Inc.).

2. 4. 2. TEM

The morphology, thickness, size, and presence of Ag NPs in the channel of freestanding TiO_2 nanotube arrays were confirmed using a field emission scanning electron microscope (FE-SEM, JSM-6330F, JEOL Inc.) and the high angular annular dark field (HAADF) technique with a scanning transmission electron microscope (TEM) (JEM-2200FS, JEOL).

2. 4. 3. Solar simulator

The current density－voltage (I－V) characteristics of the DSSCs were measured using an electrometer (KEITHLEY 2400) under AM 1.5 illumination (100 mW/cm2) provided by a solar simulator (1 kW xenon with AM 1.5 filter, PEC-L01, Peccel Technologies).

2. 4. 4. Incident photon-to-current conversion efficiency (IPCE)

The incident photon-to-current conversion efficiency (IPCE) was measured using McScience (model K3100) with reference to the calibrated diode. A 300 W xenon lamp was used as light source for generation of a monochromatic beam. The bias light was supplied by a 150 W halogen lamp.

Chapter 3

Improved energy conversion efficiency of dye-sensitized solar cells fabricated using open-ended TiO_2 nanotube arrays with scattering layer

3. 1 Overall view of free standing TiO_2 nanotube arrays DSSCs

Dye-sensitized solar cells (DSSCs) have attracted immense interest due to their high energy conversion efficiency and low cost [58, 62, 107]. However, the energy conversion efficiency of DSSCs still needs to be improved so that it compares favorably with conventional photovoltaic devices [148]. There are several parameters that can be investigated, including the dimensionality of TiO_2 for electron transport [149, 150], light-harvesting capability [151, 152], molar absorption coefficiency [153], energetically suitable HOMO－LUMO levels [154], available surface area for dyes [155], transport kinetics of the electrons [156], regeneration by a redox couple [157], and losses due to recombination and back reactions [158].

TiO_2 nanotubes can enhance electron transport and charge separation by creating direct pathways and accelerating the charge transfer between interfaces [144-146, 159-163]. These properties make them an attractive candidate for DSSC applications. TiO_2 nanotube arrays that are prepared by electrochemical anodization have a highly oriented and vertically aligned tubular structure [155, 156]. Thus, the arrays have a high degree of electron transport and minor charge recombination in comparison to TiO_2 nanoparticle films [164]. Hence, although current DSSCs fabricated using TiO_2 nanotube arrays have a low energy conversion efficiency as compared to DSSCs fabricated using TiO_2

nanoparticle films, they have immense potential. Recently, we prepared DSSCs using open-ended TiO_2 nanotube arrays and demonstrated that nanotube arrays whose barrier layers were removed by ion milling have 24% higher energy conversion efficiency as compared with DSSCs fabricated using TiO_2 nanoparticle films [163].

Introducing a scattering layer such as TiO_2, ZrO_2, or SiO_2 can increase the total energy conversion efficiency of DSSCs [165]. TiO_2 is a good material to use for a scattering layer due to its chemical stability and dye adsorption capability; hence, several DSSCs fabricated using TiO_2 nanoparticle films use a TiO_2 scattering layer on the active layer.

To the best of our knowledge, TiO_2 nanotube arrays have not been combined with scattering layers. In this paper, we report the improved energy conversion efficiency of DSSCs using open-ended TiO_2 nanotube arrays with a TiO_2 scattering layer. In this study, we compared the energy conversion efficiency of 1) closed- and open-ended TiO_2 nanotube arrays 2) with and without a TiO_2 scattering layer. In addition, we compared the energy conversion efficiency of fabricated DSSCs treated with $TiCl_4$ to untreated DSSCs.

3. 2. Characteristics of closed- and open-ended TiO_2 nanotube arrays

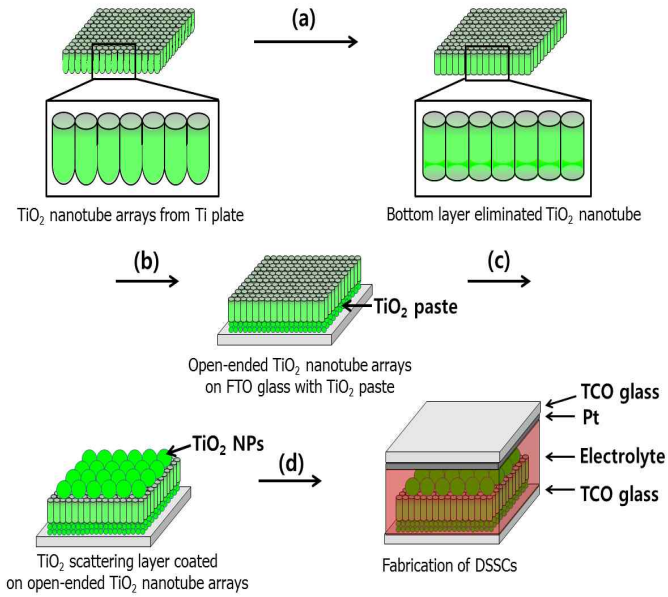

Figure 3. 1. Overall scheme of fabrication of DSSCs using the closed- or open-ended TiO_2 nanotube arrays. (a) Elimination of the bottom layer of closed-ended TiO_2 nanotube arrays by ion milling, (b) introduction of the closed- or open-ended TiO_2 nanotube arrays on FTO glass with TiO_2 paste, (c) coating the TiO_2 scattering layer on closed-ended or open-ended TiO_2 nanotube arrays by doctor blade, and (d) fabrication of DSSCs.

Figure 3. 1. shows the fabrication flow of the DSSCs using the closed- and open-ended TiO_2 nanotube arrays with the TiO_2 scattering layer for improved energy conversion efficiency. After sintering at 450℃ for 1 h under ambient conditions, the TiO_2 nanotube arrays have a crystalline form similar to anatase.

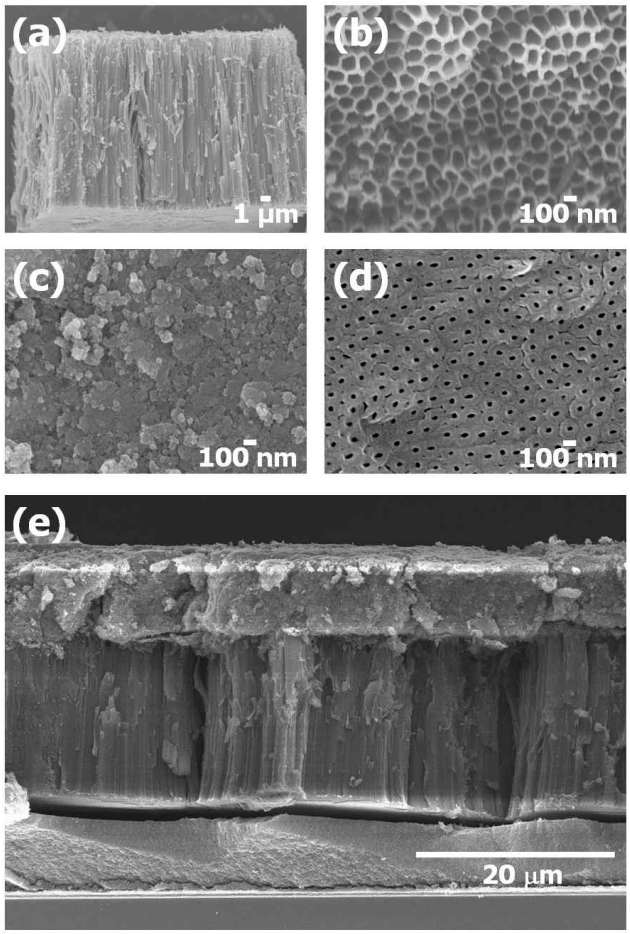

Figure 3. 2. FE-SEM images of (a) side view of TiO_2 nanotube arrays, (b) top view of TiO_2 nanotube arrays, (c) bottom view of the closed-ended TiO_2 nanotube arrays, (d) bottom view of open-ended TiO_2 nanotube arrays after ion milling, and (e) side view of TiO_2 nanotube arrays on FTO glass with TiO_2 nanoparticles and TiO_2 scattering layer.

SEM images of the side, top, and bottom of the free-standing TiO_2 nanotube arrays are shown in Figures 3. 2a, b, and c, respectively. The length of the free-standing TiO_2 nanotube arrays was approximately 18 μm, as shown in Figure 3. 2a. The upper pores were well ordered and their diameter was ca. 100 nm. The morphology of the bottom layer under the closed-ended TiO_2 nanotube array was very rough due to chemical etching with the H_2O_2 solution after secondary anodization, as shown in Figure 2c.

To prepare the open-ended TiO_2 nanotube arrays, the bottom layer of the closed-ended TiO_2 nanotube array was eliminated by ion milling to remove the barrier layer. Most of the bottom tips were opened after ion milling for 90 min and they had an approximate diameter of 20 nm, as shown in Figure 3. 2d. Figure 3. 2e shows the closed- and open-ended TiO_2 nanotube arrays on FTO glass after attachment using a TiO_2 paste and sintering at 450℃ for 1 h under ambient conditions. The TiO_2 scattering layer was coated onto the closed- and open-ended TiO_2 nanotube arrays using a doctor blade and then the dye (N719) was adsorbed. DSSCs were fabricated by assembling the working electrode (the closed- and open-ended TiO_2 nanotube arrays with TiO_2 scattering layer) and the counter electrode (Pt).

3. 3 Performance Measurements of the DSSCs which have closed-/open-ended TiO_2 nanotube arrays with the TiO_2 scattering layer

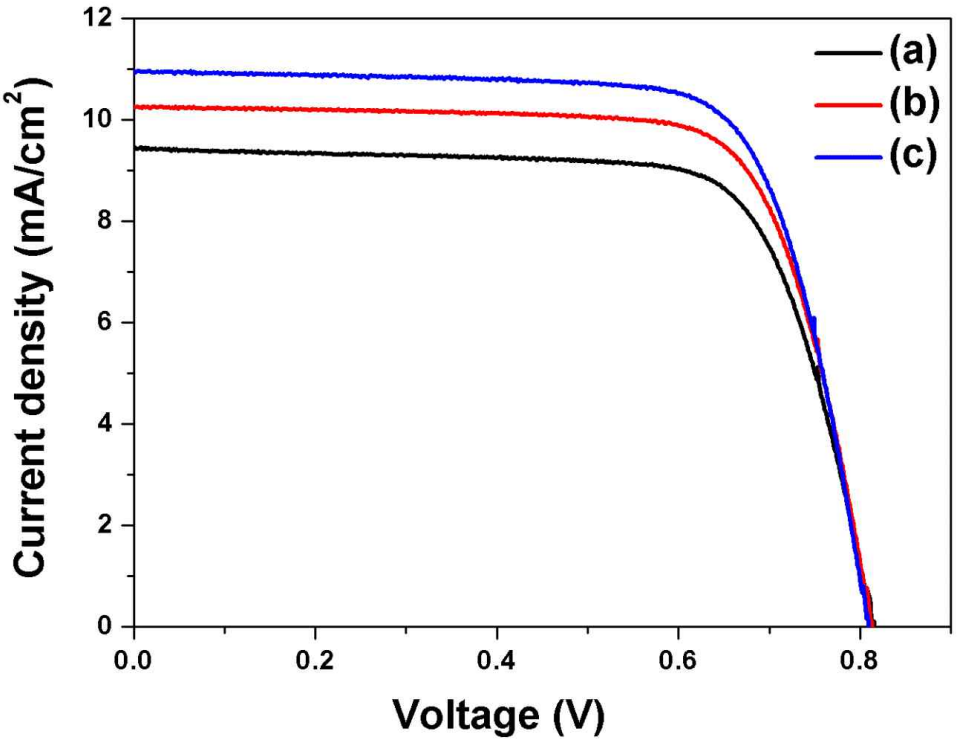

Figure 3. 3. I−V curves of DSSCs fabricated using (a) the closed-ended TiO_2 nanotube arrays, (b) the closed-ended TiO_2 nanotube arrays with the TiO_2 scattering layer, and (c) the closed-ended TiO_2 nanotube arrays with the TiO_2 scattering layer treated with $TiCl_4$.

Figure 3. 3. presents the current density−voltage curves of three different DSSCs fabricated using the closed-ended TiO_2 nanotube arrays attached to the FTO glass using TiO_2 paste. The measurements were taken using AM 1.5-simulated sunlight.

Table 3. 1. Photovoltaic properties of DSSCs fabricated using the closed-ended TiO_2 nanotube arrays

	Jsc (mA/cm^2)	Voc (V)	ff	η (%)
Closed-ended TiO_2 nanotube arrays	9.44	0.82	0.73	5.63± 0.14
Closed-ended TiO_2 nanotube arrays with TiO_2 scattering layer	10.24	0.81	0.74	6.17± 0.18
Closed-ended TiO_2 nanotube arrays with TiO_2 scattering layer treated with $TiCl_4$.	10.96	0.81	0.74	6.54± 0.20

The values of the open-circuit voltage (Voc), short-circuit current (Jsc), fill factor (ff), and energy conversion efficiency (h) are summarized in Table 3. 1. For the DSSC fabricated using just the

closed-ended TiO_2 nanotube arrays, the energy conversion efficiency was 5.63 ± 0.14%. For the DSSC fabricated using the closed-ended TiO_2 nanotube arrays and the TiO_2 scattering layer, the energy conversion efficiency was 6.17 ± 0.18%.

By introducing the TiO_2 scattering layer on the closed-ended TiO_2 nanotube arrays, the energy conversion efficiency improved significantly, with a 9.59% enhancement. When the closed-ended TiO_2 nanotube arrays with the TiO_2 scattering layer were treated with $TiCl_4$, the energy conversion efficiency increased from 5.63 ± 0.14% to 6.54 ± 0.20%, corresponding to a 16.2% enhancement due to increasing dye adsorption on the surface of the TiO_2 nanotube arrays [146].

By introducing the TiO_2 scattering layer on the closed-ended TiO_2 nanotube arrays, the energy conversion efficiency was improved due to increased light harvesting by the scattering layer.

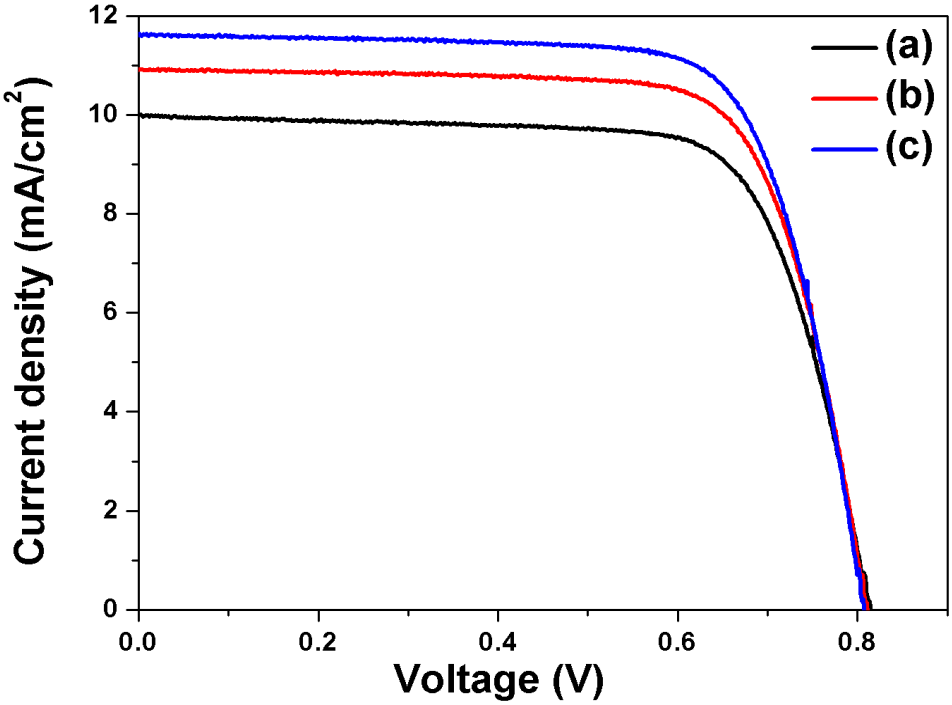

Figure 3. 4. I−V curves of DSSCs fabricated using (a) the open-ended TiO_2 nanotube arrays, (b) the open-ended TiO_2 nanotube arrays with the TiO_2 scattering layer, and (c) the open-ended TiO_2 nanotube arrays with the TiO_2 scattering layer treated with $TiCl_4$.

Figure 3. 4. presents the current density−voltage curves of three different DSSCs fabricated using the open-ended TiO_2 nanotube arrays attached to the FTO glass using TiO_2 paste.

Table 3. 2. Photovoltaic properties of DSSCs fabricated using open-ended TiO_2 nanotube arrays

	Jsc (mA/cm^2)	Voc (V)	ff	η (%)
Open-ended TiO_2 nanotube arrays	9.99	0.82	0.73	5.92±0.19
Open-ended TiO_2 nanotube arrays with TiO_2 scattering layer	10.92	0.81	0.74	6.53±0.13
Open-ended TiO_2 nanotube arrays with TiO_2 scattering layer treated with TiCl4	11.63	0.81	0.73	6.89±0.16

The values of Voc, Jsc, ff, and h are summarized in Table 3. 2. For the DSSC fabricated using just the open-ended TiO_2 nanotube arrays, the energy conversion efficiency was 5.92 ± 0.19%. For the DSSC fabricated using the open-ended TiO_2 nanotube arrays with the TiO_2 scattering layer, the energy conversion efficiency was 6.53 ± 0.13%, a 10.30% enhancement. When the open-ended TiO_2 nanotube arrays with the TiO_2 scattering layer were treated with $TiCl_4$, the energy

conversion efficiency improved from 5.92 ± 0.19% to 6.89 ± 0.16%, corresponding to a 16.38% enhancement.

The energy conversion efficiency increased from 5.63 ± 0.14% for the DSSCs with the closed-ended TiO_2 nanotube arrays to 5.92 ± 0.19% for the DSSCs with open-ended TiO_2 nanotube arrays, a 5.15% enhancement. With the introduction of the scattering layer, the efficiency increased from 6.17 ± 0.18% for the DSSCs with the closed-ended TiO_2 nanotube arrays to 6.53 ± 0.13% for the DSSCs with open-ended TiO_2 nanotube arrays, an improvement of 5.83%.

Upon treatment with $TiCl_4$, the enhancement was 5.35%, from 6.54 ± 0.20% for the DSSCs with the closed-ended TiO_2 nanotube arrays to 6.89 ± 0.16% for the DSSCs with open-ended TiO_2 nanotube arrays.

In previous our works, the barrier layer in the closed-ended TiO_2 nanotube arrays affected the electron transport in the DSSCs, so the barrier layer was removed by ion milling in order to prepare the open-ended TiO_2 nanotube arrays [163].

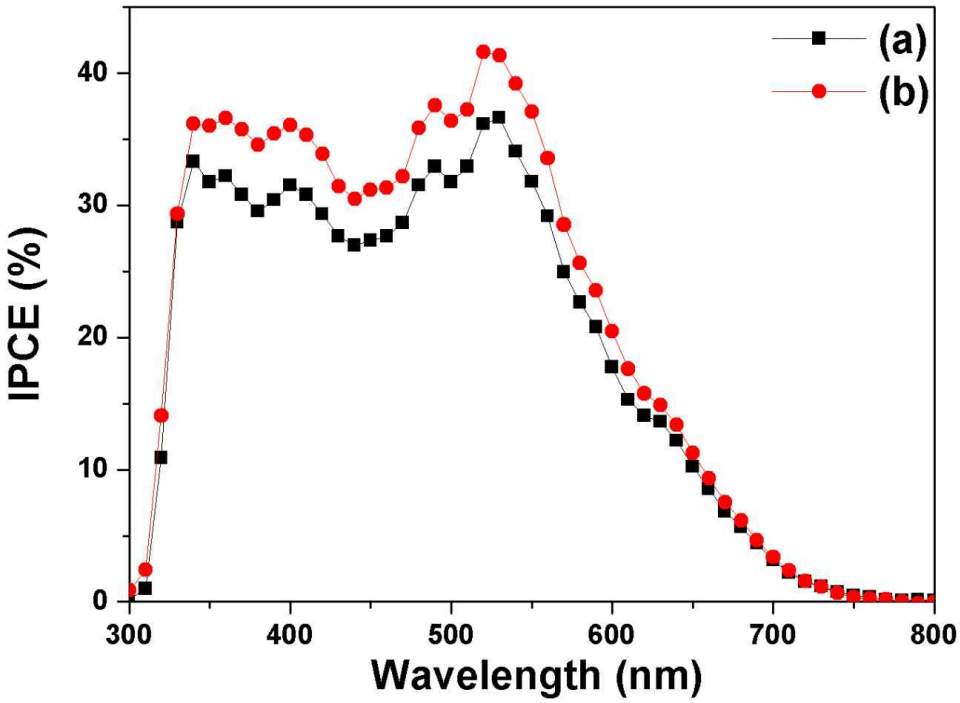

Figure 3. 5. IPCE spectra of DSSCs fabricated using (a) the open-ended TiO_2 nanotube arrays and (b) the open-ended TiO_2 nanotube arrays with the TiO_2 scattering layer.

The IPCE spectra of the DSSCs fabricated using the open-ended TiO_2 nanotube arrays and open-ended TiO_2 nanotube arrays with the TiO_2 scattering layer are shown in Figure 3. 5. The IPCE spectra are similar but the DSSC with the TiO_2 scattering layer had a higher intensity.

3. 4. Conclusions

We prepared dye-sensitized solar cells (DSSCs) with enhanced energy conversion efficiency using open-ended TiO_2 nanotube arrays with a TiO_2 scattering layer.

As compared to closed-ended TiO_2 nanotube arrays, the energy conversion efficiency of the open-ended TiO_2 nanotube arrays was increased from 5.63% to 5.92%, which is an enhancement of 5.15%. Due to the removal of the barrier layer, which was present in the closed-ended TiO_2 nanotube arrays, causing an improvement in electron transport.

By introducing the TiO_2 scattering layer on the open-ended TiO_2 nanotube arrays, the energy conversion efficiency was increased from 5.92% to 6.53%, which is an enhancement of 10.30%.

After treating the open-ended TiO_2 nanotube arrays with $TiCl_4$, the energy conversion efficiency was increased from 5.92% to 6.89%, a 16.38% enhancement, which is attributed to improved light harvesting and increased dye adsorption.

Chapter 4

Ag nanoparticle-functionalized open-ended freestanding TiO_2 nanotube arrays with scattering layer for improved energy conversion efficiency in dye-sensitized solar cells

4. 1. Overall view of Ag nanoparticle-functionalized open-ended freestanding TiO_2 nanotube arrays with scattering layer for improved energy conversion efficiency in dye-sensitized solar cells

Since the original work by O'Regan and Grätzel in 1991 [58], dye-sensitized solar cells (DSSCs) have been investigated extensively because of their high energy conversion efficiency and low cost.[168-175] Generally, mesoporous TiO_2 nanoparticle (NP) films and ruthenium sensitizers are used for DSSCs. [64, 168-181] However, the efficiency of mesoporous TiO_2 NP film-based DSSC is limited by grain boundaries, defects, and numerous trapping sites. Moreover, mesoporous TiO_2 NP films can cause charge recombination and mobility. [82, 182]

TiO_2 nanotubes, which enhance electron transport and charge separation by creating direct pathways and accelerating charge transfer between interfaces, have great potential to overcome the problems of mesoporous TiO_2 NP films. [183-186] TiO_2 nanotubes can be prepared by a hydrothermal method [187] or an electrochemical method [18], known as anodization. TiO_2 nanotube arrays prepared by anodization have a well-ordered and vertically oriented-tubular structure that facilitates a high degree of electron transport and less charge recombination than mesoporous TiO_2 NP films. [38, 149, 164] There is much room for improvement in the energy conversion efficiency of

current DSSCs based on TiO_2 nanotube arrays compared to the relatively extensively researched mesoporous TiO_2 NP film-based DSSCs. [188]

To date, several approaches for improving the energy conversion efficiency of TiO_2 nanotube array-based DSSCs have been reported. Metal NPs, which can harvest light via surface plasmon resonance (SPR), have been used to enhance the energy conversion efficiency of DSSCs by introducing Au or Ag NPs into TiO_2 nanotube arrays. [143, 189-191] Barrier layers remove TiO_2 nanotube arrays, so open-ended TiO_2 nanotube arrays, which can also be classified as arrays of columnar nanopores, have been used for DSSCs to provide increased energy conversion efficiency.[163] Moreover, the energy conversion efficiency of TiO_2 nanotube array-based DSSCs can be further increased by introducing a scattering layer to the active layer.[192]

So far, TiO_2 nanotubes that make use of a scattering layer[192] or plasmonic materials [179] have been reported, but a scattering layer with plasmonic materials has not been used in TiO_2 nanotube-based DSSCs. In this study, we report the development of freestanding TiO_2 nanotube arrays filled with Ag NPs and large TiO_2 NPs, which improve the energy conversion efficiency of DSSCs. Furthermore, we compare the effects of Ag NPs and large TiO_2 NPs in open- and close-ended freestanding TiO_2 nanotube arrays in DSSCs. The energy

conversion efficiencies of the following eight types of DSSC were compared: closed-ended freestanding TiO_2 nanotube arrays with/without Ag NPs and/or TiO_2 scattering layer and open-ended freestanding TiO_2 nanotube arrays with/without Ag NPs and/or a TiO_2 scattering layer.

4. 2. Results and discussion

4. 2. 1 Overall scheme of DSSCs with freestanding TiO_2 nanotube arrays with channels containing Ag NPs

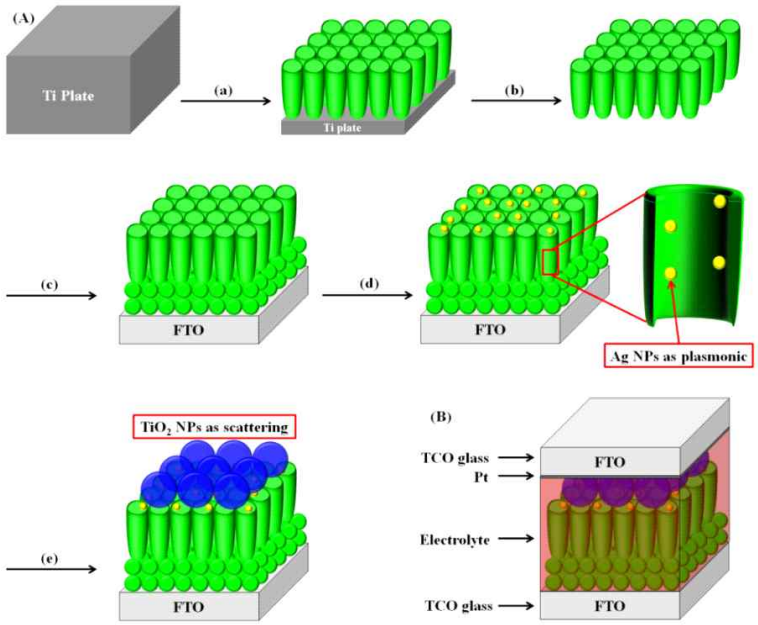

Figure 4. 1. Overall scheme of DSSCs with open-ended freestanding TiO_2 nanotube arrays with Ag NPs and large TiO_2 NPs. (A) (a) Ti anodization for TiO_2 nanotube arrays, (b) freestanding TiO_2 nanotube arrays and etching by ion milling, (c) transference of open-ended freestanding TiO_2 nanotube arrays on FTO glass, (d) formation of Ag NPs by UV irradiation, and (e) introducing large TiO_2 NPs. (B) Structure of DSSC with freestanding TiO_2 nanotube arrays and large TiO_2 NPs.

Figure 4. 1. illustrates the fabrication of DSSCs with Ag NPs and large TiO_2 NPs to enable plasmonic and scattering effect in open-ended freestanding TiO_2 nanotube array-based DSSCs. Ti plates were anodized and then annealed at 500C for 1 h to prepare anatase TiO_2 nanotube arrays. After carrying out secondary anodization, the TiO_2 nanotube arrays were easily detached from the Ti plate. TiO_2 nanotube arrays, once separated from the Ti plate, are termed "closed-ended freestanding TiO_2 nanotube arrays". Freestanding TiO_2 nanotube arrays have a barrier layer at the bottom that disturbs electron transport and electrolyte diffusion.

This barrier layer was removed using the ion-milling method with several minutes of Ar+ bombardment to yield "open-ended freestanding TiO_2 nanotube arrays". The closed- and open-ended freestanding TiO_2 nanotube arrays were transferred to fluorine-doped tin oxide(FTO) glass using TiO_2 paste and annealed to enhance the adhesion between the closed- and open-ended freestanding TiO_2 nanotube arrays and the fluorine-doped tin oxide(FTO) glass.

To improve the energy conversion efficiency by the plasmonic effect, Ag NPs were embedded in the channel of freestanding TiO_2 nanotube arrays using 254 nm ultraviolet(UV) irradiation with aqueous silver nitrate. To further enhance the energy conversion efficiency, large TiO_2 NPs (400 nm) as a scattering layer were coated onto the active layer by the doctor blade method. This substrate was sandwiched with the

counter electrode and filled with electrolyte. The active area of the DSSCs was ~0.25 cm^2.

4. 2. 2 Characterization of freestanding TiO_2 nanotube arrays with channels containing Ag NPs

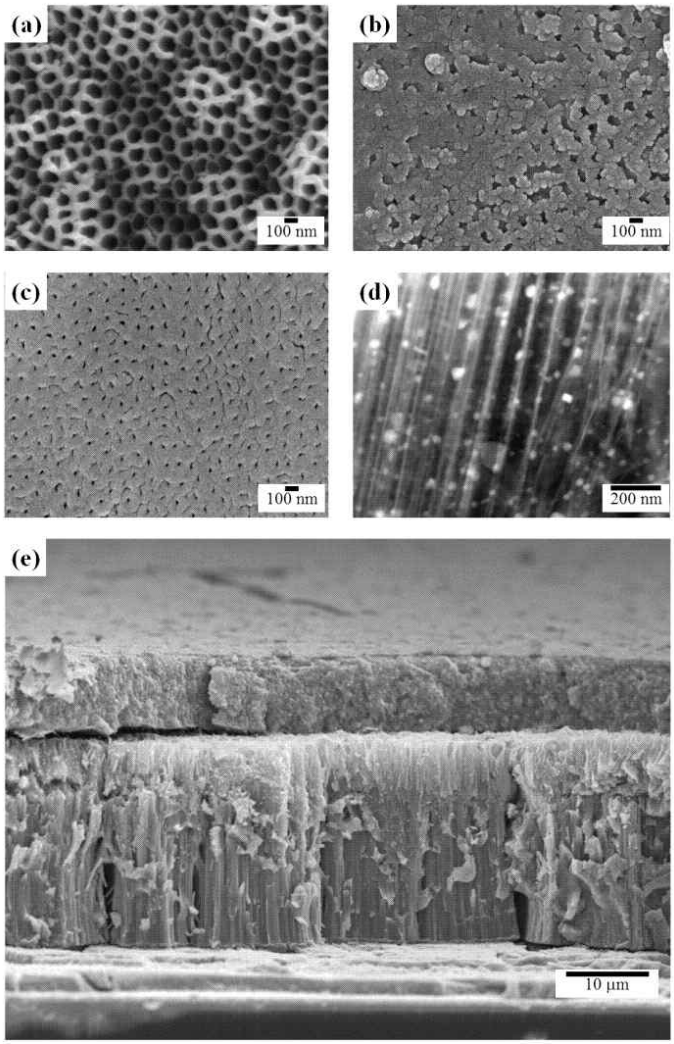

Figure 4. 2. FE-SEM images of the (a) top, (b) bottom, (c) bottom of post-ion milling freestanding TiO_2 nanotube arrays, (d) a high-angle annular dark-field (HAADF) image of Ag NPs in the channel of TiO_2 nanotube arrays, and (e) a side view of the active layer with freestanding TiO_2 nanotube arrays and the scattering layer.

FE-SEM images of freestanding TiO_2 nanotube arrays are shown in Figure 4. 2. The top side of the freestanding TiO_2 nanotube arrays had 100-nm-diameter pores, as shown in Figure 4. 2(a). The bottom layer of closed-ended freestanding TiO_2 nanotube arrays before ion milling lacked pores, as shown in Figure 4. 2(b).

However, after ion milling, 20-nm-diameter pores were evident on the bottom layer of open-ended freestanding TiO_2 nanotube arrays, as shown in Figure 4. 2(c). Open ended TNT arrays can be prepared by the chemical etching [161] and physical etching method. [162, 163] In the chemical etching method, the bottom layer of TNT arrays were easily removed by etchant. However, the surface morphology and length of TNT arrays were also dissolved in etchant and TNT arrays are easily fragile when they are attached on substrate due to their amorphous crystallinity. In the physical etching method, the bottom layer of TNT arrays were removed by the plasma or ion milling process, which is not simple. However, the surface morphology and length of TNT arrays were not damaged and they are very stable when they are attached on substrate because TNT arrays have the annealing process to change the crystallinity from the amorphous to anatase phase. After UV irradiation using a silver source, ~30 nm Ag NP were found in the channels of freestanding TiO_2 nanotubes in high-angle-annular dark-field (HAADF) images, as shown in Figure 4. 2(d). The length of TiO_2 nanotubes was ~22 μm and the length of the

scattering layer, which consisted of 400 nm TiO_2 NPs, was ~10 nm.

The UV-Vis spectrum of Ag NPs in the channels of freestanding TiO_2 nanotubes was shown in Figure 4. 3. A broad absorption peak centered at 402 nm was observed, which indicates the presence of Ag NPs.[193, 194] The absorption band of Ag NPs is matched with dye, N719 has two visible absorption bands; 390 nm 531 nm, [195] that was affected by the plasmon band. Moreover, the shell of Ag NPs was prepared by $TiCl_4$ to prevent the trapping electron by Ag NPs that will be better to electron transport in the channel of TiO_2 nanotube arrays.

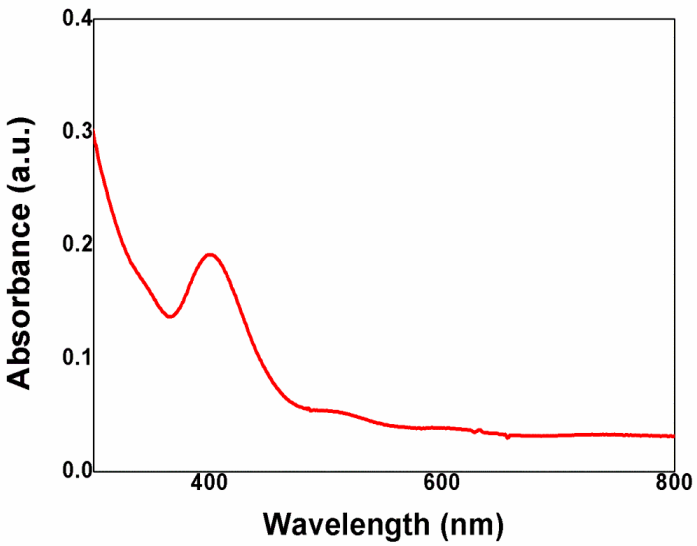

Figure 4. 3. UV-vis spectrum of Ag NP-functionalized TiO_2 nanotubes

4. 2. 3. DSSCs with closed-ended freestanding TiO_2 nanotube arrays with channels containing Ag NPs and large TiO_2 NPs

The photocurrent-voltage curves of DSSCs fabricated using closed-ended freestanding TiO_2 nanotube arrays measured under air mass 1.5 illumination (100 mW/cm^2) are shown in Figure 4. 4. and Table 4. 1.

Four types of closed-ended freestanding TiO_2 nanotube array-based DSSCs were fabricated to assess the effect of each component on the energy conversion efficiency: closed-ended freestanding TiO_2 nanotube array based DSSCs without Ag or large TiO_2 NPs (a), with Ag NPs (b), with large TiO_2 NPs (c), and with Ag NPs and large TiO_2 NPs (d). The open-circuit voltage (Voc), short-circuit current (Jsc), fill factor (ff), and energy conversion efficiency values are shown in Table 4. 1. The energy conversion efficiency of DSSCs based on closed-ended freestanding TiO_2 nanotube arrays lacking NPs was 5.86%. The energy conversion efficiency of the DSSCs based on closed-ended freestanding TiO_2 nanotube arrays with Ag NPs, with large TiO_2 NPs, and with Ag NPs and large TiO_2 NPs was 6.40%, 6.24%, and 6.71%, respectively.

Introduction of Ag NPs increased the energy conversion efficiency significantly, by 9.21% comparing to closed-ended freestanding TiO_2 nanotube array-based DSSCs without Ag and large TiO_2 NPs (actual efficiency; 6.40%), due to increased light harvesting by the plasmonic

effect.

Introduction of large TiO_2 NPs increased the energy conversion efficiency significantly, by 6.48% (actual efficiency; 6.40%), due to increased light harvesting by the scattering effect. Moreover, introduction of both Ag NPs and large TiO_2 NPs increased the energy conversion efficiency significantly, by 14.50% (actual efficiency; 6.71%), due to increased light harvesting by both the plasmonic and scattering effects.

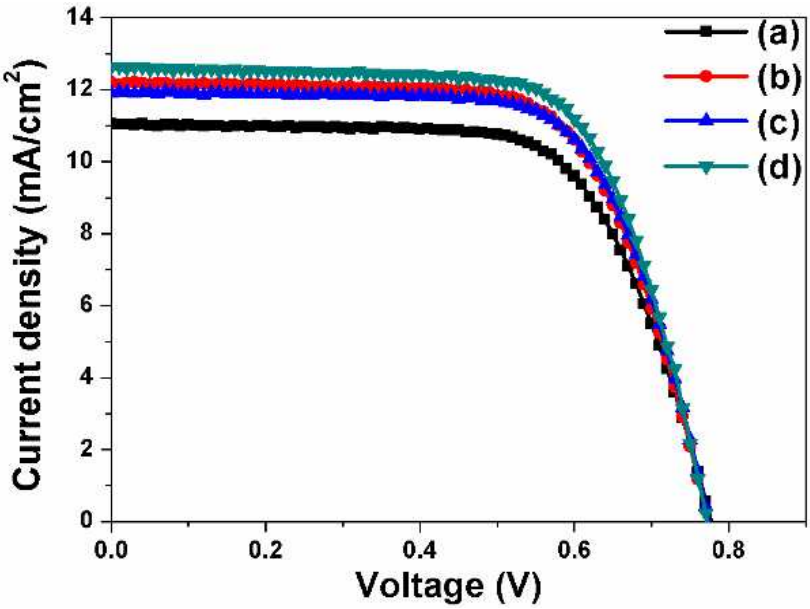

Figure 4. 4. I-V curves of DSSC-based closed-ended freestanding TiO_2 nanotube arrays fabricated without NPs (a), with Ag NPs (b), with large TiO_2 NPs (c), and with Ag NPs and large TiO_2 NPs (d).

Table 4. 1. Photovoltaic properties of DSSCs based on closed-ended freestanding TiO_2 nanotube arrays

	DSSCs	Jsc (mA/cm^2)	Voc (V)	ff	η (%)
a	Closed-ended freestanding TiO_2 nanotube arrays without any NPs	11.05	0.78	0.68	5.86
b	Closed-ended freestanding TiO_2 nanotube arrays with Ag NPs	12.22	0.77	0.68	6.40
c	Closed-ended freestanding TiO_2 nanotube arrays with large TiO_2 NPs	11.90	0.76	0.69	6.24
d	Closed-ended freestanding TiO_2 nanotube arrays with Ag NPs and large TiO_2 NPs	12.63	0.77	0.69	6.71

4. 2. 4. DSSCs with open-ended freestanding TiO_2 nanotube arrays with channels containing Ag NPs and large TiO_2 NPs

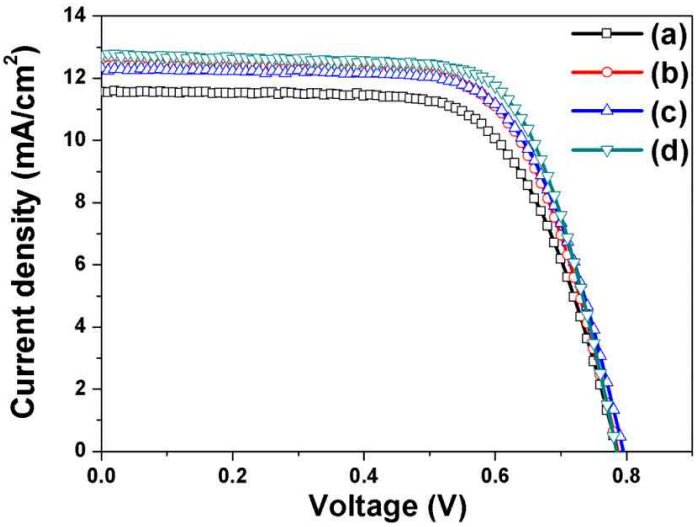

Figure 4. 5. I-V curves of DSSCs based open-ended freestanding TiO_2 nanotube arrays fabricated without NPs (a), with Ag NPs (b), with large TiO_2 NPs (c), and with Ag NPs and large TiO_2 NPs (d).

Table 4. 2. Photovoltaic properties of DSSCs based on open-ended freestanding TiO_2 nanotube arrays

	DSSCs	Jsc (mA/cm^2)	Voc (V)	ff	η (%)
a	Open-ended freestanding TiO_2 nanotube arrays without any NPs	11.56	0.79	0.67	6.12
b	Open-ended freestanding TiO_2 nanotube arrays with Ag NPs	12.45	0.79	0.68	6.68
c	Open-ended freestanding TiO_2 nanotube arrays with large TiO_2 NPs	12.33	0.79	0.68	6.62
d	Open-ended freestanding TiO_2 nanotube arrays with Ag NPs and large TiO_2 NPs	12.74	0.78	0.71	7.05

The photocurrent-voltage curves of DSSCs fabricated using open-ended freestanding TiO_2 nanotube arrays are shown in Figure 4. 5. and Table 4. 2. to assess the effect of each component on the energy conversion efficiency.

Four types of DSSC-based open-ended freestanding TiO_2 nanotube array were fabricated: open-ended freestanding TiO_2 nanotube array based DSSCs without Ag or large TiO_2 NPs, (a), with Ag NPs (b), with large TiO_2 NPs (c), and with Ag NPs and large TiO_2 NPs (d). The Voc, Jsc, ff, and values are summarized in Table 4. 2.

The energy conversion efficiency of DSSCs based on open-ended freestanding TiO_2 nanotube arrays lacking NPs was 6.12%. The energy conversion efficiency of DSSCs based on open-ended freestanding TiO_2 nanotube arrays with Ag NPs, with large TiO_2 NPs, and with Ag NPs and large TiO_2 NPs was 6.68%, 6.62%, and 7.05%, respectively.

The introduction of Ag NPs and/or large TiO_2 NPs increased the energy conversion efficiency by 9.15%, 8.17%, and 15.20%, respectively. Compared to closed-ended freestanding TiO_2 nanotube arrays, the energy conversion efficiency of DSSCs based on open-ended freestanding TiO_2 nanotube arrays was 5.07% (6.71−7.05%) higher due to enhanced electron transport and electrolyte diffusion. [163]

Although TiO_2 nanotube arrays based DSSCs have great potential, as best we know, the theoretical maximum improvement by Ag NPs or TiO_2 scattering layer of TiO_2 nanotube based DSSCs were not reported yet. However, the opened-end TiO_2 nanotube-based device exhibited an increase in one-sun efficiency from 5.3% to 9.1%, corresponding to 70% which is a much higher increase compared to our results. [161] We believe that there is lots of room to improve the efficiency by

combining each parameter with an optimal condition based on theoretical studies.

4. 3. Conclusions

In this study, we compared the natural consequence of several parameters such as the plasmonic effect, the scattering effect and open-closed ended freestanding TiO_2 nanotube as basic experiments for better efficiency.

We demonstrated that the plasmonic and scattering effects enhanced the energy conversion efficiency of freestanding TiO_2 nanotube arrays in DSSCs. Ag NPs were added to the channels of TiO_2 nanotube arrays by UV irradiation to induce a plasmonic effect, and large TiO_2 NPs were introduced to TiO_2 nanotube arrays to induce a scattering effect.

The energy conversion efficiency of DSSCs with both Ag NPs and large TiO_2 NPs was higher than that of DSSCs without Ag NPs due to the plasmonic effect, and was higher than that of DSSCs without large TiO_2 NPs due to the scattering effect. Compared to closed-ended freestanding TiO_2 nanotube arrays, open-ended freestanding TiO_2

nanotube arrays exhibited enhanced energy conversion efficiency.

We demonstrate that Ag NPs, TiO_2 NPs and open-ended freestanding TiO_2 nanotube arrays, enhanced the energy conversion efficiency; furthermore, the combination of all components exhibited the highest energy conversion efficiency. Our research suggests that the energy conversion efficiency of DSSCs is improved by both the plasmonic and scattering effects and have applications in organic solar cells, hybrid solar cells, and perovskite solar cells.

Chapter 5

Dual Functionalized Freestanding TiO_2 Nanotube Arrays Coated with Ag Nanoparticles and Carbon Materials for Dye-Sensitized Solar Cells

5.1. Overall view of dual Functionalized Freestanding TiO_2 Nanotube Arrays Coated with Ag Nanoparticles and Carbon Materials for Dye-Sensitized Solar Cells

Highly ordered, freestanding TiO_2 nanotube arrays (TiO_2 NTAs) were prepared using an electrochemical method. The barrier layer was etched to open the bottom of each array, aptly named "open-ended TiO_2 NTAs". These arrays were coated with silver nanoparticles (Ag NPs) and/or carbon materials to enhance electron generation and transport. The energy conversion efficiency of the resulting dye-sensitized solar cells (DSSCs) with open-ended freestanding TiO_2 NTAs increased from 5.32% to 6.14% (by 15%) when coated with Ag NPs due to plasmonic interactions. Meanwhile, coating the open-ended freestanding TiO_2 NTAs with carbon materials increased the energy conversion efficiency from 5.32% to 6.07% (by 14%) due to π-π conjugation. When the Ag NPs and carbon materials were simultaneously applied to the open-ended freestanding TiO_2 NTAs, the energy conversion efficiency increased to 6.91% an enhancement of 30% due to the additive effects of plasmonics and π-π conjugation.

Global research of dye-sensitized solar cells (DSSCs) has continued since their initial development in 1991 by the Grätzel group [58], due to their low cost, ease of fabrication, and high power conversion efficiency [64,197]. Titanium dioxide nanoparticles (TiO_2 NPs) are

typically used as the photoanode in DSSCs, because they have a desirable direct band gap (3.2 eV) and a large surface area for adsorbing dyes, both helping to generate electrons [198-201]. However, TiO_2 NPs are randomly networked, and the countless grain boundaries within them lead to material defects and charge recombinations that inhibit the smooth electron transport [62,202,203].

For the last few years, TiO_2 nanotube arrays (NTAs) have been explored as an alternative to TiO_2 NPs [204-206]. The TiO_2 NTAs could be fabricated using an electrochemical method (i.e., anodization) [204,207], and they have a well-ordered and vertically aligned tubular structure that serves as direct electron pathways to enhance not only electron transport, but also charge separation [208,209]. Despite their merits, however, the barrier layer at the bottom of the TiO_2 NTAs could impede charge transfer and electrolyte diffusion. To overcome this problem, we recently removed the bottom layer of TiO_2 NTAs using argon ion (Ar^+) milling, resulting in improved electron transport and electrolyte diffusion [210].

There have been an increasing number of studies that add carbon to TiO_2 NTAs in order to improve the charge separation and transfer of electrons, due to the superior electrical properties of the π-π conjugation [211-213]. Many researchers have explored the application of carbon materials in solar cell technologies. Carbon 60 (C60 or "fullerene") and carbon nanotubes (CNTs) are well known for their

roles as electron acceptors and charge separators in organic solar cells [214,215]. When incorporated in organic solar cells, CNTs act as exciton dissociation sites and hopping centers for hole transport [216], and graphene mixed with TiO_2 NPs in DSSCs plays a role in promoting charge separation and movement [217]. As mentioned, TiO_2 NTAs were developed as alternatives to TiO_2 NPs. While it is not simple to blend carbon materials with TiO_2 NTAs, we recently reported a method for enriching freestanding TiO_2 NTAs with carbon for use in DSSCs. When a small amount of carbon was deposited on TiO_2 NTAs, the energy conversion efficiency increased by approximately 22.4% compared to those without carbon enrichment [218]. We tentatively attributed this to the π-π conjugation introduced by carbon enrichment that improved the efficiency of electron transport.

A plasmonic effect triggered by metal NPs such as silver and gold can be used to enhance photoabsorption in solar cells [219-221]. When incident photons pass by Ag NPs, they cause electron vibration and photo scattering of the nanoparticles, which facilitate more efficient photon control [222]. The metal NPs were incorporated by mixing with TiO_2 sol in the DSSCs or with precursors of the active layer in organic solar cells. In the fabrication of DSSCs based on TiO_2 NTAs, however, it is difficult to insert metal NPs into the channels of TiO_2 NTAs. We recently devised a simple method for the complete formation of Ag NPs in the channels of TiO_2 NTAs using UV

irradiation [223-225]. These NPs helped the dyes generate electrons, as demonstrated by a high current density in the DSSCs.

To date, we have confirmed the separate effects of carbon enrichment and the incorporation of Ag NPs in previous studies. However, the effects of adding both carbon and Ag NPs remain unknown. Here, we report the effects of enriching freestanding TiO_2 NTAs with one or both materials on the performance of DSSCs, in terms of enhanced electron transport and plasmonic effects. Carbon materials were synthesized by chemical vapor deposition (CVD) and deposited on the wall of TiO_2 NTAs. The Ag NPs were formed using UV irradiation within the channels of TiO_2 NTAs.

5.2. Materials and Methods

5.2.1 Preparation of closed- and open-ended TiO_2 NTAs

Titanium foils (Alfa Aesar, 99.7% purity, 2.5 cm × 4.0 cm × 320 μm) were prepared and anodized using an electrochemical method to fabricate TiO_2 NTAs. The electrolyte was composed of 0.8 wt.% NH_4F and 2 vol.% H_2O in ethylene glycol. Carbon rods served as the cathode material. A 60 V DC potential was supplied to the titanium foils at 25 °C for 2 h. Later, the anodized titanium foils were annealed in a tube furnace at 450 °C for 1 h, and a second anodization process was then conducted on the samples at 30 V for 10 min. To detach the TiO_2 NTAs from the titanium foils, the sample after the second anodization was immersed in 10% H_2O_2 for 24 h. Ion milling with argon (Ar^+) bombardment was used to remove the bottom of the TiO_2 NTAs to make open-ended tips [218].

5.2.2 Preparation of photoanodes for DSSCs based on the TiO_2 NTAs

Fluorine-doped tin oxide (FTO) glass was washed and sonicated in ethanol and acetone to remove impurities. Titanium diisopropoxide bis(acetylacetonate) (5 wt.% in n-butanol) was spin-coated on the clean FTO glass to form a compact TiO_2 blocking layer after annealing at

450 °C for 1 h. A TiO_2 paste (Solaronix, T/SP) was applied to the FTO glass using a doctor blade method, in order to attach the closed- or open-ended TiO_2 NTAs. Finally, the samples were annealed in a furnace at 450 °C for 30 min.

5.2.3 Synthesis of Ag NPs on the TiO_2 NTAs by UV irradiation

The samples were placed in a 0.3 mM $AgNO_3$ aqueous solution. Ag NPs were synthesized in the channels of closed- or open-ended TiO_2 NTAs using a 254 nm UV lamp for 3 min.

5.2.4 Synthesis of carbon materials by CVD on TiO_2 NTAs

The samples were placed in a quartz tube furnace filled with nitrogen (200 standard cubic centimeter per minute [sccm]). Hydrogen gas (30 sccm) and ethylene gas (40 sccm) were flowed into the tube furnace at 450 °C for 30 s.

5.2.5 Fabrication of dye-sensitized solar cells

All DSSC samples were post-treated with 10 mM $TiCl_4$ solution at 50 °C for 30 min, and then annealed at 450 °C for 1 h. These steps not only enhanced the photocurrent but also prevented the Ag NPs from dissolution upon contacting the iodine-iodide electrolyte. Each

treated sample was stained using dye molecules (0.5 mM solutions of N719 ($(Bu_4N)_2Ru(dobpyH)_2(NCS)_2$, Solaronix) in ethanol at 50 °C for 8 h. Following this treatment, samples were washed with ethanol to eliminate physisorbed dye molecules. To fabricate counter electrodes, chloroplatinic acid (H_2PtCl_6) in ethanol was drop-casted onto clean FTO glass and annealed in a tube furnace at 400 °C for 1 h.

The electrolyte used to separate the electrodes contained 0.7 M 1-butyl-3-methyl-imidazolium iodide (BMII), 0.03 M I_2, 0.1 M guanidium thiocyanate (GSCN), and 0.5 M 4-tert-butyl pyridine (TBP) in a mixture of acetonitrile and valeronitrile (85:15 v/v). A 60-μm thick hot-melt Surlyn spacer (Solaronix) was put between the photoanode and counter electrode. The electrolyte was injected into the space provided by the Surlyn spacer.

5.2.6 Characterization of dye-sensitized solar cells

The structures of TiO_2 NTAs on FTO glass were confirmed using a field emission scanning electron microscope (FE-SEM, JSM-6330F, JEOL Inc.). The existence of Ag NPs in the channels of TiO_2 NTAs was verified by the high-angle annular dark-field (HAADF) imaging technique using a scanning transmission electron microscope (TEM, JEM-2200FS, JEOL Inc.). Raman spectra were measured with a Raman spectrometer (LabRAM HV Evolution spectrometer, HORIBA). The

UV-Vis spectra were recorded using a UV-Vis spectrophotometer (NEOSYS-2000, SCINCO). Current density-voltage measurements were carried out using an electrometer (Keithley 2400) and a solar simulator (1 kW xenon with AM 1.5 filter, PEC-L01, Peccel Technologies). Electrochemical impedance spectroscopy (EIS) data were collected using a potentiostat (Solartron 1287) equipped with a frequency response analyzer (Solartron 1260) between 10^{-2} and 10^{6} Hz under AM 1.5 light illumination, and analyzed using Z-View software (Solartron Analytical). The applied bias voltage and AC amplitude were set at the open circuit voltage (Voc) of the DSSCs and 10 mV, respectively.

5.3. Results and Discussion

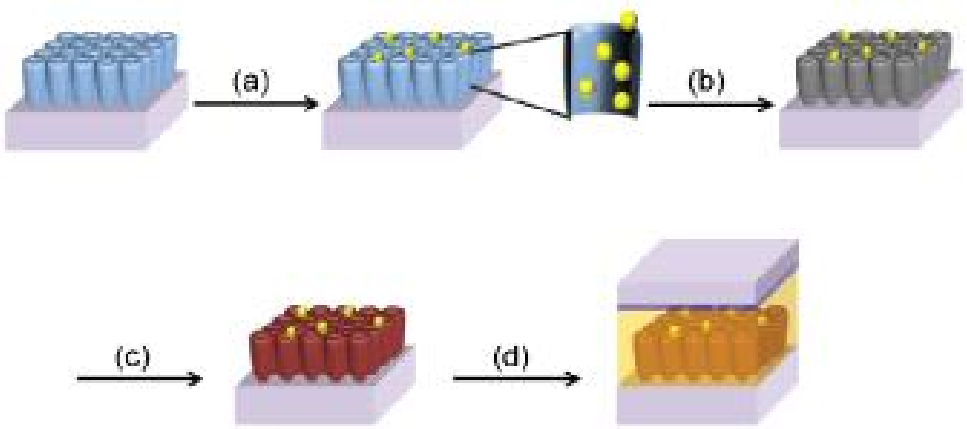

Figure 5.1. Overall scheme of the fabrication of DSSCs based on freestanding TiO_2 NTAs coated with Ag NPs and carbon materials. (a) Synthesis of Ag NPs in the channel of TiO_2 NTAs, (b) deposition of carbon materials, (c) dye adsorption, and (d) fabrication of the DSSC.

The fabrication of DSSCs based on freestanding TiO_2 NTAs is shown in Figure 5.1. The bottom layer was present in the closed-ended freestanding TiO_2 NTAs, but removed by ion milling in the open-ended ones. The DSSCs were fabricated from both types of freestanding TiO_2 NTAs to compare their energy conversion efficiency. In both cases, the freestanding TiO_2 NTAs were attached to the FTO glass with TiO_2 paste, and Ag NPs were synthesized using UV irradiation as shown in Figure 5.1(a). Carbon materials were synthesized using CVD as shown in Figure 5.1(b). By using the UV irradiation and CVD, Ag NPs and

carbon materials were deposited in the channel of highly ordered TiO_2 NTAs without any distortion. The dye (N719) was adsorbed onto both types of freestanding TiO_2 NTAs, as shown in Figure 5.1(c). Finally, DSSCs were fabricated by assembling the working electrode (freestanding TiO_2 NTAs on FTO glass) and the counter electrode (Pt on FTO glass) as shown in Figure 5.1(d).

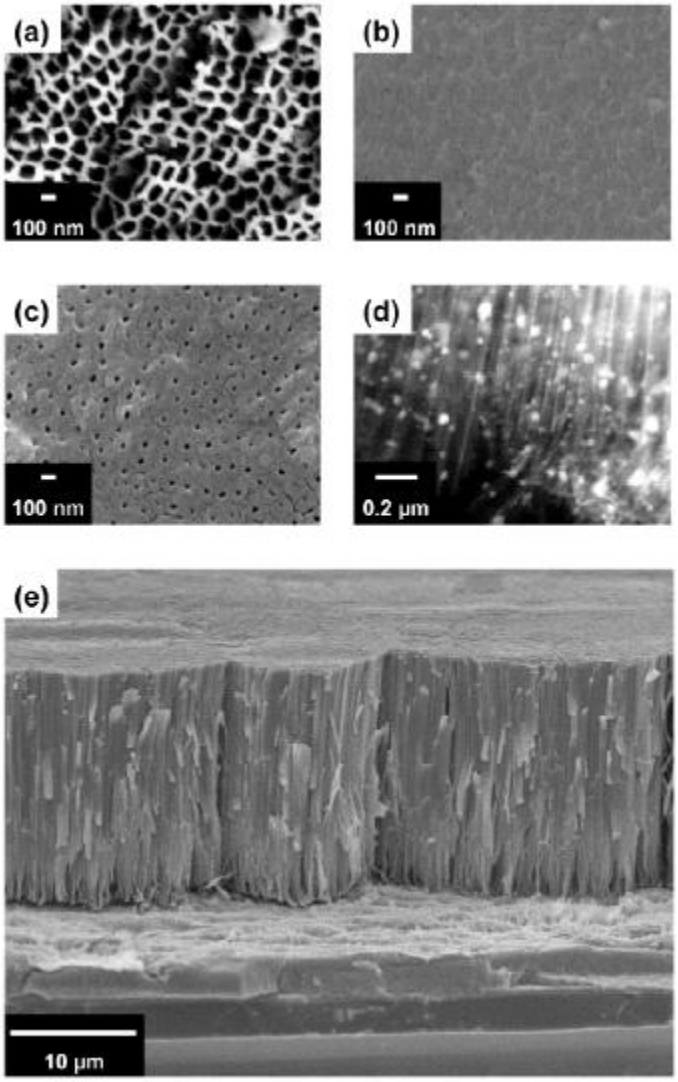

Figure 5.2. FE-SEM images of TiO_2 NTAs: (a) top view, (b) bottom view, and (c) bottom view after ion milling. (d) HAADF image of Ag NPs in the channel of TiO_2 NTAs. (e) Side view of TiO_2 NTAs on FTO glass.

FE-SEM images of TiO_2 NTAs are shown in Figure 5.2. The top view in Figure 5.2(a) shows a pore size of approximately 100 nm after applying the electrochemical method. The bottom of the TiO_2 NTAs before ion milling (the "closed-ended TiO_2 NTA") is shown in Figure 5.2(b), with a total bottom pore size of approximately 100 nm including that of the wall thickness. However, when the bottom was removed by ion milling to produce the "open-ended TiO_2 NTAs" (Figure 5.2(c)), the bottom pore was reduced to 30 nm in size, and the wall thickness was approximately 35 nm. An HAADF image of Ag NPs in the channels of TiO_2 NTAs is shown in Figure 5.2(d), and the diameter of Ag NPs was approximately 30 nm. This allowed the Ag NPs to be successfully immobilized inside the channel of TiO_2 NTAs by UV irradiation, and the resulting plasmonic interactions may have affected all the surface areas. A side view of TiO_2 NTAs attached to the FTO glass by TiO_2 paste after being sintered at 450 °C is shown in Figure 5.2(e). The main role of the TiO_2 paste is to connect the TiO_2 NTAs with the FTO glass surface. The thickness of the TiO_2 film layer was 3 μm, and the length of TiO_2 NTAs was approximately 18 μm.

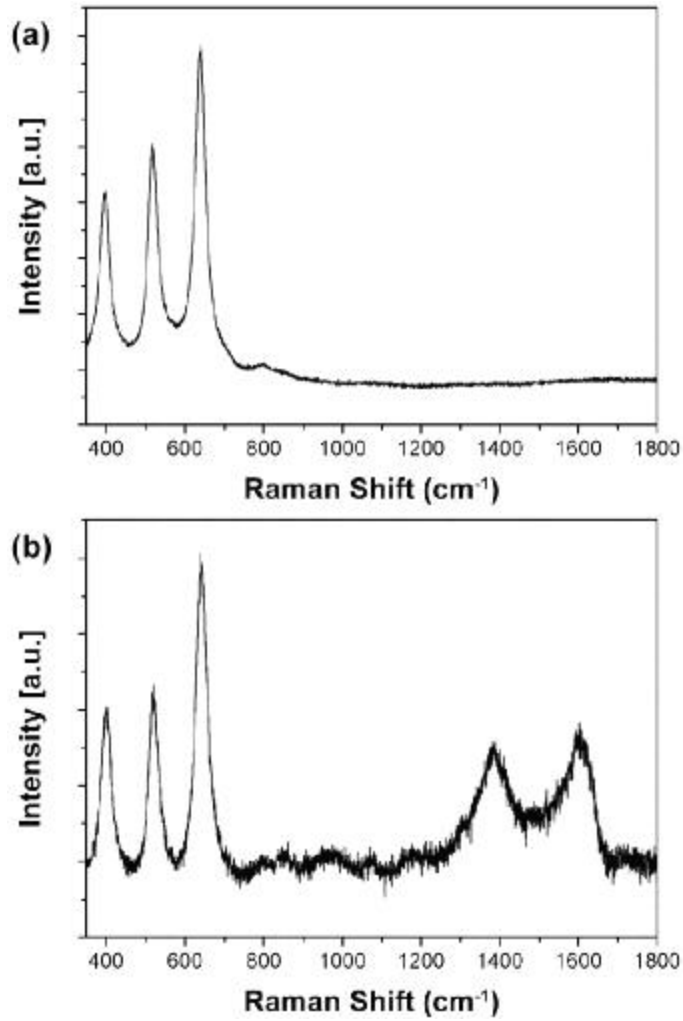

Figure 5.3. Raman spectra of TiO_2 NTAs (a) without and (b) with carbon materials.

Carbon materials on the TiO_2 NTAs were synthesized by CVD, and their structure was confirmed by Raman spectroscopy, as shown in Figure 5.3. In a previous publication, we reported the optimization of

TiO_2 NTAs for DSSCs using carbon materials [218]. The B1g (397 cm^{-1}), A1g (518 cm^{-1}), and Eg (641 cm^{-1}) peaks indicated that the TiO_2 NTAs were in the form of anatase TiO_2, as shown in Figure 5.3(a) [225]. When carbon materials were synthesized on the TiO_2 NTAs using CVD, the G band at 1600 cm^{-1} represented graphite, while the D band at 1384 cm^{-1} was due to the disorderly network of sp^2 and sp^3 sites in the carbon materials, as shown in Figure 5.3(b). The sp^2 sites of carbon materials resulted in a π-π conjugation that improved the efficiency of electron transport across the TiO_2 NTAs.

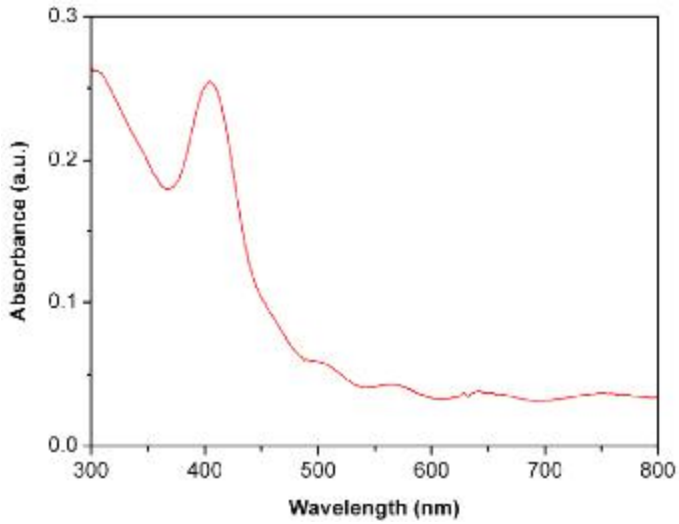

Figure 5.4. UV-Vis spectrum of Ag NPs on the TiO_2 NTAs.

Ag NPs were synthesized on the TiO_2 NTAs using UV irradiation, and this was confirmed by the ultraviolet-visible (UV-Vis) spectrum. The size of Ag NPs was confirmed as approximately 30 nm, using the HAADF image shown in Figure 5.2(d). An absorption peak centered at 405 nm was observed, as shown in Figure 5.4. Our previous paper [218] reported on the optimization of TiO_2 NTAs using Ag NPs. Other researchers have reported that Ag NPs with sizes of approximately 30 nm had UV-Vis absorption peaks at 420 nm. However, in this case, the Ag NPs were synthesized using UV irradiation (at 254 nm) without the addition of any stabilizing or reducing agents. As such, the Ag NPs were immobilized in the TiO_2 NTAs, which would affect absorption in the UV-Vis spectrum. The absorption band of Ag NPs is within the same range as that of the dye N719 (cis-diisothiocyanato-bis (2,2'-bityridyl-4,4'-dicarboxylato) ruthenium(II) bis(tetrabutylammonium), 390−530 nm, leading to enhanced electron generation from the dye by means of plasmonic interactions.

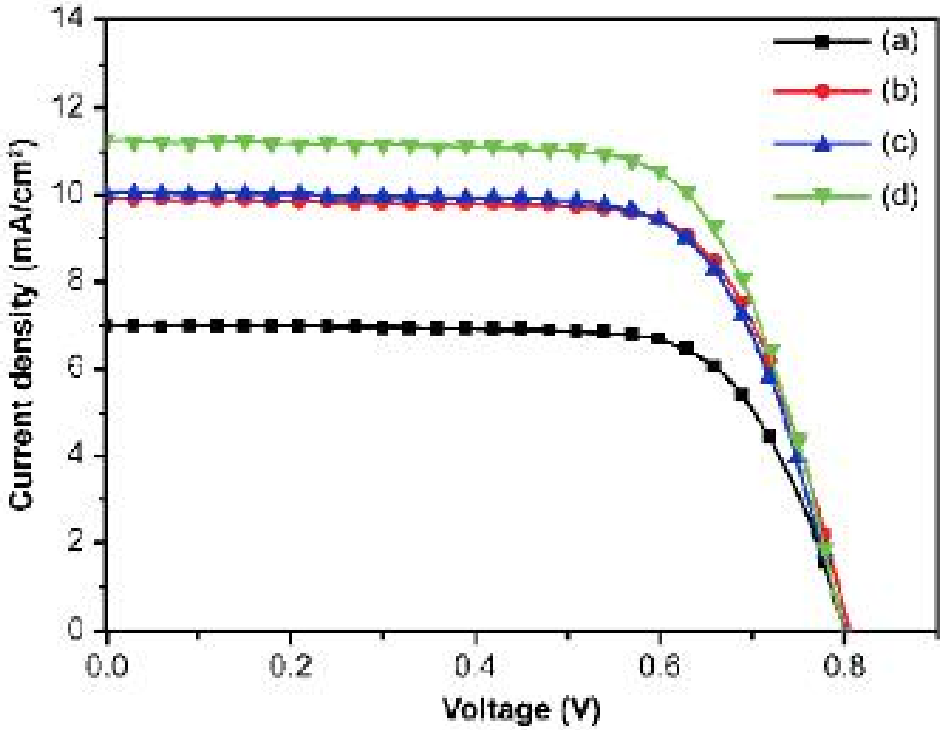

Figure 5.5. Current density-voltage curves of DSSCs based on (a) unmodified closed-ended TiO_2 NTAs, (b) with embedded Ag NPs, (c) with applied carbon materials, and (d) with both Ag NPs and carbon materials.

The current density-voltage curves of DSSCs using closed-ended TiO_2 NTAs with or without modification were measured under air-mass (AM) 1.5 sunlight, and the results are presented in Figure 5.5. The Voc, short-circuit current density (Jsc), fill factor (ff), and energy conversion efficiency (η) of the DSSCs are summarized in Table 5.1. For the DSSCs without any treatment, the energy conversion efficiency

was 4.10%, which increased to 5.73% when Ag NPs were embedded via UV irradiation, corresponding to an overall increase of 40%. When carbon materials were added to the closed-ended TiO_2 NTAs via CVD, the energy conversion efficiency improved to 5.69%, corresponding to a 39% increase. With both Ag NPs and carbon materials, the energy conversion efficiency improved even further to 6.36%, corresponding to an overall increase of 55%. Note that when Ag NPs were treated with $TiCl_4$, the core-shell type $Ag@TiO_2$ nanoparticles were formed. Because the dye are adsorbed on $Ag@TiO_2$, the amount of dye loading might not be significantly reduced as shown table 5.1. As previously reported [218], a large amount of carbon doping materials could lower the conversion efficiency by decreasing of dye loading. However, in this case only a trace amount of carbon material was deposited, which did not decrease the dye loading significantly.

Table 5.1. Photovoltaic properties of DSSCs based on closed-ended TiO_2 NTAs with Ag NPs and/or carbon materials.

DSSCs based on closed-ended TiO_2 NTAs decorated	J_{sc} (mA/cm^2)	Voc (V)	*ff*	η (%)	Dye loading ($nmol/cm^2$)
without Ag NPs and carbon materials	7.02	0.81	0.72	4.10 ±0.28	144
with Ag NPs	9.92	0.81	0.72	5.73 ±0.31	142
with carbon materials	10.03	0.80	0.71	5.69 ±0.26	139
with Ag NPs and carbon materials	11.25	0.80	0.71	6.36 ±0.34	141

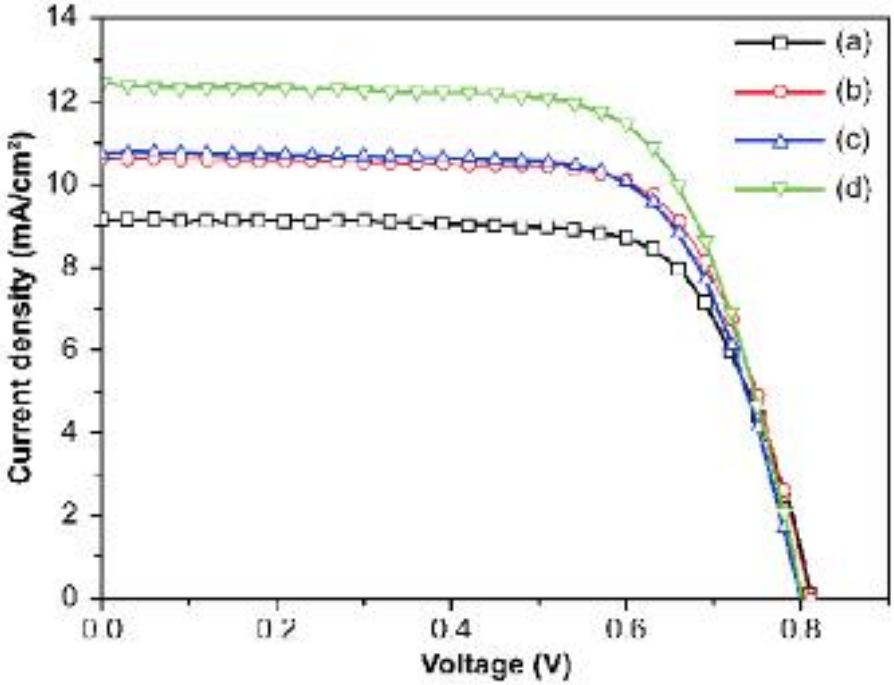

Figure 5.6. Current density-voltage curves of DSSCs based on (a) unmodified open-ended TiO_2 NTAs, (b) embedded with Ag NPs, (c) applied with carbon materials, and (d) with both Ag NPs and carbon materials.

Table 5.2. Photovoltaic properties of DSSCs based on open-ended TiO2 NTAs with Ag NPs and/or carbon materials.

DSSCs based on open-ended TiO_2 NTAs decorated	J_{sc} (mA/cm^2)	Voc (V)	*ff*	η (%)	Dye loading ($nmol/cm^2$)
without Ag NPs and carbon materials	9.12	0.81	0.72	5.32 ±0.36	153
with Ag NPs	10.61	0.81	0.71	6.14 ±0.46	151
with carbon materials	10.73	0.80	0.71	6.07 ±0.30	147
with Ag NPs and carbon materials	12.41	0.80	0.69	6.91 ±0.41	149

The current density-voltage curves for DSSCs based on open-ended TiO_2 NTAs with or without modification were also measured under AM 1.5 sunlight, and the results are presented in Figure 5.6. The Voc, Jsc, ff, values of these DSSCs are summarized in Table 5.2. When using unmodified TiO_2 NTAs, DSSCs based on open-ended TiO_2 NTAs had higher energy conversion efficiency (5.32%) compare to those based on closed-ended ones (4.10%). The closed-end barrier of the TiO_2 NTA disturbs electron transport between the TiO_2 layer and the electrode [210,218].

When Ag NPs were embedded in the open-ended TiO_2 NTAs, the energy conversion efficiency improved from 5.32% to 6.14%, corresponding to a 15% enhancement. In this case, electron generation in the DSSCs was enhanced by the plasmonics from the NPs, despite the slightly diminished dye loading (from 153 to 151 nmol/cm^2). When carbon materials alone were applied to TiO_2 NTAs, the energy conversion efficiency improved to 6.07%, a 14% increase. In this case, the carbon materials improved electron transport due to the π-π conjugation across the small quantity of carbon materials, in spite of a diminished dye load (153 to 147 nmol/cm^2, which is even less than that with Ag NPs). The reason is that the carbon materials were distributed to interact between the TiO_2 and the dye, making up for the loss of dye loading in term of the energy conversion efficiency. When Ag NPs and carbon materials were both applied to the open-ended TiO_2 NTAs, the energy conversion efficiency improved to 6.91%, corresponding to a 30% enhancement compared to the unmodified open-ended TiO_2 NTAs. In this case, the Ag NPs and carbon materials produced additive effects with their respective plasmonics and π-π conjugations, in spite of a slightly reduced dye loading of 149 nmol/cm^2. Comparing the performance parameters in Table 5.2, the Voc and ff decreased with treatment; the conduction band of the TiO_2 NTAs shifted down, which in turn affected the Voc and the charge recombination through electron density that suppressed

the ff. However, the Jsc was increased by the plasmonic activity in conjunction with π-π conjugation, which improved the energy conversion efficiency of DSSCs.

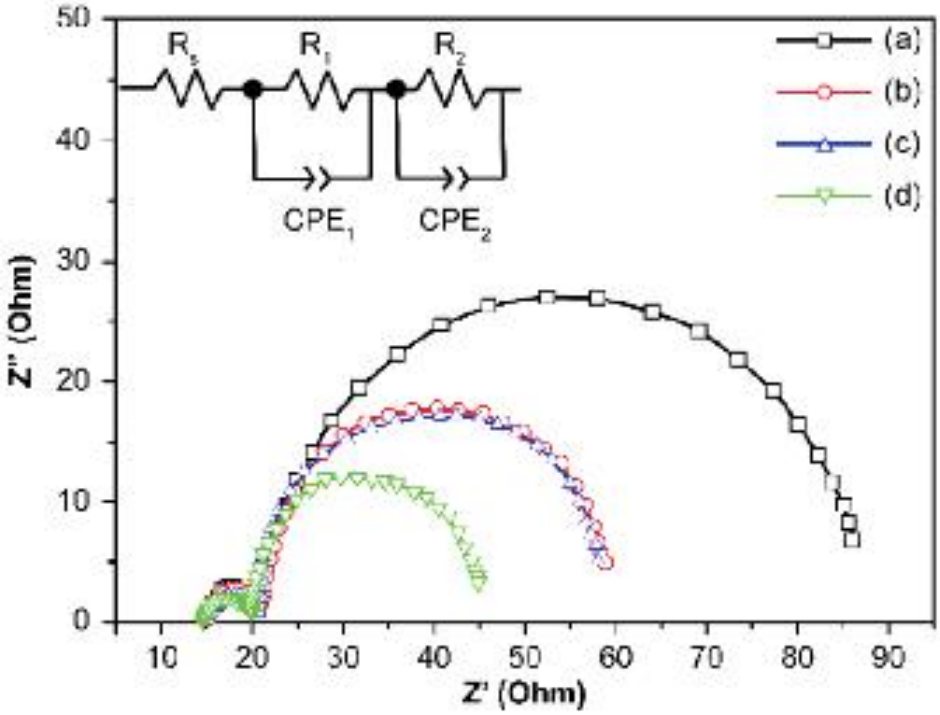

Figure 5.7. EIS data of DSSCs based on (a) unmodified open-ended TiO_2 NTAs, (b) embedded with Ag NPs, (c) applied with carbon materials, and (d) with both Ag NPs and carbon materials.

Table 5.3. EIS fitting results for DSSCs with open-ended TiO_2 NTAs.

DSSCs based on open- ended TiO_2 NTAsdecorated	R_s (Ω)	R_1 (Ω)	CPE_1 (F)	R_2 (Ω)	CPE_2 (F)
without Ag NPs and carbon materials	15.50	5.58	6.91×10^{-6}	61.12	1.99×10^{-3}
with Ag NPs	15.52	5.54	8.65×10^{-6}	36.90	2.10×10^{-3}
with carbon materials	15.56	5.07	1.62×10^{-5}	36.40	2.03×10^{-3}
with Ag NPs and carbon materials	14.99	4.88	1.16×10^{-6}	24.55	2.99×10^{-3}

The DSSCs based on open-ended TiO_2 NTAs were characterized by EIS across the frequency range from 10^{-2} to 10^{6} Hz, as shown in Figure 5.7. The applied bias voltage was set at the Voc with 10 mV of AC amplitude. The data were analyzed using an equivalent circuit (inset of Figure 5.7), and the fit parameters are listed in Table 5.3. The ohmic series resistance (R_s) is due to the sheet resistance that corresponds to the x-axis value where the first semicircle begins on the left-hand side in Figure 5.7. The value of Rs is similar with or without Ag NPs or carbon materials, meaning that the additional deposits did not affect the sheet's resistance to FTO or the current collector. The R_1 value is given by the sum of the small semicircle at

high frequency that is assigned to the parallel combination of resistances, and the capacitances at the Pt-FTO/electrolyte and the FTO/TiO_2 interfaces. The R_2 value is given by the sum of the large semicircle at low frequency that is associated with the resistance, and the capacitance at the dye-adsorbed TiO_2/electrolyte interface, plus the transport resistance. The value of R_1 without and with Ag NPs was approximately 5.58 and 5.54 Ω, respectively. However, the value of R_2 with Ag NPs (36.90 Ω) is much lower than that without Ag NPs (61.12 Ω). More electrons were generated by plasmonic activities than produced at the dye-adsorbed TiO_2/electrolyte interface. As a result, the R_2 value was reduced in the presence of Ag NPs. The value of R_1 with carbon materials (5.07 Ω) was less than those without or with Ag NPs (5.58 and 5.54 Ω, respectively), whereas the value of R_2 (36.40 Ω) was less than that without Ag NPs (61.12 Ω). Electrons are better transported by π-π conjugation that is affected by the FTO/TiO_2 and dye-adsorbed TiO_2/electrolyte interfaces. Hence, the values of both R_1 and R_2 decreased in the presence of carbon materials. In the presence of both Ag NPs and carbon materials, the values of R_1 (4.88 Ω) and R_2 (24.55 Ω) were the lowest. More electrons were generated and better transported in this case, by a combination of plasmonics and the π-π conjugation that affected the FTO/TiO_2 and dye-adsorbed TiO_2/electrolyte interfaces. Therefore, the values of R_1 and R_2 were reduced.

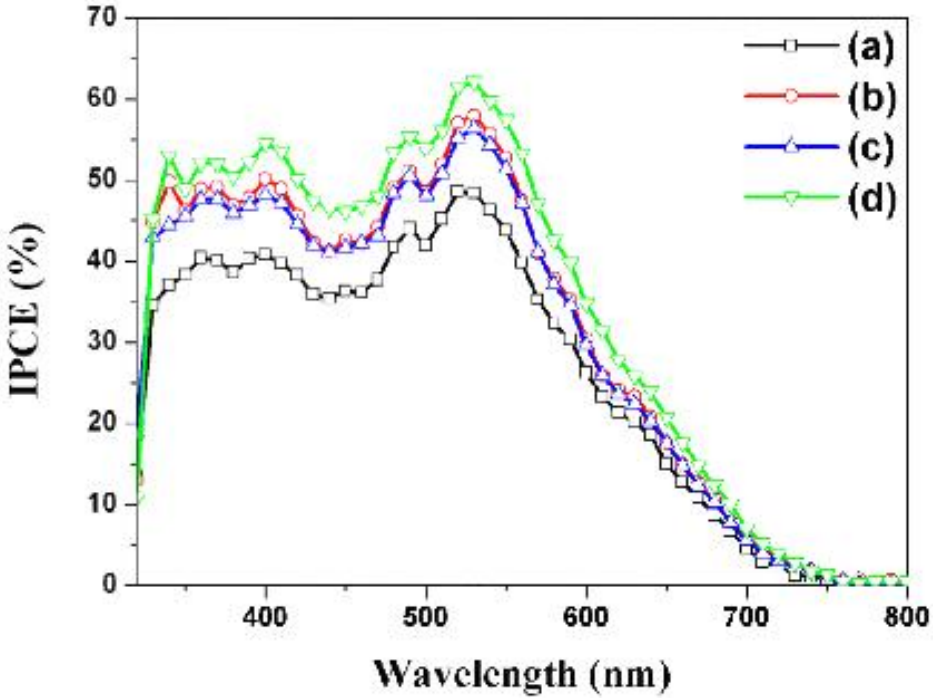

Figure 5.8. IPCE of DSSCs based on (a) unmodified open-ended TiO_2 NTAs, (b) embedded with Ag NPs, (c) applied with carbon materials, and (d) with both Ag NPs and carbon materials.

The incident photon-to-electron conversion efficiency (IPCE) of DSSCs based on the open-ended TiO_2 NTAs is shown in Figure 5.8. Plasmon is a kind of quasiparticle consisting of free electrons collectively vibrating within the metal. At the interface between a metal with negative dielectric constant and a medium having positive dielectric constant, surface plasmon resonance (SPR) combines a spreading electromagnetic wave on this interface (from visible to near-infrared

frequency) and the plasmon. This combination generates plasmon-polariton, which leads to optical absorption, and strong electric field is generated in some parts. During SPR, the light energy accumulates on the metal nanoparticle surface, and optical control is possible in the frequency range below the optical diffraction limit. Therefore, the intensity of DSSC based on open-ended TiO_2 NTAs embedded with Ag NPs is higher than that without. This may mean that more electrons were generated by the plasmonic activities, which increased the short circuit current. The current intensity in the DSSCs based on open-ended TiO_2 NTAs with carbon materials is also higher than that without. This may mean that electrons were better transported by π-π conjugation, which also increased the short circuit current. Moreover, the current intensity is the strongest in the presence of both Ag NPs and carbon materials. In this case, electrons are generated in large quantities and are better transported by plasmonic activities and π-π conjugation.

4. Conclusions

We deposited Ag NPs and carbon materials in the channels of closed- and open-ended TiO_2 NTAs using UV irradiation and CVD, respectively. These modifications improved the energy conversion efficiency of the corresponding DSSCs: the electron generation is enhanced by plasmonics from the Ag NPs, while the resistance of TiO_2 NTAs is suppressed via the π-π conjugation from the carbon materials. DSSCs made of freestanding TiO_2 NTAs coated with both Ag NPs and carbon materials had the best energy conversion efficiency, due to the combination of these two factors. Between the open-ended and closed-ended TiO_2 NTAs (both with Ag NPs and carbon materials), the energy conversion efficiency of the DSSCs was higher for the former.

References

1. Jason A. C. , Wood J. L. : Some electrical effects of the adsorption of water vapour by anodized aluminum. Proceedings of the Physical Society of London Section B 1955, 68(12):1105-1116.
2. Nakao M., Oku S., Tamamura T., Yasui K., Masuda H.: GaAs and InP nanohole arrays fabricated by reactive beam etching using highly ordered alumina membranes. Japanese Journal of Applied Physics Part 1-Regular Papers Short Notes & Review Papers 1999, 38(2B):1052-1055.
3. Li J., Papadopoulos C., Xu J. M., Moskovits M.: Highly-ordered carbon nanotube arrays for electronics applications. Applied Physics Letters 1999, 75(3):367-369.
4. Li J, Papadopoulos C, Xu J: Nanoelectronics - Growing Y-junction carbon nanotubes. Nature 1999, 402(6759):253-254.
5. Chen L, Yin A. J., Im J. S., Nurmikko A. V., Xu J. M., Han J.: Fabrication of 50-100 nm patterned InGaN blue light emitting heterostructures. Physica Status Solidi a-Applied Research 2001, 188(1):135-138.
6. Hu W. C., Gong D. W., Chen Z., Yuan L. M., Saito K., Grimes

C. A., Kichambare P.: Growth of well-aligned carbon nanotube arrays on silicon substrates using porous alumina film as a nanotemplate. Applied Physics Letters 2001, 79(19):3083-3085.

7. Liang J. Y., Chik H., Yin A. J., Xu J.: Two-dimensional lateral superlattices of nanostructures: Nonlithographic formation by anodic membrane template. Journal of Applied Physics 2002, 91(4):2544-2546.
8. Basu S., Chatterjee S., Saha M., Bandyopadhay S., Mistry K. K., Sengupta K: Study of electrical characteristics of porous alumina sensors for detection of low moisture in gases. Sensors and Actuators B-Chemical 2001, 79(2-3):182-186.
9. Yang B. C., Uchida M., Kim H. M., Zhang X. D., Kokubo T.: Preparation of bioactive titanium metal via anodic oxidation treatment. Biomaterials 2004, 25(6):1003-1010.
10. Mor G. K., Shankar K., Paulose M., Varghese O. K., Grimes C. A.: Enhanced photocleavage of water using titania nanotube arrays. Nano Letters 2005, 5(1):191-195.
11. Keller F., Hunter M. S., Robinson D. L.: Structural features of oxide coatings on aluminum. Journal of the Electrochemical Society 1953, 100(9):411-419.
12. Osulliva J. P., Wood G. C.: Morphology and mechanism of formation of porous anodic films on aluminum. Proceedings of the Royal Society of London Series a-Mathematical and Physical

Sciences 1970, 317(1531):511-543.

13. Thompson G. E., Furneaux R. C., Wood G. C., Richardson J. A., Goode J. S.: Nucleation and growth of porous anodic films on aluminium. Nature 1978, 272(5652):433-435.

14 Jessensky O., Muller F., Gosele U.: Self-organized formation of hexagonal pore arrays in anodic alumina. Applied Physics Letters 1998, 72(10):1173-1175.

15. Mukherjee N., Paulose M., Varghese O. K., Mor G. K., Grimes C. A.: Fabrication of nanoporous tungsten oxide by galvanostatic anodization. Journal of Materials Research 2003, 18(10):2296-2299.

16. Tsuchiya H., Macak J. M., Sieber I., Schmuki P.: Self-organized high-aspect-ratio nanoporous zirconium oxides prepared by electrochemical anodization. Small 2005, 1(7):722-725.

17. Gong D., Grimes C. A., Varghese O. K., Hu W. C., Singh R. S., Chen Z., Dickey E. C.: Titanium oxide nanotube arrays prepared by anodic oxidation. Journal of Materials Research 2001, 16(12):3331-3334.

18. Macak J. M., Tsuchiya H., Schmuki P.: High-aspect-ratio TiO_2 nanotubes by anodization of titanium. Angewandte Chemie-International Edition 2005, 44(14):2100-2102.

19. Paulose M., Shankar K., Yoriya S., Prakasam H. E., Varghese O. K., Mor G. K., Latempa T. A., Fitzgerald A., Grimes C. A.:

Anodic growth of highly ordered TiO_2 nanotube arrays to 134 μm in length. J Phys Chem B 2006, 110(33):16179-16184.

20. Sieber I., Kannan B., Schmuki P.: Self-assembled porous tantalum oxide prepared in H_2SO_4/HF electrolytes. Electrochemical and Solid State Letters 2005, 8(3):J10-J12.
21. Tsuchiya H., Schmuki P.: Self-organized high aspect ratio porous hafnium oxide prepared by electrochemical anodization. Electrochemistry Communications 2005, 7(1):49-52.
22. Sieber I., Hildebrand H., Friedrich A., Schmuki P.: Formation of self-organized niobium porous oxide on niobium. Electrochemistry Communications 2005, 7(1):97-100.
23. Stefanovich G. B., Pergament A. L., Velichko A. A., Stefanovich L. A.: Anodic oxidation of vanadium and properties of vanadium oxide films. Journal of Physics-Condensed Matter 2004, 16(23):4013-4024.
24. Hoar T. P., Mott N. F.: A mechanism for the formation of porous anodic oxide films on aluminum. Journal of Physics and Chemistry of Solids 1959, 9(2):97-99.
25. Heber K. V.: Studies on porous Al_2O_3 growth Physical model. Electrochimica Acta 1978, 23(2):127-133.
26. Adachi M., Murata Y., Harada M., Yoshikawa S.: Formation of titania nanotubes with high photo-catalytic activity. Chemistry Letters 2000(8):942-943.

27. Chu S. Z., Inoue S., Wada K., Li D., Haneda H., Awatsu S.: Highly porous (TiO_2-SiO_2-TeO_2)/Al_2O_3/TiO_2 composite nanostructures on glass with enhanced photocatalysis fabricated by anodization and sol-gel process. J Phys Chem B 2003, 107(27):6586-6589.

28. Varghese O. K., Gong D. W., Paulose M., Ong K. G., Dickey E. C., Grimes C. A.: Extreme changes in the electrical resistance of titania nanotubes with hydrogen exposure. Advanced Materials 2003, 15(7-8):624-627.

29. Mor G. K., Carvalho M. A., Varghese O. K., Pishko M. V., Grimes C. A.: A room-temperature TiO_2-nanotube hydrogen sensor able to self-clean photoactively from environmental contamination. Journal of Materials Research 2004, 19(2):628-634.

30. Varghese O. K., Mor G. K., Grimes C. A., Paulose M., Mukherjee N.: A titania nanotube-array room-temperature sensor for selective detection of hydrogen at low concentrations. Journal of Nanoscience and Nanotechnology 2004, 4(7):733-737.

31. Paulose M., Varghese O. K., Mor G. K., Grimes C. A., Ong K. G.: Unprecedented ultra-high hydrogen gas sensitivity in undoped titania nanotubes. Nanotechnology 2006, 17(2):398-402.

32. Mor G. K., Shankar K., Varghese O. K., Grimes C. A.: Photoelectrochemical properties of titania nanotubes. Journal of Materials Research 2004, 19(10):2989-2996.

33. Varghese O. K., Paulose M., Shankar K., Mor G. K., Grimes C. A.: Water-photolysis properties of micron-length highly-ordered titania nanotube-arrays. Journal of Nanoscience and Nanotechnology 2005, 5(7):1158-1165.
34. Uchida S., Chiba R., Tomiha M., Masaki N., Shirai M.: Application of titania nanotubes to a dye-sensitized solar cell. Electrochemistry 2002, 70(6):418-420.
35. Adachi M., Murata Y., Okada I., Yoshikawa S.: Formation of titania nanotubes and applications for dye-sensitized solar cells. Journal of the Electrochemical Society 2003, 150(8):G488-G493.
36. Paulose M., Shankar K., Varghese O. K., Mor G. K., Hardin B., Grimes C. A.: Backside illuminated dye-sensitized solar cells based on titania nanotube array electrodes (vol 17, pg 1446, 2006). Nanotechnology 2010, 21(38).
37. Zwilling V., Aucouturier M., Darque-Ceretti E.: Anodic oxidation of titanium and TA6V alloy in chromic media. An electrochemical approach. Electrochimica Acta 1999, 45(6):921-929.
38. Mor G. K., Varghese O. K., Paulose M., Shankar K., Grimes C. A.: A review on highly ordered, vertically oriented TiO_2 nanotube arrays: Fabrication, material properties, and solar energy applications. Sol Energy Mater Sol Cells 2006, 90(14):2011-2075.
39. Mor G. K., Varghese O. K., Paulose M., Grimes C. A.: A

self-cleaning, room-temperature titania-nanotube hydrogen gas sensor. Sensor Letters 2003, 1(1):42-46.

40. Ruan C. M., Paulose M., Varghese O. K., Grimes C. A.: Enhanced photo electrochemical-response in highly ordered TiO_2 nanotube-arrays anodized in boric acid containing electrolyte. Sol Energy Mater Sol Cells 2006, 90(9):1283-1295.
41. Cai Q. Y., Paulose M., Varghese O. K., Grimes C. A.: The effect of electrolyte composition on the fabrication of self-organized titanium oxide nanotube arrays by anodic oxidation. Journal of Materials Research 2005, 20(1):230-236.
42. Beranek R., Hildebrand H., Schmuki P.: Self-organized porous titanium oxide prepared in H_2SO_4/HF electrolytes. Electrochemical and Solid State Letters 2003, 6(3):B12-B14.
43. Macak J. M., Sirotna K., Schmuki P.: Self-organized porous titanium oxide prepared in Na_2SO_4/NaF electrolytes. Electrochimica Acta 2005, 50(18):3679-3684.
44. Shankar K., Mor G. K., Prakasam H. E., Yoriya S., Paulose M., Varghese O. K, Grimes C. A.: Highly-ordered TiO_2 nanotube arrays up to 220 μm in length: use in water photoelectrolysis and dye-sensitized solar cells. Nanotechnology 2007, 18(6).
45. Paulose M., Prakasam H. E., Varghese O. K., Peng L., Popat K. C., Mor G. K., Desai T. A., Grimes C. A.: TiO_2 nanotube arrays of 1000 μm length by anodization of titanium foil: Phenol red

diffusion. J Phys Chem C 2007, 111(41):14992-14997.

46. Alivov, Fan, and Johnstone, Titanium nanotubes grown by titanium anodization. J. Appl. Phys., 2009, 106, 034314

47. Taveira L. V., Macak J. M., Tsuchiya H., Dick L. F. P., Schmuki P.: Initiation and growth of self-organized TiO_2 nanotubes anodically formed in $NH_4F/(NH_4)_2SO_4$ electrolytes. Journal of the Electrochemical Society 2005, 152(10):B405-B410.

48. Su Z. X., Zhou W. Z.: Formation mechanism of porous anodic aluminum and titanium oxides. Advanced Materials 2008, 20(19):3663-3667.

49. Martin C. R.: Membrane-based synthesis of nanomaterials. Chemistry of Materials 1996, 8(8):1739-1746.

50. Energy Modeling of Electrochemical Anodization Process of Titanium Dioxide Nanotubes, Bingbing L., Xianfeng G., Hong-Chao Z., Chris Y., ACS Sustainable Chem. Eng. 2014, 2, 404－410

51. Minagar S., Berndt C. C., Wang J., Ivanova E., Wen C.: A review of the application of anodization for the fabrication of nanotubes on metal implant surfaces. Acta Biomater 2012, 8(8):2875-2888.

52. Study on titania nanotube arrays prepared by titanium anodization in NH_4F/H_2SO_4 solution, Tian T., Xiu-feng X., Rong-fang L., Hou-de S., Xiao-feng H., J. Mater. Sci., 2007, 42, 5539−5543]

53. Hebert K. R., Wu H. Q., Gessmann T., Lynn K.: Positron

annihilation spectroscopy study of interfacial defects formed by dissolution of aluminum in aqueous sodium hydroxide. Journal of the Electrochemical Society 2001, 148(2):B92-B100.

54. Huang R. C., Hebert K. R., Gessmann T., Lynn K. G.: Effect of impurities on interfacial void formation in aluminum. Journal of the Electrochemical Society 2004, 151(4):B227-B232.

55. Chao C. Y., Lin L. F., Macdonald D. D.: A point-defect model for anodic passive films .1. film growth-kinetics. Journal of the Electrochemical Society 1981, 128(6):1187-1194.

56. Lin L. F., Chao C. Y., Macdonald D. D.: A point-defect model for anodic passive films .2. Chemical breakdown and pit initiation. Journal of the Electrochemical Society 1981, 128(6):1194-1198.

57. N. Vlachopoulos, P. Liska, J. Augustynski, M. Graetzel, Very efficient visible light energy harvesting and conversion by spectral sensitization of high surface area polycrystalline titanium dioxide films, J. Am. Chem. Soc., 1988, 110 (4), 1216−1220.

58. A low-cost, high-efficiency solar cell based on dye-sensitized colloidal TiO_2 films Brian O'Regan ; Michael Grätzel Nature, 1991, Vol.353(6346), 737-740

59. Dye-sensitized solar cells, Hagfeldt, Anders ; Boschloo, Gerrit ; Sun, Licheng ; Kloo, Lars ; Pettersson, Henrik, Chemical reviews, 10 November 2010, Vol.110(11), pp.6595-663

60. Conversion of light to electricity by cis-X_2 Bis(2,2'-bipyridyl-4,4'-dicarboxylate)ruthenium(II) charge-transfer sensitizers (X = Cl-, Br-, I-, CN-, and SCN- on nanocrystalline TiO_2 electrodes , Nazeeruddin, M. K. ; Kay, A. ; Rodicio, I. ; Humphry-Baker, R. ; Mueller, E. ; Liska, P. ; Vlachopoulos, N. ; Graetzel, M., Journal of the American Chemical Society, 1993, Vol.115(14) 6382-6390

61. Photovoltaic Technology: The Case for Thin-Film Solar Cells , Shah, A. ; Torres, P. ; Tscharner, R. ; Wyrsch, N. ; Keppner, H. , Science, 30 July 1999, Vol.285(5428), pp.692-698

62. Photoelectrochemical cells , Michael Grätzel, Nature, 2001, Vol.414(6861), p.338-344

63. Applied physics: Solar cells to dye for , Gratzel, Michael , Nature, Feb 6, 2003, Vol.421(6923), p.586(2)

64. Dye-sensitized solar cells , Grätzel, Michael , Journal of Photochemistry & Photobiology, C: Photochemistry Reviews, 2003, Vol.4(2), pp.145-153

65. Conversion of sunlight to electric power by nanocrystalline dye-sensitized solar cells , Grätzel, Michael , Journal of Photochemistry & Photobiology, A: Chemistry, 2004, Vol.164(1), pp.3-14

66. Light and energy—dye solar cells for the 21st century , Tulloch, Gavin E. , Journal of Photochemistry and Photobiology A:

Chemistry, 6/2004, Vol.164(1-3), pp.209-219

67. Review of photovoltaic technologies , El Chaar, L. ; Lamont, L.A. ; El Zein, N. , Renewable and Sustainable Energy Reviews, 2011, Vol.15(5), pp.2165-2175

68. The advent of mesoscopic injection solar cells , Grätzel, Michael , Progress in Photovoltaics: Research and Applications, 2006, Vol.14(5), pp.429-442

69. Khan, Md. A Study on the Optimization of Dye-Sensitized Solar Cells, Graduate theses and dissertation, University of South Florida, usa, 2013 , ISBN: 9781303007453

70. Review on nanostructured photoelectrodes for next generation dye-sensitized solar cells, Macaira, Jose ; Andrade, Luisa ; Mendes, Adelio, Renewable and Sustainable Energy Reviews, Nov, 2013, Vol.27, p.334(16)

71. Dye-sensitized solar cells: A brief overview , Nazeeruddin, Md. K. ; Baranoff, Etienne ; Grätzel, Michael , Solar Energy, 2011, Vol.85(6), pp.1172-1178

72. Nanocrystalline titanium oxide electrodes for photovoltaic applications , Barbe, C.J. ; Arendse, F. ; Comte, P. ; Jirousek, M. ; Lenzmann, F. ; Shklover, V. ; Graetzel, M. , Journal of the American Ceramic Society, 1997, Vol.80(12), pp.3157-3171

73. Combined experimental and DFT-TDDFT computational study of photoelectrochemical cell ruthenium sensitizers , Nazeeruddin,

Mohammad K ; De Angelis, Filippo ; Fantacci, Simona ; Selloni, Annabella ; Viscardi, Guido ; Liska, Paul ; Ito, Seigo ; Takeru, Bessho ; Grätzel, Michael , Journal of the American Chemical Society, 7 December 2005, Vol.127(48), pp.16835-16847

74. Y. V. Zubavichus, Y. L. Slovokhotov, M. K. Nazeeruddin, S. M. Zakeeruddin, M. , Grätzel, and V. Shklover, Structural Characterization of Solar Cell Prototypes Based on Nanocrystalline TiO2 Anatase Sensitized with Ru Complexes. X-ray Diffraction, XPS, and XAFS Spectroscopy Study, Chem. Mater., 2002, 14(8), 3556−3563.
75. Review on dye-sensitized solar cells (DSSCs): Fundamental concepts and novel materials , Gong, Jiawei ; Liang, Jing ; Sumathy, K. , Renewable and Sustainable Energy Reviews, October 2012, Vol.16(8), pp.5848-5860
76. Electrolytes in Dye-Sensitized Solar Cells , Wu, Jh ; Lan, Z ; Lin, Jm ; Huang, Ml ; Huang, Yf ; Fan, Lq ; Luo, Gg. , Chemical Reviews, 2015 Mar 11, Vol.115(5), pp.2136-2173
77. Progress on the electrolytes for dye-sensitized solar cells , Wu, Jihuai ; Lan, Zhang ; Hao, Sanchun ; Li, Pingjiang ; Lin, Jianming ; Huang, Miaoliang ; Fang, Leqing ; Huang, Yunfang , Pure and Applied Chemistry, 2008, Vol.80(11), pp.2241-2258
78. Liquid electrolytes for dye-sensitized solar cells , Yu, Ze ; Vlachopoulos, Nick ; Gorlov, Mikhail ; Kloo, Lars , Dalton

Transactions, Dalton Transactions, 2011, Vol.40(40), pp.10289-10303

79. Charge Recombination in Dye-Sensitized Nanocrystalline TiO_2 Solar Cells , Huang, S. Y. ; Schlichthörl, G. ; Nozik, A. J. ; Grätzel, M. ; Frank, A. J. , The Journal of Physical Chemistry B, 04/1997, Vol.101(14), pp.2576-2582

80. Quantification of the effect of 4-tert-butylpyridine addition to I^-/I_3^- redox electrolytes in dye-sensitized nanostructured TiO_2 solar cells , Boschloo, Gerrit ; Häggman, Leif ; Hagfeldt, Anders , The journal of physical chemistry. B, 6 July 2006, Vol.110(26), pp.13144-13150

81. Effect of an Adsorbent on Recombination and Band-Edge Movement in Dye-Sensitized TiO_2 Solar Cells: Evidence for Surface Passivation , Frank, A. J. ; Kopidakis, N. ; Neale, N. R. , Journal of Physical Chemistry B, 2006, Vol.110(2006), pp.12485-12489

82. Influence of surface area on charge transport and recombination in dye-sensitized TiO_2 solar cells , Zhu, Kai ; Kopidakis, Nikos ; Neale, Nathan R ; Van De Lagemaat, Jao ; Frank, Arthur J , The journal of physical chemistry. B, 21 December 2006, Vol.110(50), pp.25174-80

83. Mechanism of enhanced performance of dye-sensitized solar cell based TiO_2 films treated by titanium tetrachloride , Zeng,

Long-Yue ; Dai, Song-Yuan ; Wang, Kong-Jia ; Pan, Xu ; Shi, Cheng-Wu ; Guo, Li ; Shi, Cheng-Wu , Chinese Physics Letters, September 2004, Vol.21(9), pp.1835-1837

84. Recent developments in molecule-based organic materials for dye-sensitized solar cells , Yen, Yung-Sheng ; Chou, Hsien-Hsin ; Chen, Yung-Chung ; Hsu, Chih-Yu ; Lin, Jiann T. , Journal of Materials Chemistry, 14 May 2012, Vol.22(18), pp.8734-8747
85. A review on counter electrode materials in dye-sensitized solar cells , Thomas, Sara ; Deepak, T. G. ; Anjusree, G. S. ; Arun, T. A. ; Nair, Shantikumar V. ; Nair, A. Sreekumaran , Journal of Materials Chemistry A, 2014, Vol.2(13), pp.4474-4490
86. Jihuai Wu, Zhang Lan, Sanchun Hao, Pingjiang Li, Jianming Lin, Miaoliang Huang, Leqing Fang, and Yunfang Huang, Pure Appl. Chem., Vol. 80, No. 11, pp. 2241–2258, 2008.
87. A. J. Frank, N. Kopidakis, J. V. D. Lagemaat. Coord. Chem. Rev. 248, 1165 (2004).
88. S. A. Haque, E. Palomares, B. M. Cho, A. N. M. Green. J. Am. Chem. Soc. 127, 3456 (2005).
89. A. Hagfeldt, M. Gratzel. Chem. Rev. 95, 49 (1995).
90. N. S. Sariciftci, L. Smilowitz, A. J. Heeger, F. Wudl. Science 258, 1474 (1992).
91. G. Benko, J. Kallioinen, A. P. Yartsev, V. Sundstrom. J. Am. Chem. Soc. 124, 489 (2002).

92. J. Schnadt, P. A. Bruhwiler, L. Patthey, J. N. O'Shea, S. Sodergren. Nature 418, 620 (2002).

93. W. Stier, W. R. Duncan, O. V. Prezhdo. Adv. Mater. 16, 240 (2004).

94. J. Ashbury, E. Hao, Y. Wang, H. N. Ghosh, T. Lian. J. Phys. Chem. B 105, 4545 (2001).

95. Boyuan Qi and Jizheng Wang J. Mater. Chem., 2012, 22, 24315–24325

96. T. Marinado, K. Nonomura, J. Nissfolk, M. K. Karlsson, D. P. Hagberg, L. Sun, S. Mori, and A. Hagfeldt, How the Nature of Triphenylamine-Polyene Dyes in Dye-Sensitized Solar Cells Affects the Open-Circuit Voltage and Electron Lifetimes, Langmuir, 2010, 26, 2592

97. Open circuit voltage of organic solar cells: an in-depth review, Elumalai, Naveen Kumar ; Uddin, Ashraf , Energy & Environmental Science, 2016, Vol.9(2), pp.391-410

98. Polydisperse Aggregates of ZnO Nanocrystallites: A Method for Energy Conversion Efficiency Enhancement in Dye Sensitized Solar Cells , Zhang, Qifeng ; Chou, Tammy P. ; Russo, Bryan ; Jenekhe, Samson A. ; Cao, Guozhong , Advanced Functional Materials, 2008, Vol.18(11), pp.1654-1660

99. Study of the equivalent circuit of a dye sensitized solar cells, M. Belarbi , A. Benyoucef, B. Benyoucef , Advanced Energy: An

International Journal (AEIJ), Vol. 1, No. 2, April 2014,1,2-1-8

100. Series resistance effects on solar cell measurements, Martin Wolf, Hans rauschenbacht, Advanced Energy Conversion. Vol. 3, pp. 455-479.

101. Competition between recombination and extraction of free charges determines the fill factor of organic solar cells , Bartesaghi, Davide ; Perez, Irene del Carmen ; Kniepert, Juliane ; Roland, Steffen ; Turbiez, Mathieu ; Neher, Dieter ; Koster, L. Jan Anton , Nature Communications, 2015, Vol.6, pp.7083- urn:issn:2041-1723

102. M. Grätzel, Recent Advances in Sensitized Mesoscopic Solar Cells, Acc. Chem. Res., 2009, 42 (11), 1788-1798.

103. L. Meng, and C. Li, Blocking Layer Effect on Dye-Sensitized Solar Cells Assembled with TiO_2 Nanorods Prepared by DC Reactive Magnetron Sputtering, Nanoscience and Nanotechnology Letters, 2011, 3(2), 181−185.

104. P. J. Cameron and L. M. Peter, Characterization of Titanium Dioxide Blocking Layers in Dye-Sensitized Nanocrystalline Solar Cells, J. Phys. Chem. B, 2003, 107, 14394-14400.

105. A. Burke, S. Ito, H. Snaith, U. Bach, J. Kwiatkowski, and M. Grätzel, The Function of a TiO_2 Compact Layer in Dye-Sensitized Solar Cells Incorporating “Planar” Organic Dyes, Nano Lett., 2008, 8(4), 977−981.

106. Park J. H., Choi K. J., Kim J., Kang Y. S., Lee S. S.: Effect of molecular weight of oligomer on ionic diffusion in oligomer electrolytes and its implication for dye-sensitized solar cells. Journal of Power Sources 2007, 173(2):1029-1033.

107. S. Ito, T. N. Murakami, P. Comte, P. Liska, C. Grätzel, M. K. Nazeeruddin, M. Grätzel, Fabrication of thin film dye sensitized solar cells with solar to electric power conversion efficiency over 10%, Thin Solid Films, 2008, 516(14), 4613-4619.

108. S. Ito, P. Liska, P. Comte, R. Charvet, P. Péchy, U. Bac, L. Schmidt-Mende, S. M. Zakeeruddin, A. Kay, M. K. Nazeeruddin, and M. Grätzel, Control of dark current in photoelectrochemical (TiO_2/I^- I_3^-) and dye-sensitized solar cells, Chem. Commun., 2005, 34, 4351-4353.

109. E. Palomares, J. N. Clifford, S. A. Haque, T. Lutz, and J. R. Durrant, Control of Charge Recombination Dynamics in Dye Sensitized Solar Cells by the Use of Conformally Deposited Metal Oxide Blocking Layers, J. Am. Chem. Soc., 2003, 125(2), 475-482.

110. Z. Wang, T. Yamaguchi, H. Sugihara, and H. Arakawa, Significant Efficiency Improvement of the Black Dye-Sensitized Solar Cell through Protonation of TiO_2 Films, Langmuir, 2005, 21(10), 4272-4276.

111. Influence of dye-concentration on the light-scattering effect in

dye-sensitized solar cell , Kyung-Jun Hwang, Dong-Won Park, Sungho Jin, Sang Ook Kang, Dae Won Cho, Materials Chemistry and Physics 149-150 (2015) 594-600

112. A ZnO nanorod layer with a superior light-scattering effect for dye-sensitized solar cells , Gao, Rui ; Liang, Zhiqiang ; Tian, Jianjun ; Zhang, Qifeng ; Wang, Liduo ; Cao, Guozhong , RSC Advances, 2013, Vol.3(40), pp.18537-18543

113. Mesoporous multi-shelled ZnO microspheres for the scattering layer of dye sensitized solar cell with a high efficiency , Xia, Weiwei ; Mei, Chao ; Zeng, Xianghua ; Chang, Shuai ; Wu, Guoqing ; Shen, Xiaoshuang , Applied Physics Letters, 14 March 2016, Vol.108(11)

114. Size-dependent light-scattering effects of nanoporous TiO 2 spheres in dye-sensitized solar cells , Yu, In Gyoung ; Kim, Yong Joo ; Kim, Hark Jin ; Lee, Wan In ; Lee, Chongmu , Journal of Materials Chemistry, 14 January 2011, Vol.21(2), pp.532-538

115. Analysis on the Light-Scattering Effect in Dye-Sensitized Solar Cell according to the TiO_2 Structural Differences , Son, Min-Kyu ; Seo, Hyunwoong ; Kim, Soo-Kyoung ; Hong, Na-Yeong ; Kim, Byung-Man ; Park, Songyi ; Prabakar, Kandasamy ; Kim, Hee-Je , International Journal of Photoenergy, 2012, Vol.2012, 8 pages

116. The effect of light-scattering layer on the performance of

dye-sensitized solar cell assembled using TiO_2 double-layered films as photoanodes , Zhu, L. ; Zhao, Y.L. ; Lin, X.P. ; Gu, X.Q. ; Qiang, Y.H. , Superlattices and Microstructures, January 2014, Vol.65, pp.152-160

117. Double-layer dye-sensitized solar cells based on Zn-doped TiO_2 transparent and light scattering layers: Improving electron injection and light scattering effect , Ghanbari Niaki, A.H. ; Bakhshayesh, A.M. ; Mohammadi, M.R. , Solar Energy, May 2014, Vol.103, pp.210-222
118. A ZnO nanorod layer with a superior light-scattering effect for dye-sensitized solar cells , Gao, Rui ; Liang, Zhiqiang ; Tian, Jianjun ; Zhang, Qifeng ; Wang, Liduo ; Cao, Guozhong , RSC Advances, 2013, Vol.3(40), pp.18537-18543
119. Observation of positive effects of freestanding scattering film in Dye-Sensitized solar cells , Shin, Kahee ; Park, Jong Hyeok ; Jun, Yongseok ; Moon, Jun Hyuk , ACS Applied Materials and Interfaces, 27 January 2010, Vol.2(1), pp.288-291
120. Thickness effect of the TiO_2 nanofiber scattering layer on the performance of the TiO_2 nanoparticle/TiO_2 nanofiber-structured dye-sensitized solar cells , Lee, Ji - Hye ; Ahn, Kyun ; Kim, Soo Hyung ; Kim, Jong Man ; Jeong, Se - Young ; Jin, Jong - Sung ; Jeong, Euh Duck ; Cho, Chae ⁻ Ryong , Current Applied Physics, June, 2014, Vol.14(6), p.856(6)

121. Dye Sensitized Solar Cells: Resonant Multiple Light Scattering for Enhanced Photon Harvesting in Dye Sensitized Solar Cells (Adv. Mater. 30/2014 , Kim, Jihun ; Lee, Horim ; Kim, Dong Young ; Seo, Yongsok , Advanced Materials, 2014, Vol.26(30), pp.5191-5191

122. Hexagonal TiO_2 microplates with superior light scattering for dye-sensitized solar cells , Peng, Wenqin ; Han, Liyuan ; Han, Liyuan , Journal of Materials Chemistry, 14 October 2012, Vol.22(38), pp.20773-20777

123. Sandwich-like design of TiO_2 electrodes containing multiple light scattering layers for dye-sensitized solar cells applications , Bakhshayesh, A.M. , Thin Solid Films, 2 November 2015, Vol.594, pp.88-95

124. Ordered Mesoporous Particles in Titania Films with Hierarchical Structure as Scattering Layers in Dye-Sensitized Solar Cells , Xiong, Y. ; He, D. ; Jin, Y. ; Cameron, P.J. ; Edler, K.J. , Journal of Physical Chemistry C, 8 September 2015, Vol.119(39), pp.22552-22559

125. Tunable synthesis of single-crystalline-like TiO_2 mesocrystals and their application as effective scattering layer in dye-sensitized solar cells , Wu, Dapeng ; Cao, Kun ; Wang, Hongju ; Wang, Fujuan ; Gao, Zhiyong ; Xu, Fang ; Guo, Yuming ; Jiang, Kai , Journal of Colloid And Interface Science, 15 October 2015,

Vol.456, pp.125-131

126. A simple method to achieve light scattering in dye-sensitized solar cells using a low-temperature-sintering TiO_2 paste , Jung, You-Ra ; Park, Ju-Young ; Gu, Hal-Bon , Materials Letters, 1 January 2015, Vol.138, pp.268-271

127. Tunable synthesis of single-crystalline-like TiO_2 mesocrystals and their application as effective scattering layer in dye-sensitized solar cells , Wu, Dapeng ; Cao, Kun ; Wang, Hongju ; Wang, Fujuan ; Gao, Zhiyong ; Xu, Fang ; Guo, Yuming ; Jiang, Kai, Journal of Colloid And Interface Science, Oct 15, 2015, Vol.456, p.125(7)

128. The use of silicon carbide as scattering layer in dye sensitized solar cell (DSSC) , Ahmad, Z. , Journal of Ovonic Research, July/August 2014, Vol.10(4), pp.109-113

129. Preparation of composite light-scattering layer for dye sensitized solar cells , Wang, Hsiou - Hsuan ; Su, Chaochin ; Wu, Chung - Ying ; Tsai, Hon - Bin ; Li, Chung - Yen ; Li, Wen ‐ Ren , Thin Solid Films, Feb 1, 2013, Vol.529, p.15(4)

130. Large-diameter titanium dioxide nanotube arrays as a scattering layer for high-efficiency dye-sensitized solar cell , Liu, Xiaolin ; Guo, Min ; Cao, Jianjun ; Lin, Jia ; Tsang, Yuen ; Chen, Xianfeng ; Huang, Haitao , Nanoscale Research Letters, 2014, Vol.9(1), pp.1-5

131. The Performance of Dye-sensitized Solar Cell Using Light-scattering Layer , Eom, Tae-Sung ; Choi, Hyung-Wook , Journal of the Korean Institute of Electrical and Electronic Material Engineers, 07/01/2012, Vol.25(7), pp.558-562

132. Meier J, Dubail S, Golay S, Kroll U, Fay S, Vallat-Sauvain E, Feitknecht L, Dubail J, Shah A: Microcrystalline silicon and the impact on micromorph tandem solar cells. Sol Energy Mater Sol Cells 2002, 74(1-4):457-467.

133. Muller J, Rech B, Springer J, Vanecek M: TCO and light trapping in silicon thin film solar cells. Solar Energy 2004, 77(6):917-930.

134. Nie S. M., Emery S. R.: Probing single molecules and single nanoparticles by surface-enhanced Raman scattering. Science 1997, 275(5303):1102-1106.

135. Moskovits M: Surface-enhanced spectroscopy. Reviews of Modern Physics 1985, 57(3):783-826.

136. Review of surface plasmon resonance and localized surface plasmon resonance sensor , Chen, Yong ; Ming, Hai , Photonic Sensors, 2012, Vol.2(1), pp.37-49

137. Physics: Molecular Plasmonics , Van Duyne, R. P. , Science, 11/05/2004, Vol.306(5698), pp.985-986

138. Plasmonic Materials for Surface-Enhanced Sensing and Spectroscopy , Haes, Amanda J. ; Haynes, Christy L. ;

Mcfarland, Adam D. ; Schatz, George C. ; Van Duyne, Richard P. ; Zou, Shengli , MRS Bulletin, 5/2005, Vol.30(05), pp.368-375

139. Rapid detection of an anthrax biomarker by surface-enhanced Raman spectroscopy , Zhang, Xiaoyu ; Young, Matthew A ; Lyandres, Olga ; Van Duyne, Richard P , Journal of the American Chemical Society, 30 March 2005, Vol.127(12), pp.4484-9

140. Localized Surface Plasmon Resonance Spectroscopy and Sensing , Willets, Katherine A. ; Van Duyne, Richard P. , 2007, Vol.58, p.267-297

141. Nanoparticle-based plasmonic organic photovoltaic devices , Stratakis, Emmanuel ; Kymakis, Emmanuel , Materials Today, April 2013, Vol.16(4), pp.133-146

142. Plasmonic nanostructures for light trapping in organic photovoltaic devices , Chou, Chun-Hsien ; Chen, Fang-Chung , Nanoscale, 2014, Vol.6(15), pp.8444-8458

143. Plasmonics for improved photovoltaic devices , Harry A. Atwater ; Albert Polman , Nature Materials, 2010, Vol.9(3), p.205

144. Chen Q. W., Xu D. S.: Large-Scale, noncurling, and free-standing crystallized TiO_2 nanotube arrays for dye-sensitized solar cells. J Phys Chem C 2009, 113(15):6310-6314.

145. Ghicov A., Albu S. P., Hahn R., Kim D., Stergiopoulos T., Kunze J., Schiller C. A., Falaras P., Schmuki P.: TiO_2 nanotubes

in dye-sensitized solar sells: Critical factors for the conversion efficiency. Chemistry-an Asian Journal 2009, 4(4):520-525.

146. Rho C, Suh J. S.: Filling TiO_2 nanoparticles in the channels of TiO_2 nanotube membranes to enhance the efficiency of dye-sensitized solar cells. Chemical Physics Letters 2011, 513(1-3):108-111.

147. Jung H. Y., Jung S. M., Gu G. H., Suh J. S.: Anodic aluminum oxide membrane bonded on a silicon wafer for carbon nanotube field emitter arrays. Applied Physics Letters 2006, 89(1).

148. Green, M. A., Emery, K., Hishikawa, Y., Warta, W. & Dunlop, E. D. Solar cell efficiency tables (version 41). Prog Photovoltaics 21, 1-11, doi:Doi 10.1002/Pip.2352 (2013).

149. Law, M., Greene, L. E., Johnson, J. C., Saykally, R. & Yang, P. D. Nanowire dye-sensitized solar cells. Nat. Mater. 4, 455-459, doi:10.1038/nmat1387 (2005).

150. Mor, G. K., Shankar, K., Paulose, M., Varghese, O. K. & Grimes, C. A. Use of highly-ordered TiO_2 nanotube arrays in dye-sensitized solar cells. Nano Lett 6, 215-218, doi:Doi 10.1021/Nl052099j (2006).

151. Wang, Z. S. et al. A high-light-harvesting-efficiency coumarin dye for stable dye-sensitized solar cells. Adv Mater 19, 1138-1141, doi:DOI 10.1002/adma.200601020 (2007).

152. Chen, C. Y., Wu, S. J., Wu, C. G., Chen, J. G. & Ho, K. C. A

ruthenium complex with superhigh light-harvesting capacity for dye-sensitized solar cells. Angew Chem Int Edit 45, 5822-5825, doi:DOI 10.1002/anie.200601463 (2006).

153. Gao, F. et al. Enhance the optical absorptivity of nanocrystalline TiO_2 film with high molar extinction coefficient ruthenium sensitizers for high performance dye-sensitized solar cells. J Am Chem Soc 130, 10720-10728, doi:Doi 10.1021/Ja801942j (2008).

154. Hagberg, D. P. et al. Tuning the HOMO and LUMO energy levels of organic chromophores for dye sensitized solar cells. J Org Chem 72, 9550-9556, doi:Doi 10.1021/Jo701592x (2007).

155. Yang, W. G., Wan, F. R., Chen, Q. W., Li, J. J. & Xu, D. S. Controlling synthesis of well-crystallized mesoporous TiO_2 microspheres with ultrahigh surface area for high-performance dye-sensitized solar cells. J Mater Chem 20, 2870-2876, doi:Doi 10.1039/B923105f (2010).

156. Hara, K., Miyamoto, K., Abe, Y. & Yanagida, M. Electron transport in coumarin-dye-sensitized nanocrystalline TiO_2 electrodes. J Phys Chem B 109, 23776-23778, doi:Doi 10.1021/Jp055572q (2005).

157. Hamann, T. W., Jensen, R. A., Martinson, A. B. F., Van Ryswyk, H. & Hupp, J. T. Advancing beyond current generation dye-sensitized solar cells. Energ Environ Sci 1, 66-78, doi:Doi 10.1039/B809672d (2008).

158. Dang, X. N. et al. Virus-templated self-assembled single-walled carbon nanotubes for highly efficient electron collection in photovoltaic devices. Nat. Nanotechnol. 6, 377-384, doi:10.1038/nnano.2011.50 (2011).

159. Roy, P., Kim, D., Paramasivam, I. & Schmuki, P. Improved efficiency of TiO_2 nanotubes in dye sensitized solar cells by decoration with TiO_2 nanoparticles. Electrochemistry Communications 11, 1001-1004, doi:10.1016/j.elecom.2009.02.049 (2009).

160. Park, J. H., Lee, T. W. & Kang, M. G. Growth, detachment and transfer of highly-ordered TiO_2 nanotube arrays: use in dye-sensitized solar cells. Chemical Communications, 2867-2869, doi:10.1039/b800660a (2008).

161. Lin, C. J., Yu, W. Y. & Chien, S. H. Transparent electrodes of ordered opened-end TiO_2-nanotube arrays for highly efficient dye-sensitized solar cells. J Mater Chem 20, 1073-1077, doi:10.1039/b917886d (2010).

162. Li, L. L., Chen, Y. J., Wu, H. P., Wang, N. S. & Diau, E. W. G. Detachment and transfer of ordered TiO_2 nanotube arrays for front-illuminated dye-sensitized solar cells. Energ Environ Sci 4, 3420-3425, doi:10.1039/c0ee00474j (2011).

163. Rho, C., Min, J. H. & Suh, J. S. Barrier Layer Effect on the Electron Transport of the Dye-Sensitized Solar Cells Based on

TiO_2 Nanotube Arrays. Journal of Physical Chemistry C 116, 7213-7218, doi:10.1021/jp211708y (2012).

164. Jennings, J. R., Ghicov, A., Peter, L. M., Schmuki, P. & Walker, A. B. Dye-sensitized solar cells based on oriented TiO_2 nanotube arrays: Transport, trapping, and transfer of electrons. J. Am. Chem. Soc. 130, 13364-13372, doi:Doi 10.1021/Ja804852z (2008).

165. Hore, S., Vetter, C., Kern, R., Smit, H. & Hinsch, A. Influence of scattering layers on efficiency of dye-sensitized solar cells. Sol. Energ. Mat. Sol. C 90, 1176-1188, doi:DOI 10.1016/j.solmat.2005.07.002 (2006).

166. Zhang, Z. P. et al. The electronic role of the TiO2 light-scattering layer in dye-sensitized solar cells. Z. Phys. Chemie-Int. J. Res. Phys. Chem. Chem. Phys. 221, 319-327, doi:10.1524/zpch.2007.221.3.319 (2007).

167. Koo, H. J. et al. Size-dependent scattering efficiency in dye-sensitized solar cell. Inorganica Chimica Acta 361, 677-683, doi:10.1016/j.ica.2007.05.017 (2008).

168. Lim, J.; Kim, H.A.; Kim, B.H.; Han, C.H.; Jun, Y. Reversely fabricated dye-sensitized solar cells. Rsc Advances 2014, 4, 243-247.

169. Jo, Y.; Yun, Y.J.; Khan, M.A.; Jun, Y. Densely packed setose zno nanorod arrays for dye sensitized solar cells. Synthetic Metals 2014, 198, 137-141.

170. Kim, J.; Lim, J.; Kim, M.; Lee, H.S.; Jun, Y.; Kim, D. Fabrication of carbon-coated silicon nanowires and their application in dye-sensitized solar cells. Acs Applied Materials & Interfaces 2014, 6, 18788-18794.

171. Ko, K.W.; Lee, M.; Sekhon, S.; Balasingam, S.K.; Han, C.H.; Jun, Y. Efficiency enhancement of dye"]sensitized solar cells by the addition of an oxidizing agent to the tio2 paste. ChemSusChem 2013, 6, 2117-2123.

172. Balasingam, S. K.; Kang, M. G.; Jun, Y. Metal substrate based electrodes for flexible dye-sensitized solar cells: Fabrication methods, progress and challenges. Chemical Communications 2013, 49, 11457-11475.

173. Jung, C. L.; Lim, J.; Park, J. H.; Kim, K. H.; Han, C. H.; Jun, Y. High performance dye sensitized solar cells by adding titanate co-adsorbant. RSC Advances 2013, 3, 20488-20491.

174. Nath, N.C.D.; Ahammad, A.; Sarker, S.; Rahman, M.; Lim, S. S.; Choi, W. Y.; Lee, J. J. Carbon nanotubes on fluorine-doped tin oxide for fabrication of dye-sensitized solar cells at low temperature condition. Journal of nanoscience and nanotechnology 2012, 12, 5373-5380.

175. Deb Nath, N.C.; Lee, H.J.; Choi, W.-Y.; Lee, J.-J. Effects of phenylalkanoic acids as co-adsorbents on the performance of dye-sensitized solar cells. Journal of nanoscience and

nanotechnology 2013, 13, 7880-7885.

176. Du, L. C.; Furube, A.:Hara, K.;Katoh, R.;Tachiya, M. Mechanism of particle size effect on electron injection efficiency in ruthenium dye-sensitized TiO_2 nanoparticle films. J. Phys. Chem. C 2010, 114, 8135-8143.

177. Ahn, J.; Lee, K.C.; Kim, D.; Lee, C.; Lee, S.; Cho, D.W.; Kyung, S.; Im, C. Synthesis of novel ruthenium dyes with thiophene or thienothiophene substituted terpyridyl ligands and their characterization. Molecular Crystals and Liquid Crystals 2013, 581, 45-51.

178. Kwon, T.H.; Kim, K.; Park, S.H.; Annamalai, A.; Lee, M.J. Effect of seed particle size and ammonia concentration on the growth of zno nanowire arrays and their photoconversion efficiency. International Journal of Nanotechnology 2013, 10, 681-691.

179. Rho, W. Y.; Kim, H. S.; Lee, S. H.; Jung, S.; Suh, J. S.; Hahn, Y.-B.; Jun, B.-H. Front-illuminated dye-sensitized solar cells with ag nanoparticle-functionalized freestanding tio2 nanotube arrays. Chem Phys Lett 2014, 614, 78-81.

180. Hwang, K. J.; Cho, D. W.; Lee, J. W.; Im, C. Preparation of nanoporous TiO_2 electrodes using different mesostructured silica templates and improvement of the photovoltaic properties of dsscs. New J. Chem. 2012, 36, 2094-2100.

181. Nath, N. C. D.; Kim, J. C.; Kim, K. P.; Yim, S.; Lee, J. J. Deprotonation of N3 adsorbed on TiO_2 for high-performance dye-sensitized solar cells (DSSCs). Journal of Materials Chemistry A 2013, 1, 13439-13442.

182. Nakade, S.; Saito, Y.; Kubo, W.; Kitamura, T.; Wada, Y.; Yanagida, S. Influence of TiO_2 nanoparticle size on electron diffusion and recombination in dye-sensitized TiO_2 solar cells. J. Phys. Chem. B 2003, 107, 8607-8611.

183. Chung, K.-H.; Rahman, M.M.; Son, H.-S.; Lee, J.-J. Development of well-aligned TiO_2 nanotube arrays to improve electron transport in dye-sensitized solar cells. International Journal of Photoenergy 2012, 2012. , 1-6

184. Lee, G. I.; Nath, N. C. D.; Sarker, S.; Shin, W. H.; Ahammad, A. S.; Kang, J. K.; Lee, J. J. Fermi energy level tuning for high performance dye sensitized solar cells using sp^2 selective nitrogen-doped carbon nanotube channels. Physical Chemistry Chemical Physics 2012, 14, 5255-5259.

185. Nath, N. C. D.; Sarker, S.; Ahammad, A. S.; Lee, J. J. Spatial arrangement of carbon nanotubes in TiO_2 photoelectrodes to enhance the efficiency of dye-sensitized solar cells. Physical Chemistry Chemical Physics 2012, 14, 4333-4338.

186. Yadav, S.K.; Madeshwaran, S.R.; Cho, J.W. Synthesis of a hybrid assembly composed of titanium dioxide nanoparticles and thin

multi-walled carbon nanotubes using “click chemistry”. Journal of colloid and interface science 2011, 358, 471-476.

187. Bavykin, D.V.; Parmon, V.N.; Lapkin, A.A.; Walsh, F.C. The effect of hydrothermal conditions on the mesoporous structure of TiO_2 nanotubes. J Mater Chem 2004, 14, 3370-3377.

188. Rho, W. Y.; Jeon, H.; Kim, H. S.; Chung, W. J.; Suh, J. S.; Jun, B. H. Recent progress in dye-sensitized solar cells for improving efficiency: TiO_2 nanotube arrays in active layer. Journal of Nanomaterials 2015, 2015, 1-17.

189. Standridge, S. D.; Schatz, G. C.; Hupp, J. T. Distance dependence of plasmon-enhanced photocurrent in dye-sensitized solar cells. Journal of the American Chemical Society 2009, 131, 8407-9.

190. Brown, M. D.; Suteewong, T.; Kumar, R. S. S.; D'Innocenzo, V.; Petrozza, A.; Lee, M. M.; Wiesner, U.; Snaith, H. J. Plasmonic dye-sensitized solar cells using core-shell metal-insulator nanoparticles. Nano Letters 2011, 11, 438-445.

191. Qi, J. F.; Dang, X. N.; Hammond, P. T.; Belcher, A. M. Highly efficient plasmon-enhanced dye-sensitized solar cells through metal@oxide core-shell nanostructure. Acs Nano 2011, 5, 7108-7116.

192. Rho, W. Y.; Chun, M. H.; Kim, H. S.; Hahn, Y. B.; Suh, J. S.; Jun, B. H. Improved energy conversion efficiency of dye-sensitized solar cells fabricated using open-ended TiO_2

nanotube arrays with scattering layer. Bull. Korean Chem. Soc 2014, 35, 1165.

193. Bhattacharyya, D.; Sarswat, P.K.; Islam, M.; Kumar, G.; Misra, M.; Free, M.L. Geometrical modifications and tuning of optical and surface plasmon resonance behaviour of au and Ag coated TiO_2 nanotubular arrays. RSC Advances 2015, 5, 70361-70370.

194. Garmaroudi, Z. A.; Mohammadi, M. R. Plasmonic effects of infiltrated silver nanoparticles inside TiO_2 film: Enhanced photovoltaic performance in dsscs. Journal of the American Ceramic Society 2015. 99. 167-173

195. Xie, Y.; Wang, X.; Han, X.; Xue, X.; Ji, W.; Qi, Z.; Liu, J.; Zhao, B.; Ozaki, Y. Sensing of polycyclic aromatic hydrocarbons with cyclodextrin inclusion complexes on silver nanoparticles by surface-enhanced Raman scattering. Analyst 2010, 135, 1389-1394.

196. Kim, H. Y.; Rho, W. Y.; Lee, H. Y.; Park, Y. S.; Suh, J. S. Aggregation effect of silver nanoparticles on the energy conversion efficiency of the surface plasmon-enhanced dye-sensitized solar cells. Solar Energy 2014, 109, 61-69.

197. Hardin, B. E.; Snaith, H.J.; McGehee, M. D. The renaissance of dye-sensitized solar cells. Nature Photonics 2012, 6, 162-169.

198. Sang, L.; Zhao, Y.; Burda, C. TiO_2 Nanoparticles as functional building blocks. Chem. Rev. 2014, 114, 9283-9318.

199. Hara, K.; Sato, T.; Katoh, R.; Furube, A.; Ohga, Y.; Shinpo, A.;

Suga, S.; Sayama, K.; Sugihara, H.; Arakawa, H. Molecular design of coumarin dyes for efficient dye-sensitized solar cells J. Phys. Chem. B 2003, 107, 597-606.

200. Galoppini, E. Linkers for anchoring sensitizers to semiconductor nanoparticles. Coordin. Chem. Rev. 2004, 248, 1283-1297.

201. Nazeeruddin, M. K.; Pechy, P.; Renouard, T.; Zakeeruddin, S. M.; Humphry-Baker, R.; Comte, P.; Liska, P.; Cevey, L.; Costa, E.; Shklover, V.; Spiccia, L.; Deacon, G. B. C.; Bignozzi, A.; Grätzel, M. Engineering of efficient panchromatic sensitizers for nanocrystalline TiO_2-based solar cells. J. Am. Chem. Soc., 2001, 123, 1613-1624.

202. Katoh, R.; Furube, A.; Yoshihara, T.; Hara, K.; Fujihashi, G.; Takano, S.; Murata, S.; Arakawa, H.; Tachiya, M. Efficiencies of electron injection from excited N3 into nanocrystalline semiconductor (ZrO_2, TiO_2, ZnO, Nb_2O_5, SnO_2, In_2O_3) films. J. Phys. Chem. B. 2004, 108, 4818-4822.

203. Du, L.; Furube, A.; Yamamoto, K.; Hara, K.; Katoh, R.; Tachiya, M. Plasmon-induced charge separation and recombination dynamics in gold－TiO2 nanoparticle systems: Dependence on TiO_2 particle size. J. Phys. Chem. C 2009, 113, 6454-6462.

204. Mor, G. K.; Varghese, O.K.; Paulose, M.; Shankar, K.; Grimes, C. A. A review on highly ordered, vertically oriented TiO2 nanotube arrays: fabrication, material properties, and solar energy

applications. Sol. Energy Mater. Sol. Cell 2006, 90, 2011-2075.

205. Shin, Y.; Lee, S. Self-organized regular arrays of anodic tio2 nanotubes. Nano Lett. 2008, 8, 3171-3173.

206. Rho, W. Y.; Jeon, H.; Kim, H. S.; Chung, W. J.; Suh J. S.; Jun, B. H. Ag Nanoparticle-functionalized open-ended freestanding TiO_2 nanotube arrays with a scattering layer for improved energy conversion efficiency in dye-sensitized solar cells. J. Nanomater. 2016, 6, 117.

207. Ruan, C. M.; Paulose, M.; Varghese, O. K.; Mor, G.K.; Grimes, C. A. Fabrication of highly ordered TiO_2 nanotube arrays using an organic electrolyte. J. Phys. Chem. B 2005, 109, 15754-15759.

208. Martinson, A.B.; Hamann, T. W.; Pellin, M. J.; Hupp, J. T. New architectures for dye-sensitized solar cells. Chemistry 2008, 14, 4458-4467.

209. Chen Q. W.; Xu, D. S. Large-scale, noncurling, and free-standing crystallized TiO_2 nanotube arrays for dye-sensitized solar cells. J. Phys. Chem. C 2009, 113, 6310-6314.

210. Rho, C.; Min, J. H.; Suh, J. S. barrier layer effect on the electron transport of the dye-sensitized solar cells based on TiO_2 nanotube arrays. J. Phys. Chem. C 2012, 116, 7213-7218.

211. Zhang, H.; Lv, X.; Li, Y.; Wang, Y.; Li, J. P25-graphene composite as a high performance photocatalyst. ACS Nano, 2010, 4, 380-386.

212. Wang, W.; Bando, Y.; Zhi, C.; Fu, W.; Wang, E.; Golberg, D. Aqueous noncovalent functionalization and controlled near-surface carbon doping of multiwalled boron nitride nanotubes. J. Am. Chem. Soc. 2008, 130, 8144-8145.

213. Guo, X.; Baumgarten, M.; Müllen, K. Designing π-conjugated polymers for organic electronics. Prog. Polym. Sci. 2013, 38, 1832-1908.

214. Schulze, K.; Uhrich, C.; Schüppel, R.; Leo, K.; Pfeiffer, M.; Brier, E.; Reinold, E.; Baeuerle, P. Efficient vacuum-deposited organic solar cells based on a new low-bandgap oligothiophene and fullerene C60. Adv. Mater. 2006, 18, 2872-2875.

215. Cheng, Y.-J.; Yang, S.-H.; Hsu, C.-S., Synthesis of conjugated polymers for organic solar cell applications. Chem. Rev. 2009, 109, 5868-5923.

216. Pradhan, B.; Batabyal, S. K.; Pal, A. J., Functionalized carbon nanotubes in donor/acceptor-type photovoltaic devices. Appl. Phys. Lett. 2006, 88, 3106.

217. Roy-Mayhew, J. D.; Aksay, I. A. Graphene materials and their use in dye-sensitized solar cells. Chem. Rev. 2014, 114, 6323-6348.

218. Rho, W. Y.; Kim, S. H.; Kim, H. M.; Suh J. S.; Jun, B. H., Carbon-doped freestanding TiO_2 nanotube arrays in dye-sensitized solar cells. New J. Chem. 2017, 41, 285-289.

219. Lu, L.; Luo, Z.; Xu, T.; Yu, L. Cooperative plasmonic effect of Ag and Au nanoparticles on enhancing performance of polymer solar cells. Nano Lett. 2012, 13, 59-64.

220. Pillai, S.; Catchpole, K.; Trupke, T.; Green, M. Surface plasmon enhanced silicon solar cells. J. Appl. Phys., 2007, 101, 093105.

221. Nakayama, K.; Tanabe, K.; Atwater, H. A. Plasmonic nanoparticle enhanced light absorption in GaAs solar cells. Appl. Phys. Lett., 2008, 93, 121904.

222. Bhattacharyya, D.; Sarswat, P. K.; Islam, M.; Kumar, G.; Misra, M.; Free, M. L. Geometrical modifications and tuning of optical and surface plasmon resonance behaviour of au and Ag coated TiO_2 nanotubular arrays. RSC Adv. 2015, 5, 70361-70370.

223. Rho, W. Y.; Kim, H. S.; Lee, S. H.; Jung, S.; Suh, J. S.; Hahn, Y.-B.; Jun, B.-H. Front-illuminated dye-sensitized solar cells with Ag nanoparticle-functionalized freestanding TiO_2 nanotube arrays. Chem. Phys. Lett. 2014, 614, 78-81.

224. Rho, W. Y.; Chun, M. H.; Kim, H. S.; Kim, H. M.; Suh, J.; Jun, B.-H. Ag Nanoparticle–functionalized open-ended freestanding TiO_2 nanotube arrays with a scattering layer for improved energy conversion efficiency in dye-sensitized solar cells. Nanomaterials., 2016, 6, 117.

225. Yan, J.; Wu, G.; Guan, N.; Li, L.; Li, Z.; Cao, X. Understanding the effect of surface/bulk defects on the photocatalytic activity of

TiO_2: anatase versus rutile. Phys. Chem. Chem. Phys. 2013, 15, 10978-10988.

국 문 초 록

매우 규칙적인 구조를 가지는 이산화티타늄 나노튜브 수직 배열층을 전기화학적 방법으로 제조하였다. 이 수직 배열층의 바닥면은 벌집통의 바닥처럼 막혀있다. 이런 형태를 '끝이 닫힌 이산화티타늄 나노튜브 수직 배열층'이라고 하고, 이 배열층 바닥면을 이온밀링의 방법으로 깎아내면 위 아래가 완전히 관통된 '끝이 열린 이산화티타늄 나노튜브 수직 배열층'이 만들어진다.

제조된 이산화티타늄 나노튜브 수직 배열층을 염료감응형 태양전지에 도입하여 기능성을 강화하였다. 이어지는 연구는 이 구조에 여러 가지 변인들의 효과를 알아보는 과정이다.

첫 번째 연구는 염료감응형 태양전지에 이산화티타늄 나노튜브 수직 배열층을 도입하는 것이다. 수직으로 배열된 이산화티타늄들에 보다 많은 염료가 부착되고 나노입자일 때보다 grain boundary 손실을 줄이고 전자의 재결합을 줄여서 태양전지의 에너지 전환 효율을 증대시킬 수 있다.

이를 위해 '끝이 닫힌 이산화티타늄 나노튜브 수직 배열층'과 '끝이 열린 이산화티타늄 나노튜브 수직 배열층'을 도입한 결과를 각각 비교하였다.

‘끝이 닫힌 이산화티타늄 나노튜브 수직 배열층’보다 ‘끝이 열린 이산화티타늄 나노튜브 수직 배열층’을 도입할 때 에너지 변환 효율이 5.15% 더 많이 증가되었다(5.92% 대 5.92%). 여기에 비교적 입자의 크기가 큰 이산화티타늄 나노입자로 부가적인 산란층을 더 만들어준 경우 에너지 전환 효율은 10.30%가 더 증가되었다(5.92% 대 6.53%).

추가적으로 ‘끝이 열린 이산화티타늄 나노튜브 수직 배열층’에 사염화티타늄 용액 처리를 해주었더니 에너지 전환 효율이 16.38% 더 증가하였다(5.92%에서 6.89%로). 이것은 염료의 빛 흡수율 증가와 빛 수확 비율이 개선된 결과이다.

두 번째 연구는 ‘끝이 열린 이산화티타늄 나노튜브 수직 배열층’을 산란층으로 염료감응 태양전지에 도입하고 여기에 은 나노입자들을 수직배열층 채널들 사이사이에 생성시키는 것이다. 이 은 나노입자들은 태양전지가 작동할 때 플라즈몬 효과를 나타내게 되어 빛의 흡수율을 높이고, 아울러 추가적으로 도입된 비교적 입자의 크기가 큰 이산화티타늄 나노입자들에 의한 산란효과가 추가되어 결국 전체 에너지 전환 효율이 높아진다.

비교실험으로 먼저 ‘끝이 닫힌 이산화티타늄 나노튜브 수직 배열층’이 도입된 염료감응 태양전지를 만들어 에너지 전환 효율을 측정하였다. 그 후에 비교적 입자의 크기가 큰 이산화티타늄 나노입자를 산란층으로 추가 도입하였더니 6.48%(5.86%에서 6.24%로)의 효율 증가가 나타났다.

한편, 은 나노입자를 추가 도입하였더니 9.21%(5.86%에서 6.40%로)의 효율 증가가 나타나서 이산화티타늄 나노입자에 의한 추가적인 산란층 도입 효과보다는 은 나노입자를 생성시켜서 얻는 플라즈몬 효과가 더 큰 것을 확인하였다.

두 가지 변인 즉, 은 나노입자에 의한 플라즈몬 효과와 이산화티타늄 나노입자에 의한 추가적 산란 효과를 '끝이 닫힌 이산화티타늄 나노튜브 수직배열층'이 도입된 염료감응 태양전지에 함께 적용한 결과 14.50%(5.86%에서 6.71%로)의 에너지 효율증가를 확인하였다.

이번에는 '끝이 열린 이산화티타늄 나노튜브 수직배열층'이 도입된 염료감응 태양전지에 동일한 변인들의 효과를 조사하였다. 그 결과 비교적 큰 이산화티타늄 나노입자층을 산란층으로 추가 도입하여 8.17% (6.12%에서 6.62%로)의 에너지 전환 효율 증가를, 은 나노입자의 도입을 통한 플라즈몬 효과로 9.15%(6.12에서 6.68%로)의 에너지 전환 효율 증가를 확인하였고, 두 변인을 모두 적용하면 15.20% (6.12%에서 7.05%로)의 에너지 전환 효율 증가를 나타내었다.

이산화티타늄 나노튜브 수직 배열층의 바닥이 열려있는지 여부가 에너지 전환 효율과 얼마나 관련이 있는지를 비교하면 끝이 닫힌 수직배열층보다 열린 경우에 더 에너지 전환 효율이 높았다(6.71% 대 7.05%).

결론으로 '끝이 열린 이산화티타늄 나노튜브 수직배열층'을 염료감응형 태양전지에 도입하고, 은 나노입자를 채널 속에 고르게 생성시켰으며, 여기에 더해 비교적 입자의 크기가 큰 이산화티타늄 나노입자를 추가 산란층으로 도입하였을 때, 산란효과와 플라즈몬 효과가

함께 증대되어 에너지 전환 효율이 증가된다.

세 번째 연구는 이산화티타늄 나노튜브 수직 배열층에 은 나노입자와 함께 탄소 물질을 도입하는 것이다. 먼저 선행 연구와 같이 ‘끝이 열린 이산화티타늄 나노튜브 수직 배열층’을 염료감응 태양전지에 도입하고 은 나노입자들을 채널들 사이사이에 생성시키고 에너지 전환 효율을 측정하여 15%(5.32%에서 6.14%로)의 증가를 확인하였다. 이것은 플라즈몬 효과에 기인한다. 이번에는 ‘끝이 열린 이산화티타늄 나노튜브 수직 배열층’이 도입된 염료감응 태양전지에 (고온의 탄화수소를 산화시키는 방법으로) 탄소물질을 생성시켜 만든 태양전지는 에너지 전환 효율이 14%(5.32%에서 6.07%로) 증가하였다. 이것은 파이-파이 공액(공명, 결합)의 결과이다.

‘끝이 열린 이산화티타늄 나노튜브 수직 배열층’이 도입된 염료감응 태양전지에 은 나노입자와 탄소물질이 모두 생성된 경우, 그렇지 않은 경우에 비해 30%(5.32%에서 6.91%로)의 에너지 전환 효율 증가를 나타내었다. 이것은 플라즈몬 효과와 파이-파이 공액(공명, 결합)의 효과가 함께 작용한 결과이다.

Keywords: open-ended freestanding TiO_2 nanotube arrays, dye-sensitized solar cells, plasmonic, scattering, anodization